

UNIVERSITY OF SOUTHAMPTON

**Multi-scale Friction Modelling of Lubricant-Surface  
Interaction in Tribological Contacts**

by

Siti Hartini binti Hamdan

A thesis submitted in fulfillment of the requirements  
for the degree of Doctor of Philosophy

in the

national Centre of Advance Tribology (nCATS)  
Faculty of Engineering and the Environment  
Mechanical Engineering Department

May 4, 2018

UNIVERSITY OF SOUTHAMPTON

**ABSTRACT**

FACULTY OF ENGINEERING AND ENVIRONMENT  
MECHANICAL ENGINEERING DEPARTMENT  
national Centre of Advance Tribology (nCATS)

Doctor of Philosophy

**MULTI-SCALE FRICTION MODELLING OF LUBRICANT-SURFACE  
INTERACTION IN TRIBOLOGICAL CONTACTS**

by Siti Hartini binti Hamdan

The study emphasises on the fundamental understanding of the tribological behaviour for a lubrication system. In a dynamic system (e.g. piston ring/liner contact), the opposing sliding surfaces are separated by a layer of lubrication film, preventing direct metal-to-metal contact. Under critical operating conditions (e.g. high applied load), the film thickness might reduce to similar order of magnitude of the surface roughness, leading to boundary friction. A multi-scale approach is required to better predict the lubrication performance in a dynamic system. The first part of this study focuses on the development of a numerical algorithm using Reynolds equation to predict fluid film formation in a lubrication system. A rough surface contact model using the Greenwood and Tripp assumption is applied to predict the frictional properties along a lubricated conjunction using a three types of commercially available SAE grade lubricant namely, SAE5W40, SAE10W40 and SAE15W40. The simulated friction force is compared to the values measured using a pin-on-disc tribometer, showing good correlation between both data sets. With acceptable level of confidence on the mathematical model, the second part of the study attempts to simulate a tribological properties of lubrication system considering biodiesel as the lubricant in the engine lubrication system. As the rough surface contact parameters are considered to be consistent in both case study, Reynolds solution is modified in order to considers the fluid film formation of biodiesel with relation to their Fatty Acid Methyl Ester (FAME) compositions. Two parameters, namely 1) average number of carbon atom ( $z_{ave}$ ) and 2) average number of double bonds ( $nd_{ave}$ ) for biodiesels are included when introducing the effect of FAME compositions to the classical Reynolds equation. The term  $\chi$  has been introduced to the modified Reynolds equation to correlate these two parameters. The value for the term  $\chi$  is determined by fitting the simulated lubrication Stribeck curve to the measured data for each of the selected biodiesels. Through this, a polynomial correlation is then obtained for the term  $\chi$  as a function of the product of average number of carbon atoms and average number of double bonds for the biodiesels. The coupling of Reynolds solution and rough surface contact model give a good correlation between measured data and predicted value in determining lubrication Stribeck curve regime for typical lubricants and biodiesel.

# Contents

<b>Nomenclature</b>	<b>xiv</b>
<b>Acknowledgements</b>	<b>xvi</b>
<b>1 Introduction</b>	<b>1</b>
1.1 Aim . . . . .	3
1.2 Research aim and objectives . . . . .	3
1.3 Research outline . . . . .	4
1.4 Expected research deliverable . . . . .	5
1.5 Summary . . . . .	6
<b>2 Literature Review</b>	<b>7</b>
2.1 Introduction . . . . .	7
2.2 Fundamentals of Tribology . . . . .	7
2.3 Lubrication Stribeck curve . . . . .	13
2.4 Rough surface contact along mixed and boundary lubrication regimes .	16
2.5 Alternative lubricants - biolubricants . . . . .	19
2.6 Application specific-modifications to Reynolds equation . . . . .	21
2.7 Measurements of tribological properties . . . . .	25
2.8 Summary . . . . .	27
<b>3 Numerical Approach for Friction Prediction</b>	<b>28</b>
3.1 Fluid film formation prediction based on Reynolds Solution . . . . .	28
3.2 Discretisation of Reynolds equation . . . . .	30
3.3 Numerical scheme . . . . .	32



3.4	Rough surface contact model . . . . .	34
3.5	TaiCaan Laser Profilometer . . . . .	39
3.6	Rheological properties for SAE grade lubricants . . . . .	41
3.7	Results and discussion . . . . .	42
3.8	Summary . . . . .	54
<b>4</b>	<b>Friction Measurements</b>	<b>56</b>
4.1	Introduction . . . . .	56
4.2	Friction testing using pin-on-disc tribometer . . . . .	56
4.3	Friction measurements for SAE grade lubricants . . . . .	60
4.3.1	Correlating friction measurements <i>for SAE grade lubricants</i> with simulation . . . . .	61
4.4	Biodiesel production using transesterification process . . . . .	70
4.5	Friction measurements <i>for biodiesel</i> . . . . .	74
4.5.1	Ternary plot mapping of biodiesel frictional properties . . . . .	81
4.6	Summary . . . . .	84
<b>5</b>	<b>Simulation of biodiesel tribological properties</b>	<b>86</b>
5.1	Preliminary simulation findings . . . . .	86
5.2	Modified mathematical approach for biodiesel . . . . .	90
5.3	Relationship between FAME compositions and Reynolds equation . . . . .	101
5.4	Verification and validation of modified Reynolds equation . . . . .	107
5.5	Summary . . . . .	112
<b>6</b>	<b>Conclusion and Future work</b>	<b>113</b>
6.1	Conclusion . . . . .	113
6.1.1	Phase 1 . . . . .	113
6.1.2	Phase 2 . . . . .	114
6.1.3	Phase 3 . . . . .	115
6.2	Main contribution to knowledge . . . . .	117
6.3	Future work . . . . .	117
	<b>References</b>	<b>119</b>

<b>Appendix A Derivation of two-dimensional Reynolds solution; point contact problem</b>	<b>132</b>
A.1 Dimensionless parameter for 2D point contact: . . . . .	133
A.2 Jacobian matrix . . . . .	137
A.3 Mathematical derivation for surface deflection . . . . .	146
<b>Appendix B SAE grade lubricant</b>	<b>148</b>
<b>Appendix C List of Publications</b>	<b>151</b>

# List of Figures

1.1	Gasoline fuel energy distribution for a unit average passenger car[4]	2
2.1	Various types of contact between surfaces	8
2.2	Elastic line contact and point contact between surfaces	9
2.3	Contact pressure distribution in EHL solutions by Petrusevich [23]	12
2.4	Lubrication Stribeck curve	14
2.5	Nature of surfaces	17
2.6	Configuration of tribometer pin-on-disc and pin-on-plate	25
2.7	Schematic outline of Plint TE 77 reciprocating pin-on-plate tribometer [85]	26
2.8	Schematic diagram of the four-ball wear machine.[87]	26
2.9	Photograph and diagram of the test zone in the MTM.[88]	27
3.1	Point contact conjunction.	29
3.2	Flow chart of Reynolds equation iterative solution	34
3.3	Contact of rough surfaces.	36
3.4	A non-Newtonian Shear-strain curve	38
3.5	Laser Profiler using TaiCaan <sup>TM</sup> machine	39
3.6	XYRIS 8600 CL	40
3.7	Schematic diagram for rheometer measurements	42
3.8	Experimentally measured on rheological properties at different temperatures for commercially available engine lubricants	43
3.9	Lubrication regime mapping for simulated SAE grade lubricants based on simulated conditions	45

3.10	Contact pressure distribution and lubricant film profile for simulated point contact lubricated with selected SAE grade lubricants at sliding velocity of 4 m/s . . . . .	46
3.11	Contact pressure distribution and lubricant film profile for point contact lubricated with SAE5W40 grade engine lubricant . . . . .	48
3.12	Contact pressure distribution and lubricant film profile for point contact lubricated with SAE10W40 grade engine lubricant . . . . .	49
3.13	Contact pressure distribution and lubricant film profile for point contact lubricated with SAE15W40 grade engine lubricant . . . . .	50
3.14	Viscous shear calculated using various formulation . . . . .	52
3.15	Viscous shear with $\gamma = 0.08$ MPa . . . . .	53
3.16	Viscous shear with $\tau_0 = 2$ MPa . . . . .	54
4.1	Pin (cast iron) and wear disc . . . . .	57
4.2	Ultrasonic bath -SONICA . . . . .	58
4.3	Experimental setup on pin-on-disc tribometer machine . . . . .	58
4.4	Schematic views of pin-on-disc tribometer . . . . .	59
4.5	Stribeck curve of selected engine lubricant on pin-on-disc tribometer machine . . . . .	61
4.6	Lateral Force Microscopy (LFM) setup . . . . .	62
4.7	Measured friction force for wear disc surface lubricated with ZDDP using Lateral Force Microscopy . . . . .	63
4.8	Simulated lubricant Stribeck curve for selected commercially available engine lubricant . . . . .	65
4.9	Viscous and boundary shear properties for point contact lubricated with SAE5W40 grade engine lubricant. . . . .	67
4.10	Viscous and boundary shear properties for point contact lubricated with SAE10W40 grade engine lubricant. . . . .	68
4.11	Viscous and boundary shear properties for point contact lubricated with SAE15W40 grade engine lubricant . . . . .	69
4.12	Ternary plot describing the fatty acid methyl ester composition for the tested biodiesels . . . . .	71
4.13	Flow chart of a biodiesel process . . . . .	72

4.14	Transesterification reaction derived from vegetable oil . . . . .	72
4.15	Coefficient of friction (CoF) measured at varying sliding velocity at 20N load for tested biodiesels compared with SAE5W40 standard lubricant . . . . .	75
4.16	Average friction force variation with critical velocity values at (a) EHL (b) and BL regimes for tested biodiesels . . . . .	76
4.17	Average friction force along (a) EHL and (b) BL regimes with the amount of saturated fatty acid composition . . . . .	78
4.18	Friction modifier properties: (a) Critical velocity and (b) Mixed lubrication velocity span of the biodiesels . . . . .	80
4.19	Ternary plot describing the change in critical velocity with the fatty acid composition for the tested biodiesels . . . . .	83
5.1	Contact pressure distribution and lubricant film profile for simulated point contact lubricated with palm and soybean biodiesel at sliding velocity of 4 m/s . . . . .	89
5.2	Lubrication Stribeck curve validation . . . . .	91
5.3	Contact pressure distribution and lubricant film profile for simulated point contact lubricated using biodiesels at sliding velocity of 4 m/s . . . . .	93
5.4	Contact pressure distribution and lubricant film profile at point contact lubricated for Coconut biodiesel . . . . .	94
5.5	Contact pressure distribution and lubricant film profile at point contact lubricated for Palm biodiesel . . . . .	95
5.6	Contact pressure distribution and lubricant film profile at point contact lubricated for soybean biodiesel . . . . .	96
5.7	Viscous and boundary shear properties for point contact lubricated with Coconut biodiesel . . . . .	98
5.8	Viscous and boundary shear properties for point contact lubricated with Palm biodiesel . . . . .	99
5.9	Viscous and boundary shear properties for point contact lubricated with soybean biodiesel . . . . .	100
5.10	Stribeck curve validation . . . . .	102
5.11	Contact pressure distribution and lubricant film profile for point contact lubricated with canola biodiesel . . . . .	103

5.12	Viscous and Boundary shear properties for point contact lubricated with canola biodiesel . . . . .	104
5.13	Contact pressure distribution and lubricant film profile for point contact lubricated with olive biodiesel . . . . .	105
5.14	Viscous and Boundary shear properties for point contact lubricated with olive biodiesel . . . . .	106
5.15	Coefficient of $\chi$ . . . . .	107
5.16	Stribeck curve validation . . . . .	108
5.17	Contact pressure distribution and lubricant film profile for point contact lubricated with shortening biodiesel . . . . .	110
5.18	Viscous and Boundary shear properties for point contact lubricated with shortening biodiesel . . . . .	111

# List of Tables

3.1	Simulated tribological conjunction for point contact . . . . .	35
3.2	Motion system specification . . . . .	40
3.3	Motion stage range . . . . .	40
3.4	Simulated Rheological properties for commercially available SAE grade lubricants . . . . .	43
3.5	Measured value of a rough surface contact parameters using Taicaan laser profilometer . . . . .	51
3.6	Friction value with constant $\gamma = 0.08$ . . . . .	53
3.7	Friction value with constant $\tau_0 = 2\text{MPa}$ . . . . .	53
4.1	Technical specification of a typical Pin-on-disc tribometer machine . . .	57
4.2	Parametric values of simulated lubricant study for SAE grade lubricant	64
4.3	Fatty acid methyl ester compositions for tested biodiesels [108][109] . .	73
4.4	Bulk density for selected biodiesels . . . . .	74
4.5	Melting temperature for feedstocks used to derive the tested biodiesels	79
5.1	Experimentally measured rheological properties of selected biodiesels .	86
5.2	Average carbon number and average number of double bond for vegetable oil derived biodiesel [111] . . . . .	88
5.3	Predicted values for friction estimation . . . . .	91
5.4	Average carbon number and average number of double bond for vegetable oil derived biodiesel [111] . . . . .	101
5.5	Biodiesel rheological parameters . . . . .	101
5.6	Predicted values for friction estimation . . . . .	102
5.7	Average carbon number and average number of double bond for vegetable oil derived biodiesel [111] . . . . .	107

5.8 Biodiesel rheological properties . . . . .	108
5.9 Predicted values for friction estimation . . . . .	109
A.1 Non-dimensional parameters . . . . .	133



## Academic Thesis: Declaration Of Authorship

I, Siti Hartini Binti Hamdan .....

declare that this thesis and the work presented in it are my own and has been generated by me as the result of my own original research.

Multi-scale Friction Modelling of Lubricant-Surface Interaction in Tribological Contacts

.....

I confirm that:

1. This work was done wholly or mainly while in candidature for a research degree at this University;
2. Where any part of this thesis has previously been submitted for a degree or any other qualification at this University or any other institution, this has been clearly stated;
3. Where I have consulted the published work of others, this is always clearly attributed;
4. Where I have quoted from the work of others, the source is always given. With the exception of such quotations, this thesis is entirely my own work;
5. I have acknowledged all main sources of help;
6. Where the thesis is based on work done by myself jointly with others, I have made clear exactly what was done by others and what I have contributed myself;
7. ~~Either none of this work has been published before submission, or~~ parts of this work have been published as:
  - I. M.H. Din, S.H. Hamdan. W.W.F. Chong. Frictional Analysis on Engine Lubricant Dilution by Coconut oil and Soybean oil Derived Biodiesel. *Jurnal Tribologi*. Accepted.
  - II. Y.C. Ng, S.H. Hamdan. W.W.F. Chong. Development Of A Mathematical Tool To Predict Engine In-Cylinder Friction. *Jurnal Tribologi*. Accepted.
  - III. S.H. Hamdan, W.W.F. Chong, J.-H. Ng , C.T. Chong and S. Rajoo. A study of the tribological impact of biodiesel dilution on engine lubricant properties. *Process Safety and Environmental Protection*. doi.org/10.1016/j.psep.2017.05.007, 2017 .
  - IV. S.H. Hamdan, W.W.F. Chong, J.-H. Ng, M.J. Ghazali, and R.J.K. Wood. Influence of Fatty Acid Methyl Ester Composition on Tribological Properties of Vegetable Oils and Duck Fat Derived Biodiesel. *Tribology International*. dx.doi.org/10.1016/j.triboint.2016.12.008, 2016.

Signed:

Date: ..... 4th MAY 2018

# Nomenclature

<i>BTU</i>	British thermal unit
<i>ZDDP</i>	Zinc dialkyldithiophosphate
<i>EJ</i>	Exajoule
<i>H</i>	Oil film thickness.
<i>HL</i>	Hydrodynamic lubricant.
<i>EHL</i>	Elastohydrodynamic lubricant
<i>ML</i>	Mixed lubricant.
<i>BL</i>	Boundary lubricant
$\eta_0$	Lubricant Viscosity (m.Pa.s)
$\alpha_0$	Viscosity coefficient at $p = 0$
<i>u</i>	Lubricant entraining velocity (m/s).
$dA_a$	Single asperity contact area ( $m^2$ )
$dA_{aa}$	Total asperity/actual contact area ( $m^2$ ).
$df_v$	Viscous friction for an element of apparent contact area ( $N/m^2$ )
$df_b$	Boundary friction for an element of apparent contact area ( $N/m^2$ )
$df_{tot}$	Total friction for an element of apparent contact area ( $N/m^2$ )

$i, j$	Points along contact domain
$P$	Contact pressure
$u_{av}$	Lubricant entraining speed (m/s)
$\alpha$	Non- dimensional term (chapter 2)
$\alpha$	Pressure-viscosity coefficient (chapter 3)
$\alpha$	Corresponding to the applied normal loads (chapter 4 )
$\beta$	Lubricant bulk modulus (Pa.s)
$\rho$	Lubricant density (kg/m <sup>3</sup> )
$\sigma$	RMS surface height(m)
$\tau$	Lubricant shear stress (Pa)
$\kappa$	Pressure coefficient of the boundary shear strength
$\gamma$	Slope of the limiting shear stress-pressure relation
$\sigma$	RMS surface roughness
$\gamma$	Lubricant limiting shear stress pressure relation
$\zeta$	Equivalent to the slope of the measured friction values
$\kappa$	Pressure coefficient
$\bar{\rho}$	Non dimensional lubricant density
$\bar{\eta}$	Non dimensional lubricant viscosity
$a, b$	Width of the contact area (a=b)
$g$	Switch function
$\beta$	Lubricant bulk modulus (Pa.s)

$\theta$	Frictional film content cavitation
$\Phi$	Pressure flow factor
$h_t$	Average gap
$\mathbf{u}$	Surface velocity
$\theta$	Exponential expression
$\alpha$	Piezoviscous coefficient
$\theta$	Flow rate
$\alpha$	Rarefaction correction parameter
$K_n$	Knudsen number
$\Gamma(x, z)$	Function of circumferential coordinate ( $x$ ), and axial coordinate ( $z$ ).

# Acknowledgements

First and foremost, I would like to wish personally a million thanks to my principal supervisor, Dr William W.F. Chong, who have been there with me for the past three year and become a tremendous mentor to me. His endless effort, his guidance, his sharing and his willingness to guide me along the way are highly appreciated. I also would like to express my highest gratitude to my coordinating supervisor Dr Jo-han Ng for his help particularly for his guidance whenever I used his lab, and also to Prof. Dr John McBride and Prof Dr Robert Wood for their support towards the successful completion of this thesis.

A special thanks to my sponsors, MARA and UNIKL, without their financial support, this work might not become reality. Special thanks to Associate Professor Dr Mariyam Jameelah Ghazali from UKM and Associate Professor Dr Suzana Yusup from UTP for their assistance during my presence at their respective labs.

A million thanks also to my dearest parent, Mr Hamdan Mohamad and Mrs Siti Safiah Ibrahim, who are always there for me, giving the much needed moral support in my life. I am also very thankful to all my family members with their indirect support along the way.

A special gratitude to my life-partner, Mr Maswari Sulaiman for his motivation and encouragement through out this journey and for my children, Fatin and Adam, this is for both of you to repeat.

I would also like to share my gratitude to all my friends and colleagues at University of Southampton (UK and Malaysia campus) for their moral support and encouragement during my this journey.



# Chapter 1

## Introduction

Within the next 25 years, it is expected that the global energy demand will increase from 557 quadrillion BTU (588 EJ) in the year 2014 to 703 quadrillion BTU (742 EJ) in the year 2040 [1]. This will give a serious impact on greenhouse gas emissions. In view of this, the International Energy Agency (IEA) has started the 'decarbonisation' effort to encounter the climate changes caused by the possible increase in greenhouse gas emission [2]. Specifically, for transportation sector, decarbonisation could be achieved by having an improved fuel economy through decreasing frictional forces. Figure 1.1 shows that for a passenger car, one third of the fuel energy is used to overcome friction. Figure 1.1 illustrates the gasoline fuel energy distribution for an average passenger car, showing that only 17.5% of available fuel energy is used to move the vehicle. It is highlighted that the energy lost arising from engine and transmission frictional losses adds up to as much as 22.3% of the total available fuel energy of a typical passenger car. In view of this, Holmberg *et al.* stressed that friction reduction in passenger cars could be achieved through tribological improvements in the engine, tires, transmission and brakes systems [3]. Using effective methods in reducing friction, they predicted that the drop of CO<sub>2</sub> emission might sum up to 290 million tons in the short term (5-10 years) and 960 million tons in the long term (15-25 years).

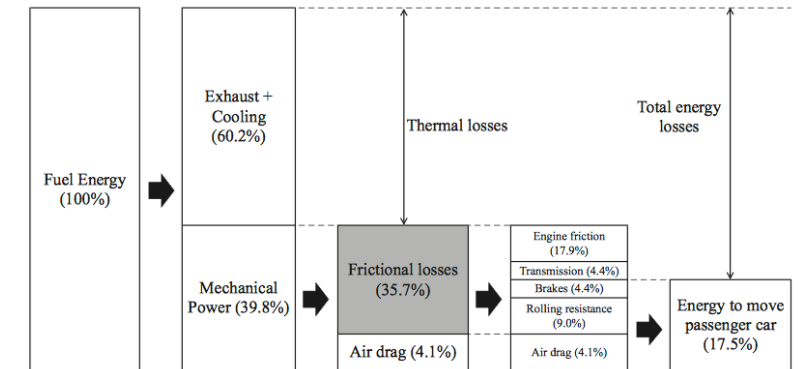


Figure 1.1: Gasoline fuel energy distribution for a unit average passenger car[4]

Obviously, these methods still involve the usage of lubricant. It is predicted that the global lubricant consumption in the automotive sector is around 22 million tonnes in 2015 [5] and most of these lubricants are still mineral oil based. Another concern of using the current crop of lubricants is also raised by Wong and Tung [6], where lubricant-derived emissions, from synthetic additives such as Zinc dialkyldithiophosphate (ZDDP), could have serious impact on the exhaust-after treatment system, which might eventually lead to emissions of toxic pollutants.

Decarbonisation in the transportation sector could also be achieved by using alternative fuels/lubricants to replace fossil-fuel. With respect to the impact of tribology towards the environment, the concept of Green tribology has been introduced. Green Tribology refers to the science and technology of the tribological aspects of ecological balance and of environmental and biological impacts [7]. Twelve principles have been formulated for this concept, with one of them focusing on the use of biodegradable lubrication [8].

One type of biodegradable lubricant that could be considered is biodiesel. A biodiesel is considered to be biodegradable [9, 10] if a minimum of 90% from its composition degraded within 3 weeks [11]. Having a mixture of biodiesel at 20% and 80% diesel fuel, this blend will be degraded twice faster compared to diesel itself [12]. Therefore, with the ability to be decomposed within a short period, a standard biodiesel is one of the better alternative fuels or lubricants applied in environmentally sensitive areas.

Biodiesel refers to fatty acid methyl or ethyl esters made from vegetable oils or animal fats and has good lubrication properties. It has also been proven to be capable



of enhancing the lubrication properties of petrol-diesel fuels [13]. It is widely accepted as a replacement for petro-diesel fuel to be used in diesel engine. Biodiesel feedstocks are selected base on their availabilities to be used in a diesel engine without requirement of modification of the engine. However, tribological characterisation studies typically focus on the use of biodiesel in the presence of ultra-low sulphur petro-diesel fuel, with little to none emphasis on the possible application of the biodiesel as lubricant and/or lubricant additives. Therefore, the current study intends to investigate the frictional properties of biodiesel, derived from different feedstocks, for the whole range of lubrication regimes. The study is hoped to be able to explore the capacity of biodiesel as possible biodegradable alternative [14] to existing lubricants and lubricant additives.

## **1.1 Aim**

The aim for this research is to study the lubrication properties of alternative biodegradable lubricant, such as biodiesel. It is essential to understand the fundamental tribological characteristics of such alternative biodegradable in order to determine its potential as an effective lubricant or lubricant additive. The focus of the study will be on investigating the interfacial phenomena governing fluid film formation and determining the underlying friction mechanisms of contacts lubricated with biodiesel.

## **1.2 Research aim and objectives**

To achieve the aim, the study emphasises on the fundamental understanding of tribological phenomena governing fluid film lubrication along opposing sliding surfaces across the whole range of lubrication regimes, namely hydrodynamic lubrication (HL), elastohydrodynamic lubrication (EHL), mixed lubrication (ML) and boundary lubrication (BL) regimes. The study adopts an empirical approach in determining the frictional characteristics of a lubrication system in the presence of biodiesel. The study is divided into three phases, where the first two phases focus on the development and the validation of mathematical tools required to fundamentally investigate frictional properties of a typical lubrication system, while the final phase looks into the application of the developed predictive tools to understand the tribological properties of a

biodiesel lubricated contact conjunction. Hence, the research objectives for the first phase are:

- To develop a numerical model for Reynolds solution to predict fluid film formation along a lubricated contact.
- To formulate a rough surface contact friction model to predict friction for a lubricated contact along the whole range of lubrication regimes.

For the second phase, the research objectives are:

- To measure frictional properties of lubricated contact of selected SAE grade engine lubricants for the whole range of lubrication regimes using a tribometer.
- To compare friction for a lubricated contact measured using a tribometer with predicted values using the developed mathematical tools.

Finally, for the third phase, the research objectives are:

- To derive laboratory grade biodiesel from various types of vegetable oil using transesterification process.
- To characterise frictional properties of various types of vegetable oil derived biodiesel using a tribometer.
- To simulate and validate shear properties of biodiesel lubricated contact using the developed mathematical tools.

## 1.3 Research outline

The current study is conducted based on the following outline:

- *Chapter 2* reviews on the fundamentals of tribology, covering aspects lubrication regimes and lubricant fluid film formation prediction approaches, inclusive of Reynolds equation. The different modifications of Reynolds equation for various tribological applications are discussed. The various lubrication regimes, namely hydrodynamic, elastohydrodynamic, mixed and boundary lubrication regimes,

are discussed based on the Stribeck curve. Rough surface contact characteristics, which influences the properties of mixed and boundary lubrication regimes are also reviewed. In this chapter, a review is also included on alternative lubricants and experimental approaches in characterising lubricants.

- Chapter 3 emphasises on the development of a numerical algorithm, solving for Reynolds equation. The developed numerical method for Reynolds equation are used to simulate for commercially available SAE grade engine lubricant. The analysis conducted in this chapter focuses on the fluid film formation properties of selected SAE grade engine lubricants. The chapter also discusses on the integration of the Reynolds solution with a Greenwood and Tripp rough surface contact friction model in determining the shear properties of selected SAE grade engine lubricants.
- Chapter 4 carries out friction testing for the selected SAE grade engine lubricants using a tribometer. A validation is conducted for the developed mathematical model for the selected SAE grade engine lubricants. The chapter also discusses on the method to synthesize biodiesel from various types of vegetable oils. From the derived laboratory grade biodiesel, the frictional characteristics are measured using a tribometer.
- Chapter 5 applies the developed mathematical model for biodiesel lubricated contact in order to determine the fluid film formation properties of such conjunction. The Reynolds equation is modified to consider the fatty acid methyl ester composition of biodiesels.
- *Chapter 6* concludes the findings for the study and proposes future work to extend the current study.

## 1.4 Expected research deliverable

By the end of the study, it is expected that the study produces a validated mathematical predictive tool, which is capable of predicting fluid film formation (based on Reynolds solution) and frictional properties across the whole range of lubrication

regimes (based on rough surface contact model) for contacts lubricated by typical lubricants and biodiesel. The model will serve as a fundamental platform in order to better understand the frictional implications when biodiesel is mixed with typical lubricants.

## **1.5 Summary**

The chapter lays out the problem for utilising biodiesel fuel in compression ignition engines, which affects the lubrication system in the engines. In order to understand the underlying mechanisms affecting the lubrication system in the engines running on petro-diesel blended with biodiesel, the chapter summarises the aim, objectives and expected outcome from the study. The next chapter will discuss on the fluid film formation properties of typical lubrication systems based on Reynolds equation, which will form the basis of the development of the proposed mathematical tools for the current study.

# Chapter 2

## Literature Review

### 2.1 Introduction

### 2.2 Fundamentals of Tribology

Since the last few decades, lubrication of non-conformal contacts have been one of the significant topic of research in the field of tribology. This relates to the application of a heavily loaded contacts in roller bearings, ball bearings, gears, and traction drives. To understand the mechanism underlying the lubrication system, it is important to begin with the basic contact mechanics knowledge. Contact mechanics explains the change in shape when two solids touch each other. The contact of two elastic bodies under non-lubricated condition can typically be described initially as a point contact or a line contact as shown in Figure 2.1. Even with minimum load, the two surfaces will create a finite contact area.

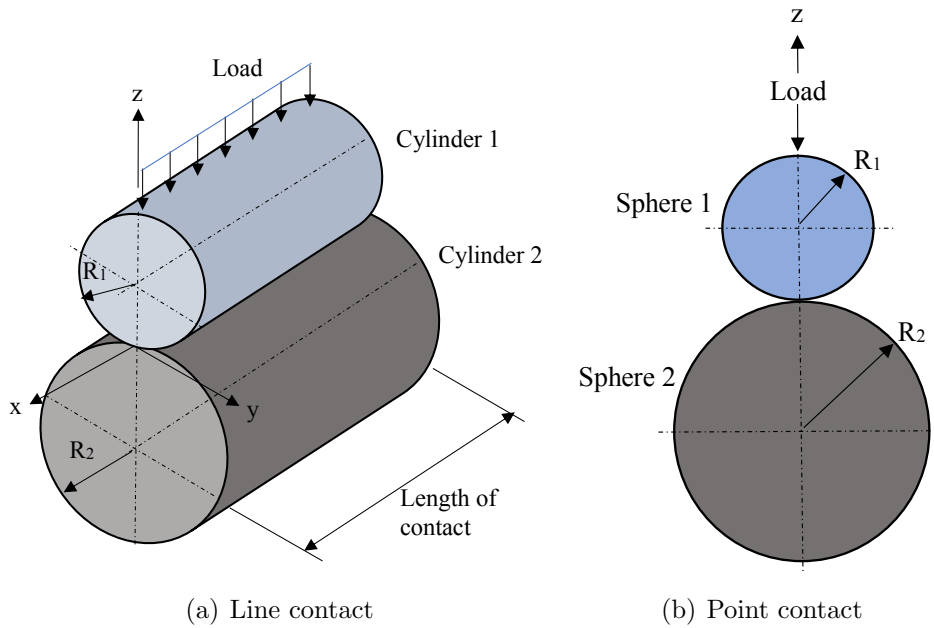


Figure 2.1: Various types of contact between surfaces

The method for determining the contact pressure was first described by Hertz. The Hertzian contact theory as shown in Table 2.2 for a line and a point contact assumes that:

- The size of the contact area is small compared with the size of the curved bodies.
- Both contacting surfaces are smooth and frictionless.
- The deformation is elastic and can be calculated by treating each body as an elastic half space or known as flat surface on an infinite elastic solid.
- The gap,  $h$  between the undeformed surfaces may be approximated by an expression of the form  $h = Ax^2 + By^2$  (e.g. the contact between spheres, cylinders, and ellipsoids).

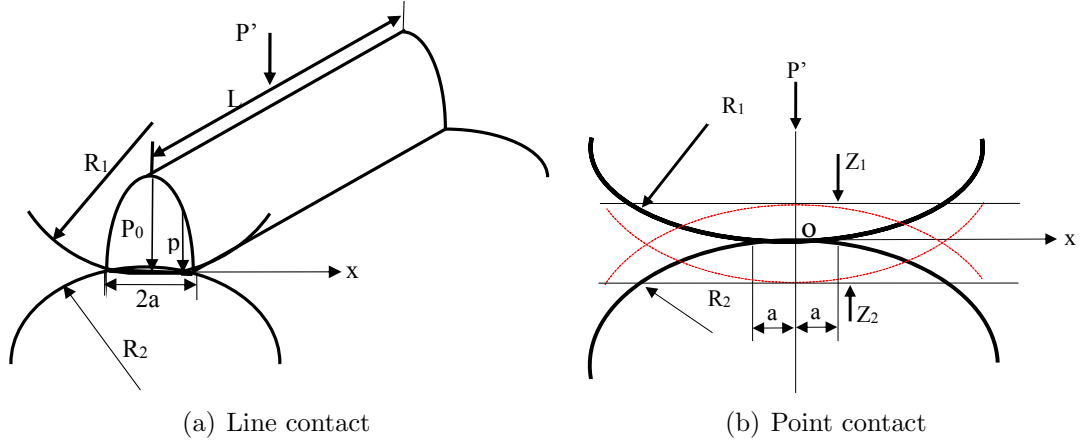


Figure 2.2: Elastic line contact and point contact between surfaces

It is to note that for a line contact problem, a cylindrical shape can be defined as  $x^2 = (2R - z)z$ , where  $z$  is taken to be the distance above the  $xy$  plane, while  $E^*$  is the composite or reduced Young's Modulus of contacting planes.

Table 2.1 Relationships between variables in elastic contact [15]

Variable	Line contact	Point contact
Contact Pressure distribution	$p = p_0(1 - x^2/a^2)^{1/2}$	$p = p_0(1 - r^2/a^2)^{1/2}$
Contact half width or radius	$a = (4P'R/\pi E^*)^{1/2}$	$a = (3WR/4E^*)^{1/3}$
Max and mean contact pressure	$p_0 = 4/\pi p_m = (P'E^*/\pi R)^{1/2}$	$p_0 = 3/2 p_m = (6WE^2/\pi^3 R^2)^{1/3}$
Load or load/unit length	$P' = 2ap_m$	$W = \pi a^2 p_m$
Maximum shear stress	$0.3p_0, 0.78a$ *	$0.31p_0, 0.48a$ *

(\*below surface on contact centre line)

However, Hertzian theory covers only dry contacts. For lubricated contact, one of the commonly used theory to predict the tribological behaviour of sliding contact is derived by Reynolds [16]. This has become the foundation of hydrodynamic lubrication theory ever since. Reynolds equation relates contact geometry, relative sliding velocity of opposing surfaces, lubricant properties (viscosity and density) and applied normal load with lubricant fluid film formation properties, such as contact pressure distribution and lubricant film thickness. The contact pressure generated within the lubricant film, which tends to push the opposing surfaces apart, balances the normal load applied on the opposing surfaces in relative motion [15].

Reynolds equation is divided into two main components: 1) *Poiseuille* flow and 2) *Couette* flow. *Couette* flow occurs because of the relative motion between opposing

surfaces, while *Poiseulle* flow comes from the variation along the contact pressure distribution within the contact. The equation is written as follow, with the terms on the left hand side being the *Poiseulle* flow and the term on the right hand side being the *Couette* flow:

$$\frac{\partial}{\partial x} \left[ \frac{\rho h^3}{12\eta} \frac{\partial p}{\partial x} \right] + \frac{\partial}{\partial y} \left[ \frac{\rho h^3}{12\eta} \frac{\partial p}{\partial y} \right] = 12 \left\{ \frac{\partial}{\partial x} [\rho h u_{av}] + \frac{\partial}{\partial y} [\rho h v_{av}] + \frac{\partial \rho h}{\partial t} \right\} \quad (2.1)$$

where  $u_{av}$  is the average sliding velocity in  $x$ -direction,  $v_{av}$  is the average sliding velocity in  $y$ -direction,  $\eta$  being the lubricant viscosity,  $\rho$  being the lubricant density,  $h$  being the lubricant fluid film thickness. The  $x$  and  $y$  direction in the equation refer to the lubricant flow direction. *Couette* flow is shown to consist of a combination of wedge (velocity dependent terms) and *squeeze film*. Reynolds equation assumes that:

- Lubricant film has negligible mass.
- Contact pressure is assumed to be constant across the lubricant film thickness because the film is thin.
- No slip occurs at the boundaries.
- Lubricant flow is laminar (Low Reynolds numbers).
- Inertia and surface tension forces are negligible as compared to viscous forces.
- Shear stress and velocity gradient are only significant across the lubricant film thickness.
- The lubricant is Newtonian (high shear rate are not present).
- Lubricant viscosity is constant across the lubricant film thickness.
- Boundary surfaces follow the designated geometry but are always at low angles to each other.



Reynolds stated that negative pressure along the outlet of the contact is not included in the formulation [16]. As a simplification, it is commonly assumed that the outlet pressure is equivalent to the atmospheric pressure. Even though this is a simplistic way of approaching the problem, the mass conservation along the cavitation region is still not yet satisfied. An answer to this problem is provided by Jakobsson and Floberg [17] together with Olsson [18], known as the JFO theory. They suggested a new set of boundary conditions for the Reynolds equation. There are two separate regions being introduced: (i) full film and (ii) cavitation. Reynolds equation can then be described using the full film region. However, in the cavitation region, the film breaks down and lubricant behaviour is predicted using the continuity of flow [19].

Ever since the introduction of Reynolds equation, there are another two related areas of lubricant analysis that have been widely discussed on. These involve the effect of localised elastic deformation of the two surfaces and the increase in lubricant viscosity caused by a high contact pressure [20], which eventually led to the introduction of elastohydrodynamic lubrication (EHL). Grubin investigated the fluid film formation mechanism of EHL [21] and his theory was inspired by Ertel's preliminary results obtained as early as 1939 [22].

The Grubin assumptions discussed on both elastic deformation and the increase in lubricant viscosity simultaneously. These assumptions can be concluded as [21]: (1) the shape of the elastically deformed cylindrical bodies in a heavily loaded lubricated contact is the same as that in the corresponding dry contact and (2) the hydrodynamic pressure approaches infinity at the inlet border of the Hertzian contact zone. After this historical finding by Grubin [21], one-dimensional EHL problems were given much attention in the 1950s and 1960s [20].

In 1951, Petrusevich [23], presented a tribological contact pressure distribution plot as shown in Figure 2.3. The results demonstrated typical EHL characteristics for the first time. This includes a nearly constant central film thickness and EHL pressure distribution that is close to a Hertzian contact. A film constriction downstream near the outlet and a high-pressure spike at the outlet side right before the film constriction were also observed. This secondary pressure spike was later named as the 'Petrusevich Spike' [23].

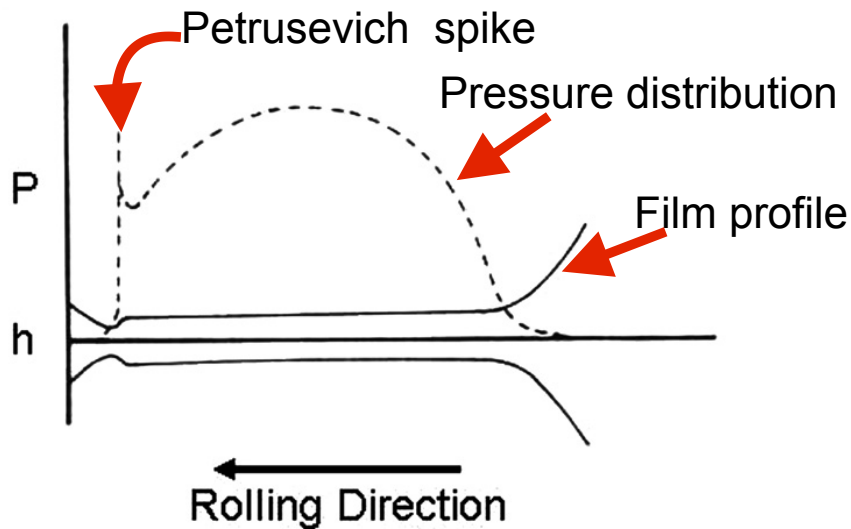


Figure 2.3: Contact pressure distribution in EHL solutions by Petrusevich [23]

In order to distinguish EHL from hydrodynamic lubrication (HL), the terms isoviscous-elastic and piezoviscous elastic lubrication regimes are used to highlight the EHL phenomena. Hamrock [24] and Esfahanian and Hamrock [25] explained that isoviscous-rigid regime is a condition where the magnitude of the elastic deformation of the surfaces is insignificant towards the fluid film separating them with the maximum pressure in the contact being too low to increase fluid viscosity significantly. In isoviscous-elastic or also known as soft EHL, elastic deformation of the solid has a significant effects on the thickness of the lubricant film. However, the contact pressure for such EHL type is still quite low and insufficient to cause any substantial increment in the lubricant viscosity.

For a piezoviscous-rigid regime, the contact pressure within the contact is usually high enough to increase the lubricant viscosity within the conjunction significantly. This may then be necessary to consider the pressure-viscosity characteristics of the lubricant while assuming that the solids remain rigid. For this particular regime to prevail, the deformation of the surfaces must remain insignificant towards the lubricant film thickness. In a fully developed EHL, piezoviscous-elastic lubrication regime or also known as hard EHL, appears where the elastic deformation of the solids play a significant part in affecting the lubricant film thickness that separates them. The contact pressure within the contact for this EHL type is typically high enough to cause

a significant increase in lubricant viscosity by few orders of magnitude.

In order to determine the lubricant film thickness under EHL, Dowson and Higginson [26] developed a solution, called the inverse solution, to overcome difficulties associated with slow numerical convergence observed in the early straightforward iterative processes for EHL problems. The inverse solution procedure appeared to be capable of handling heavily loaded cases and getting a converged solution within a small number of iterations [20]. A curve-fitting formula for predicting one-dimensional line contact EHL minimum film thickness was presented by Dowson [27] as follow:

$$H_m = h_m/R_x = 1.6G^{*0.6}U^{*.7}W^{-0.13} \quad (2.2)$$

where the dimensionless parameters used in these formulas for a line contact are; speed parameter =  $U^*$ , load parameter =  $W^*$ , materials parameter =  $G^*$ , and film thickness parameter =  $H$ . This classical film thickness formulation by Dowson and Higginson [28] for line contact are essential in better understanding the characteristics of EHL contacts. Recently, solving Reynolds equation, Kushwaha and Rahnejat [29] and Teodorescu *et al.* [30] studied the EHL transient contact conjunction for a one-dimensional line contact of cam to follower. Chong *et al.* [19] also applied a modified Reynolds equation considering the effect of cavitation and temperature on a lubricated cam-tappet conjunction. Applying Reynolds equation, Malik *et al.* [31] investigated the influence of lubricant film thickness and studied the effect of viscoelasticity on the lubricant behaviour together with the contact pressure prediction along piston eccentricities. For a multi-speed transmission, De la Cruz *et al.* [32] used a modified one-dimensional Reynolds equation to understand the thermal EHL lubrication properties of a gear teeth pair contact. Masjedi and Khonsari [33] also developed an EHL model for a one-dimensional line contact to investigate the traction coefficient of a lubricated contact.

## 2.3 Lubrication Stribeck curve

In tribology, as mentioned above, it is essential to be able to fundamentally understand the operating lubrication regimes of a given tribological conjunction. The literature

reviews covered in the previous section on the use of Reynolds equation to study a tribological conjunction tend to focus on a the lubrication regime dominant only to the studied physical system only. This might not be sufficient to fully explore the potential of a lubricant. In order to better understand this, the lubrication Stribeck curve, as illustrated in Figure 2.4, represents one of the more useful approach to describe lubrication regimes for the lubricant of interest. Lubrication regimes as described by the lubricant Stribeck curve includes hydrodynamic lubrication (HL), elastohydrodynamic lubrication (EHL), mixed lubrication (ML) and boundary lubrication (BL).

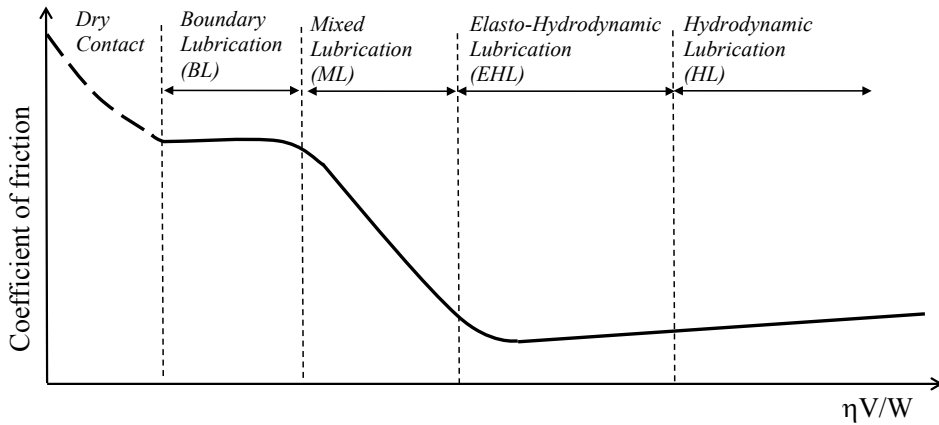


Figure 2.4: Lubrication Stribeck curve

To simulate the full range of lubrication regimes based on a lubrication Stribeck curve for a tribological contact, Hu and Zhu [34] proposed a unified numerical solution. Their numerical solution considers surface roughness of the contact profile while solving for the Reynolds equation along fluid film lubrication regime. When lubricant fluid film is depleted along BL regime, Reynolds equation is reduced in the unified solution to consider only for the dry contact. Using Bair and Winer’s approach [35] in considering non-Newtonian properties of the lubricant, Zhu and Hu further extended this unified numerical solution to predict friction, surface temperature rise and subsurface stresses along the contact [36]. More recently, Zhu *et al.* applied a similar unified numerical solution to simulate the lubrication Stribeck curve for a lubricated counter-formal rough surface contact [37]. Through this analysis, they found that contact ellipticity and roughness orientation have limited influence on frictional behaviours along HL and BL regimes.

Alternatively, Teodorescu *et al.* predicted friction generated by a cam-tappet line contact on a valve train system, operating along EHL and ML regime, using a rough surface contact model, which requires fluid film formation properties, such as contact pressure distribution and lubricant film thickness to be determined separately [38]. The lubricant film thickness separating the cam and the tappet is calculated using an empirical equation derived by Dowson [39], while the contact pressure is taken to follow Hertzian theory. Their experimentally validated friction model, which is based on Greenwood and Tripp's rough surface contact model [40], considers boundary asperity interaction along opposing rough surfaces in relative motion and also viscous shearing of entrained lubricant. They applied the Eyring limiting shear stress assumption [41] to include non-Newtonian properties of the lubricant in their calculation.

Adopting the friction model by Teodorescu *et al.* [39], Chong *et al.* investigated the tribological properties of a piston ring sliding along an engine cylinder liner for a complete engine cycle [19]. They developed a numerical solution to predict fluid film formation of the ring-liner contact based on a modified Elrod's cavitation algorithm [42]. The numerical model is shown to be capable of predicting friction along HL regime at midstroke span and ML regime at dead centre motion reversals along the ring-liner conjunction. Extending the numerical solution by Chong *et al.* [19], De la Cruz *et al.* simulated a tribological line contact of interacting gear teeth pairs under transient conditions for an automotive transmission system [32]. A modified energy equation is applied to determine the thermo-EHL properties along the gear teeth pair contact. Similar approach is also applied to study mixed thermo-EHL power loss of cam-tappet conjunction [43].

For BL regime, Chong and De la Cruz highlighted the necessity of including an accurate elastoplastic model of asperity interaction along the rough surface contact. Otherwise, underestimation of real contact area along the lubricated conjunction, operating within a boundary regime of lubrication, may occur [44]. Therefore, extending the work by Chong *et al.* [19], they introduced an improved friction model accounting for elastoplastic behaviour of interacting surface asperities along rough surfaces for a line contact solution. Their experimentally validated model, uses Greenwood and Tripp's rough surface contact as the base, takes into account surface asperity pair elastoplastic deformation. The elastoplastic asperity model follows the one derived by Jackson and Green [45], which considers the transition of the asperity contact defor-

mation from elastic to elastoplastic and finally fully plastic state.

## 2.4 Rough surface contact along mixed and boundary lubrication regimes

It is observed above that Reynolds equation is solved to determine the lubricant fluid film formation properties along line and point contact conditions. When under fluid film lubrication, friction generated along these contacts is as a result of lubricant shearing. However, when the contact undergoes ML and even BL regime, boundary interactions between surface asperities will be the significant contributor towards friction generation. For such conditions, Reynolds solution by itself is no longer sufficient in determining frictional properties of lubricated contacts as mentioned in the last chapter. Therefore, it is imperative to predict friction for a lubricated contact using a rough surface contact model. The approach requires prior calculation of fluid film formation properties, such as contact pressure distribution and lubricant film profile.

The topography of a rough surface consists of random deviation of the valleys and peak. Figure 2.5 shows the nature of rough surfaces at different length scales. Figure 2.5 (a) shows the surface feature of a typical machine shaft, while Figure 2.5 (b) is the wavy features on a selected area along the shaft. The waviness might be produced during machining as a result of vibrations of the workpiece. Zooming in further, it can be observed that at smaller length scale, irregularities appear to exist along these wavy surfaces. As the surface is being further magnified, these irregularities can now be represented by surface asperity peaks and valleys as shown in Figure 2.5 (d).

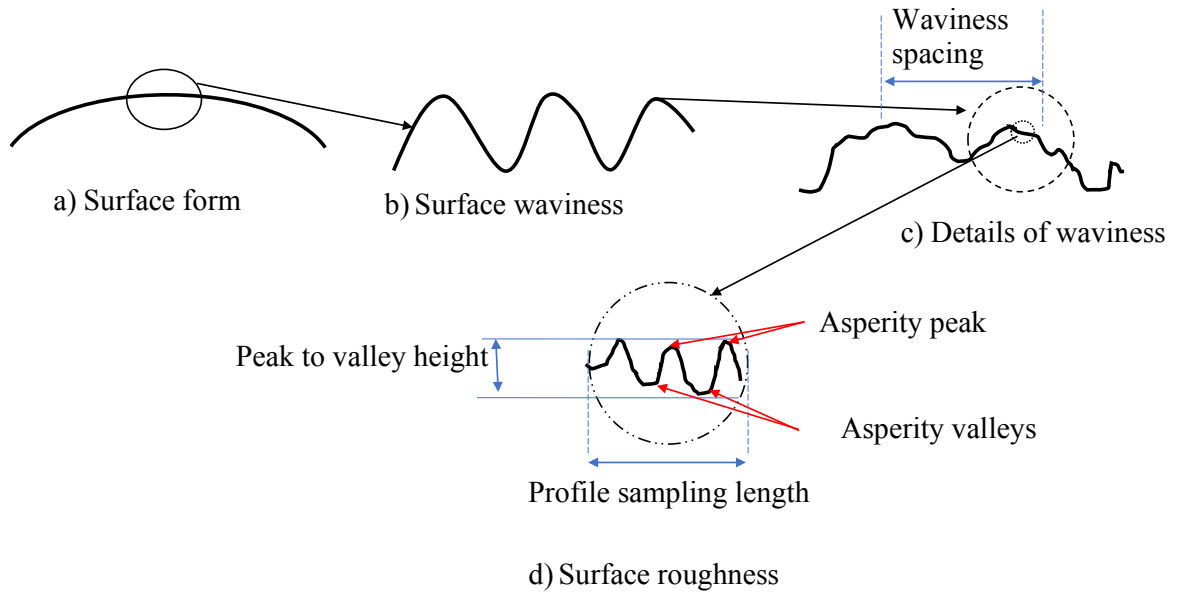


Figure 2.5: Nature of surfaces

At ML regime, friction along opposing surfaces in relative motion is generated as a result of lubricant shearing and boundary surface asperity interactions. Once the contact enters BL regime, boundary surface asperity interactions will then become the dominant underlying mechanism for friction. At such lubrication regimes, Reynolds solution will no longer be capable of accurately predicting friction of tribological conjunctions. Hence, it is imperative that a rough surface contact model be applied to determine such boundary friction properties. This chapter will focus on the implementation of a rough surface contact model, which will be coupled with the Reynolds solution from the previous chapter in order to ascertain the tribological properties of a lubricated contact for the full range of lubrication regimes.

In earlier generation of rough surface contact theories, the common assumption made takes the real contact area of two nominally flat surfaces based on plastic deformation of their highest asperity peaks. However, Archard pointed out that such assumption could not be the universal rule [46]. Instead, he introduced a rough surface contact model, where the area of contact could be proportional to the load even with purely elastic contact. Based on Archard's model, Greenwood and Williamson further investigated the contact of nominally flats surfaces [47]. It was realised through Green-

wood and Williamson’s investigation that contact deformation highly depends on the topography of the surface, where an ‘elastic contact hardness’ exists along the contact area. Through this, a criterion for distinguishing surfaces that touch elastically from those that touch plastically was established. Greenwood and Williamson also concluded that contact of opposing surfaces is controlled by material properties (e.g. shear elastic modulus and hardness) and topography properties (e.g. surface density, standard deviation of height distribution and mean radius of the asperities).

Extending the work by Greenwood and Williamson [47], Greenwood and Tripp found that the contact of two opposing rough surfaces can be simplified to an equivalent single rough surface model [48]. In their study, they used the two rough surface model as an initial study. They found that the difference between an equivalent single rough surface and two opposing rough surfaces is simply (a) the replacement of the actual single-contact laws by generalized laws, obtained by integrating the actual deformation laws over all possible radial misalignments and (b) the replacement of the distribution of asperity heights by the distribution of sums of pairs of heights.

For the rough surface contact models mentioned above, surface asperity interactions are determined using the Hertzian theory. In a later study, Greenwood [49] focused on understanding the possible errors, which might have been incurred when Hertzian theory is used to calculate the contact stress and the contact area of rough surfaces. A non-dimensional term,  $\alpha$ , was introduced to study the effect of surface roughness on the contact area and stress in a Hertzian contact of spherical bodies. They showed that as long as the non-dimensional term,  $\alpha$  is less than 0.05, Hertzian assumption for spherical asperity deformation along rough surface contact should be able to give a good representation of the realistic physical problem.

Surface asperity height, slope and curvature variances, similar to Greenwood and Williamson’s rough surface contact model, are commonly used to describe the deviation of a surface from its mean plane [50]. However, Greenwood-Williamson’s model is found to not be applicable to all micro-contact sizes, where rough surfaces are only represented at narrow-band rough surface and a wide-band smooth counter-surface [50]. Sayles and Thomas observed that topography of typical engineering surfaces is not unique for a particular surface and is often related to the length of the measured sample [51]. Such observation is further supported by Thomas [52], where the slope and the curvature of a surface topography exhibited strong dependence on the resolution of instrument



used to measure the surface roughness.

To allow for surface roughness to be characterised at any length scale, Majumdar and Tien adopted the Weierstrass-Mandelbrot (W-M) fractal function to introduce a simplistic method to characterise the multi scale structure of a rough surface [53]. Yan and Komvoupoulos also applied a similar approach to investigate the effects of surface topography parameters and material properties on the total deformation force along rough surface contacts [54]. More recently, Jackson and Streater presented a non-statistical multi-scale model of the normal contact between rough surfaces [55]. The model is capable of predicting contact area as a function of contact load. It is shown that the model produced trends similar to that of the traditional Greenwood and Williamson [47] and Majumdar and Bhushan (MB)[18] rough surface contact models. They also observed that the model seemed to not be largely affected by the sampling resolution at the employed surface data.

The above mentioned rough surface contact models consider perfectly dry rough surface contacts. For contact under EHL regime, Johnson *et al.* presented a simple asperity contact model [56]. They applied Greenwood and Williamson's rough surface contact model [47] along with Dowson and Higginson's EHL study [28] in simulating a rough surface contact under EHL. They found that the actual mean separation of the surfaces is nearly equal to the lubricant film thickness along the smooth surfaces under consistent operating condition. This shows that the separation, upon which the asperity contact conditions depend on, can be determined directly from the EHL conditions, independent of the surface roughness.

## 2.5 Alternative lubricants - biolubricants

The covered literature review above discussed on the fluid film formation and frictional properties of typical lubricated conjunctions. However, typical lubricants are mostly mineral oil based, requiring synthetic additives, which could possibly lead to emissions of toxic pollutants if not handled properly. Hence, it is essential to embrace the Green Tribology concept, where the use of biodegradable lubrication could prove to pivotal in decarbonising the transportation sector. One of the possible alternatives is biodiesel.

Biodiesel is generally produced by alkaline catalyzed transesterification of vegetable oils or animal fats with monohydric low molecular weight alcohols [57], but commer-

cial biodiesels are mainly fatty acid methyl esters (FAME). The effect of individual components of fatty acid methyl ester (FAME) on petro-diesel fuel lubrication properties has been investigated by Geller and Goodrum [58] using the High Frequency Reciprocating Rig (HFRR). The study looks into lubrication property enhancements of petro-diesel fuel when added with small concentrations of pure FAME and vegetable oil derived FAME. From their study, they found no consistent trend relating chain length to petro-diesel fuel lubrication property enhancement when FAMEs are added to this fuel. However, vegetable oil derived FAME mixtures have been observed to consistently produce better lubrication performance than their single fatty acid based counterparts when mixed with petro-diesel fuel. It can also be surmised through the study that vegetable oil based additives follow the same pattern as the predominant component of FAME in each oil.

In a similar study, Goodrum and Geller observed that lubrication property enhancement for petro-diesel fuel can be improved by adding small concentrations of vegetable oil derived FAME, consisting of hydroxylated and mono-unsaturated components [59]. Nicolau *et al.* evaluated the relation between lubrication properties and electrical impedance properties of a series of petro-diesel fuel samples with different sulfur content and low sulfur diesel/biodiesel blends [60]. They characterised the fuel samples by obtaining a linear correlation between electrical resistivity and wear scar diameter. Hazrat *et al.* also investigated the lubrication performance improvements on ultra-low sulphur petro-diesel fuel when blended with various biodiesels and vegetable oils [61]. Their study found that biodiesel blends up to 20% with the ultra-low sulphur petro-diesel fuel can effectively reduce both the wear of the tribo-contact surfaces as well as the friction coefficient.

Generally, low level blending of FAME on ultra-low sulphur petro-diesel has been observed to be capable of restoring the lubrication properties of such fuel. Knothe and Steidley studied the lubrication properties of numerous fatty acid compounds and compared them with hydrocarbon compounds found in petro-diesel [62]. The effects of blending compounds found in FAME on petrodiesel lubrication properties are also studied. Using HFRR for their friction tests, it is found that fatty acid compounds possess better lubrication properties than hydrocarbons because of their polarity imparting oxygen atoms. They also noticed that lubrication properties improve with the presence of double bonds within the fatty acid compounds. However, in their

study, they also observed that some compounds (free fatty acids, monoacylglycerols), typically considered as contaminants resulting from biodiesel production, could also be responsible for lubrication property enhancements of ultra-low sulphur petro-diesel fuel.

The tribological properties obtained in the above mentioned studies revolve around blending of vegetable oil derived biodiesel with petro-diesel using HFRR, focusing more on the wear scar on the lubricated surfaces. Alternatively, Maru *et al.* use lubrication Stribeck curves to characterise the lubrication properties of vegetable oil derived biodiesel [63]. The characteristic curve is measured using a tribometer with a ball-on-disc configuration. The study also included friction measurements for petro-diesel fuel blended with biodiesel. Through this study, they found that lubrication properties are better depicted by the Stribeck test method because of its friction response from the point of view of energy loss from the dynamic system. The measured Stribeck curves show that the major difference, in terms of lubrication performance, among the tested fuels occurs along the low sliding velocity range or in the start-stop stage of moving components. They found that the poorest lubrication performance is attained with the neat diesel fuel and the best lubrication performance is attained with animal fat derived biodiesel.

## 2.6 Application specific-modifications to Reynolds equation

Fluid film formation for lubricated contacts is typically determined using Reynolds equation. However, a few deficiencies have been pointed out since the inception of this equation, requiring modifications depending on the type of application. For example, classical Reynolds equation has been shown to not be able to account for negative pressure in the diverging part of the contact as a result of cavitation. Cavitation is one of the most important phenomena in thin film lubrication problems and it is defined as the rupture of the continuous lubricant film due to the formation of air bubbles. Two possible solutions on the outlet pressure have been proposed initially by using atmospheric pressure [64] or cavitation pressure [65]. Unfortunately, this method could not fulfil the cavitation region even though it is a rapid method.

Using the Jakobsson and Floberg [17] together with Olsson [18], known as the JFO theory, a modified Reynolds equation with a new set of boundary conditions is introduced. This method has been shown to be capable of describing the Reynolds equation in a full film region. However, in the cavitation region, the film breaks down and lubricant behaviour is predicted using the continuity of flow. One of the more common cavitation algorithm used in tribological investigations is proposed by Elrod [66]. The algorithm includes the influence of two phase flow or cavity formation into the Reynolds equation. The modified Reynolds equation can be written as follow:

$$\frac{\partial}{\partial x} \left( \frac{\rho_c h^3}{\eta} g \beta \frac{d\theta}{dx} \right) = 12 \left\{ \frac{\partial}{\partial x} [\theta \rho_c h (u_{av})] + \frac{d}{dt} (\theta \rho_c h) \right\} \quad (2.3)$$

where  $\rho_c$  is a Non-dimensional lubricant density at  $p = p_c$  and constant temperature (-),  $g$  is switch function and defined by Elrod [66] as :

$$g = \begin{cases} 0, & \text{if } \theta < 1. \\ 1, & \text{if } \theta \geq 1. \end{cases} \quad (2.4)$$

This function is important to ensure consistency of the result between the cavitated region and the uniform pressure assumption [67].  $\beta$  is lubricant bulk modulus (Pa.s) and  $\theta$  is fractional film content-cavitation, if  $h < 1.0$ .

The original Reynolds equation considers only perfectly smooth condition for the opposing surfaces in relative motion. To consider for the effect of surface roughness along lubricated contact, Patir and Cheng [68] modified the Reynolds equation to take into consideration shear flow factors as a result of lubricant entrainment across surface feature Reynolds. This method is applied to find the hydrodynamic load capacity used in iso-viscous and compressible film. The pressure flow factors are derived and introduced in the generalized Reynolds equation together with roughness parameter. The average Reynolds equation is used to find the hydrodynamic load and attitude angle, such as for a gas journal bearing in various journal speeds, rough parameters, and surface pattern parameters. The average Reynolds equation can be written as follow:

$$\frac{\partial}{\partial x} \left( \Phi_x \frac{h^3}{12\eta} \rho \frac{\partial p}{\partial x} \right) + \frac{\partial}{\partial y} \left( \Phi_y \frac{h^3}{12\eta} \rho \frac{\partial p}{\partial y} \right) = u \frac{\partial}{\partial x} (\rho h_T) + \frac{\partial (\rho h_T)}{\partial t} \quad (2.5)$$

where  $\Phi_x$ ,  $\Phi_y$  are pressure flow factors and  $h_T$  is the average gap.

Sahlin *et al.* [69] also described a method of homogenization technique for compressible Reynolds equation for rough surfaces. They introduced a two-scale expansion, involved in the homogenization process, to enable the local roughness scale to be treated separately from the global geometry scale. Using this method, the flow factors could be computed for any deterministic roughness. To compensate the surface roughness, method derived by Patir and Cheng [68] is used. They rewrite the Reynolds equation in terms of the averaged flow factors for control volumes and is applicable to any roughness structure. This flow factors are computed for an arbitrary periodic two or three-dimensional roughness, permitting the use of measured surface topographies of real surfaces. The modified Reynolds equation can be described as:

$$\frac{d}{dx} \left( h^3 \frac{d\theta}{dx} \right) = \Gamma \frac{d(\theta h)}{dx} \quad (2.6)$$

where  $\Gamma = 6^* \eta u / \beta$  ( $\eta$  =dynamic viscosity,  $u$  =surface velocity in the x-direction, m/s pressure,  $\beta$ =bulk modulus),  $\theta$  is exponential expression. Based on Patir and Cheng's [68] approach, Rahmani *et al.* [70] proposed an analytical solution to study the influence of surface texturing on the friction of slider bearings. Their approach is recently extended to predict friction along the ring/liner conjunction [71].

Recently, Bayada *et al.* investigated the tribological contact problem considering both the oscillating roughness and cavitation effect [72]. In their study, they applied the Elrod-Adams [73] approach, where cavitation region is taken to be a fluid-air mixture, described based on the saturation of the fluid mixture. They proposed a modified Reynolds equation, known as the *exact* Reynolds equation with cavitation. The alternative Reynolds equation deduced by Bayada *et al.* [72] is as follow:

$$\frac{\partial}{\partial x} \left\{ \left( \frac{h^3}{\mu} - 12\alpha \left( \frac{vh^2}{30} - \frac{Qh}{10} \right) \right) \frac{\partial p}{\partial x} \right\} = 6v \frac{dh}{dx} \quad (2.7)$$

where  $\alpha$ =piezoviscosity coefficient,  $Q$  is a flow rate.

The aforementioned modifications of the classical Reynolds equation considers typical lubricants (mostly mineral oil based) being entrained into the sliding contact. With the advancements of technology, lubrication of sliding of contacts might no longer depend purely of mineral oil based lubricants. Lubricants in the form of gas and water

have also been widely explored. In order to determine the fluid film formation properties of such lubricants, for gas lubricated contact, Burgdorfer proposed a modified Reynolds equation based on the concept of kinetic theory in gas film lubrication [74]. Alternatively, Fukui and Kaneko derived a modified Reynolds equation using a linearised Boltzman equation, describing flow of gas lubrication using Knudsen number [75]. A similar approach for gas lubricated contact is also applied by Hwang *et al.* [76], Veijola *et al.* [77] and Stevanović *et al.*[78]. Later, Bahukudumbi and Beskok developed a modified slip boundary condition for steady plane Couette flow and slip-corrected Reynolds lubrication equation for the entire Knudsen regime for gas lubricated conjunctions [79]. The modified slip-corrected Reynolds equation as per discussed by Bahukudumbi and Beskok are given as follow [79]:

$$\frac{\partial}{\partial x} \left\{ (1 + \alpha K_n) \left( 1 + \frac{6K_n}{1 + K_n} \right) h^3 p \frac{\partial p}{\partial x} \right\} = 6\mu_0 \frac{\partial}{\partial x} (phU_0) \quad (2.8)$$

where  $\alpha$  is rarefaction correction parameter,  $K_n$  is Knudsen number.

For water-lubricated journal bearing, Armentrout *et al.* investigated the influence of turbulence and convective fluid inertia along this tribological conjunction [80]. They applied two types of models Reynolds equation, computed by traditional lubrication theory and Computational Fluid Dynamics (CFD), containing a full Navier-Stokes solution. They found good agreement between the Reynolds solution and CFD solution as long as a turbulence model is prescribed to both approaches. Therefore, they proposed an adjustment scheme over a range of bearing sizes, leading to a generalise Reynolds equation as follow:

$$\frac{\partial}{\partial x} \left\{ \Gamma(x, z) \frac{\partial p}{\partial x} \right\} + \frac{\partial}{\partial z} \left\{ \Gamma(x, z) \frac{\partial p}{\partial z} \right\} = -U \frac{\partial}{\partial x} G(x, z) \quad (2.9)$$

where  $\Gamma(x, z)$  represents the function of circumferential coordinate ( $x$ ), and the axial coordinate ( $z$ ).

From the literature review covered, it is also realised that no work has yet been reported related to the development of mathematical tools to predict the fluid film formation and also the frictional properties of biodiesel. Therefore, the study attempts to simulate for a point contact lubricated with biodiesel.

## 2.7 Measurements of tribological properties

One of the most commonly used tribometer is configured for a pin-on-disc or pin-on-plate setup. This apparatus can be used to simulate continuous or intermittent motions, unidirectional or reciprocating movements between surfaces [81]. There are numerous standard test methods for investigation of scuffing in lubricated tribosystems [82]. The pin-on-disc setup involves a stagnant pin, which is loaded against a rotating disc. The pin-on-disc tribometer quantifies friction and wear properties for dry and/or lubricated surfaces under pure sliding [83]. As for the pin-on-plate, a pin is loaded against a plate, sliding in a linear reciprocating form. These two configurations are shown in Figure 2.6.

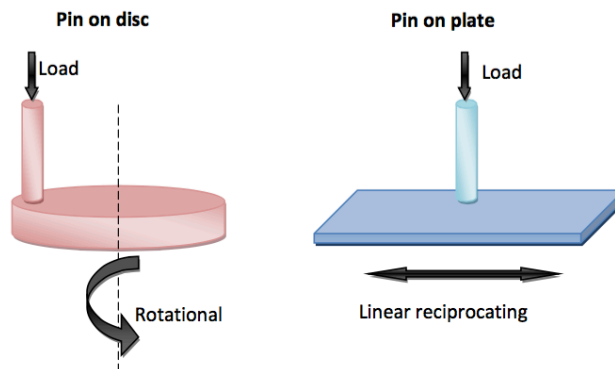


Figure 2.6: Configuration of tribometer pin-on-disc and pin-on-plate

Alternatively, Plint Te-77 can also be used to measure frictional properties under linear reciprocating motion. The apparatus measures the applied normal load using a strain gauge transducer. Contact pressure and contact area at the interface are varied with applied normal load. These parameters can be theoretically determined using the Hertzian contact assumptions. Many researchers, including Covert et al. [84] and Bonny et al. [85] have used this tribometer, as shown in Figure 2.7, to study the tribological characteristics at different applied normal loads.

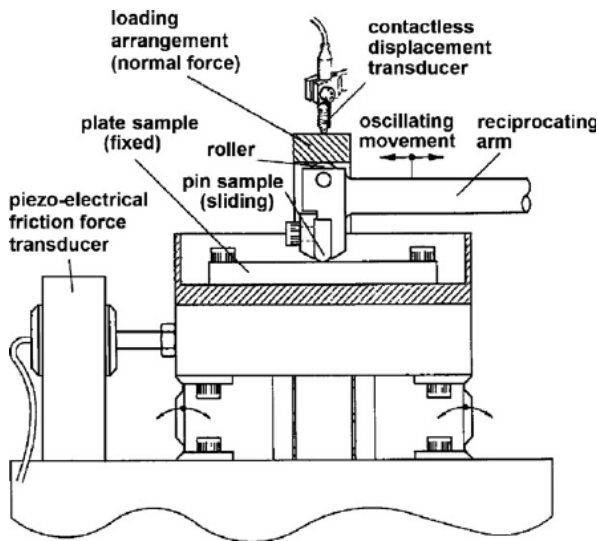


Figure 2.7: Schematic outline of Plint TE 77 reciprocating pin-on-plate tribometer [85]

For studies related to extreme pressure condition, a four-ball tribosystem is commonly used [86, 87]. This machine consists of three stationary steel balls being pressed by the upper ball in the presence of a lubricant to be tested at continuously increasing load. The upper ball rotates at a constant speed in either rolling or sliding motion (see Figure 2.8). The lower fixed balls are held in position against each other in a steel cup by a clamping ring and locking nut. The frictional torque exerted on the three lower balls can be measured by a calibrated arm, which is connected to the spring of a friction recording device [87, 82].

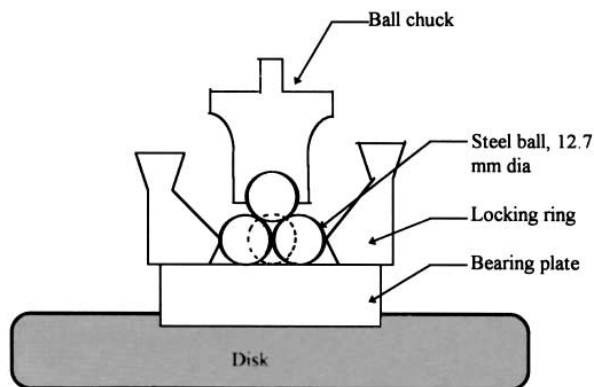


Figure 2.8: Schematic diagram of the four-ball wear machine.[87]



Mini traction machine (MTM) is another type of tribometer, meant mainly for lubricated point contacts. The MTM is shown in Figure 2.9. The equipment comprises a ball and a disc in contact, moved by independent axes, submerged in a reservoir full of lubricant at a controlled temperature. Therefore, both ball and disc can rotate independently at different rotational speeds [88, 89]. Using MTM, Morgado et al. [88] investigated the parameters influencing lubricant behaviour such as sliding velocity, temperature and applied normal load for contact lubricated with mineral lubricant. On the other hand, Pejakovic et al. [89] also used MTM to identify the friction behaviour of ionic liquid.

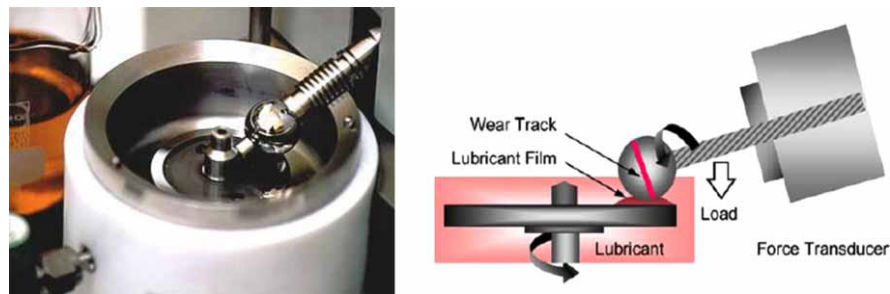


Figure 2.9: Photograph and diagram of the test zone in the MTM.[88]

As the focus of this study is to investigate pure-sliding condition at constant sliding velocity, pin-on-disc tribometer has been chosen. This machine also provides for better freedom in material selection for pin and disc setup.

## 2.8 Summary

In this chapter, a literature review has been conducted with relation to the fundamentals of Tribology, highlighting on the application of Reynolds equation to understand lubrication fluid film formation along a lubricated conjunction. Lubrication Stribeck curve is also discussed with respect to the different lubricant regimes, namely HL, EHL, ML and BL. Various mathematical methods in analysing a tribological conjunction across the whole range of lubrication regimes have also been reviewed. The importance of considering alternative lubricants, such as biodiesel, has also been discussed in this chapter, emphasising on a lack of intensive tribological fundamental knowledge on the use of biodiesel as lubricant.

# Chapter 3

## Numerical Approach for Friction Prediction

### 3.1 Fluid film formation prediction based on Reynolds Solution

In this chapter, the focus is to determine the lubricant fluid film formation properties along tribological conjunctions using Reynolds equation. Therefore, as an initial approach to better understand lubricant fluid film formation properties, such as contact pressure distribution and lubricant film profile, a two-dimensional Reynolds equation is applied. Figure 3.1 shows a typical point contact tribological problem, which represents application such as a ball bearing conjunction in an engine. The two-dimensional Reynolds equation can be expressed as follow:

$$\frac{\partial}{\partial x} \left[ \frac{\rho h^3}{12\eta} \frac{\partial p}{\partial x} \right] + \frac{\partial}{\partial y} \left[ \frac{\rho h^3}{12\eta} \frac{\partial p}{\partial y} \right] = 12 \left\{ \frac{\partial}{\partial x} \left[ \frac{\rho h(u_A + u_B)}{2} \right] + \frac{\partial}{\partial y} \left[ \frac{\rho h(v_A + v_B)}{2} \right] + \frac{\partial \rho h}{\partial t} \right\} \quad (3.1)$$

where  $h$  as shown in Figure 3.1 refers to the lubricant film profile and can be expressed as and [90]:

$$h = h_0 + h_s(x, y) + \delta(x, y) \quad (3.2)$$

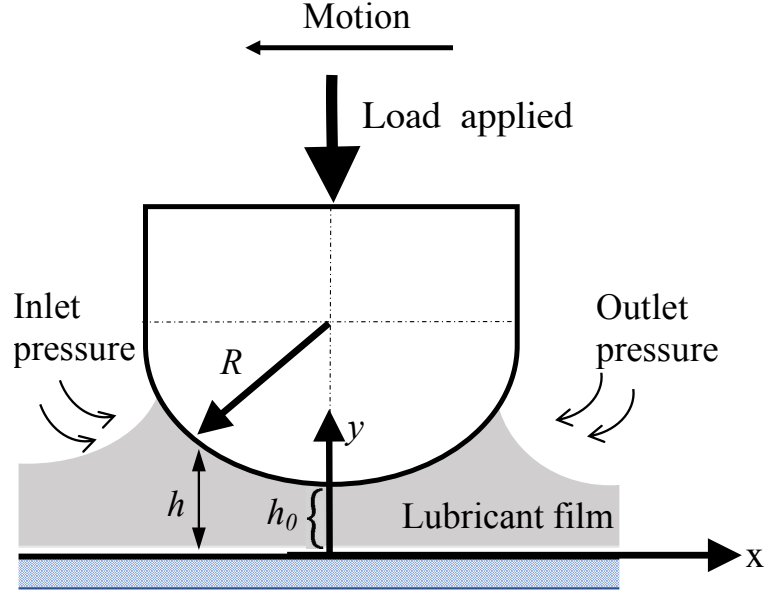


Figure 3.1: Point contact conjunction.

The term  $h_s$  refers to the local gap at any location along the contact conjunction while the term  $h_0$  refers to the initial underformed central separation gap. The term  $\delta$  is the elastic deformation of the contact geometry. The elastic deformation term,  $\delta(x, y)$  is given as:

$$\delta(x, y) = \frac{1}{\pi E^*} \iint \frac{p(x', y')}{\sqrt{(x - x')^2 + (y - y')^2}} dx' dy' \quad (3.3)$$

where  $p$  is the pressure applied at computation location  $(x', y')$ . The deflection at location  $(x, y)$  is computed as a result of all the generated pressures at points  $(x', y')$ . When a computational grid is made with the pressure distribution,  $p_{k,l}$ , this equation can be defined as:

$$\delta_{i,j} = \sum_k \sum_l D_{i,j}^{k,l} p_{k,l} \quad (3.4)$$

where  $D_{i,j}^{k,l}$  are the influence coefficients as given in reference [?]. It is to note that elastic deflection will become important when the contact pressure exerted onto the lubricant is high (typically in GPa range). During this, the viscosity and density of the lubricant will no longer remain constant [91]. It is also in the interest of this study to apply the Reynolds equation for the full range of fluid film lubrication regime, where lubricant viscosity and density change with contact pressure will be essential along the EHL lubrication regime. Hence, the lubricant viscosity-pressure relation used for typical mineral oil based lubricant is given by Roelands [92] as :

$$\eta = \eta_0 e^{(\alpha p)} \quad (3.5)$$

where  $\alpha = (\ln \eta_0 + 9.67)[1 + p/(1.98 \times 10^8)]^z - 1/p$  and  $z = \alpha_0/[5.1 \times 10^{-9}](\ln \eta_0 + 9.67)$  and  $\eta_0$  is known as viscosity at ambient pressure. As for lubricant density variation with contact pressure, Dowson and Higginson gives the relation for mineral oil based lubricant as follow [28]:

$$\rho = \rho_0 \left\{ 1 + \frac{0.6 \times 10^{-9} p}{1 + 1.7 \times 10^{-9} p} \right\} \quad (3.6)$$

where  $\rho_0$  is known as density at ambient pressure.

## 3.2 Discretisation of Reynolds equation

To solve for the Reynolds equation, Reynolds exit boundary condition is applied. This boundary condition states that at exit boundary along sliding direction is:

$$p = \frac{dp}{dx} = 0 \quad (3.7)$$

Using the Reynolds exit boundary condition, to ease the calculation of contact pressure

and lubricant film thickness, the Reynolds equation is first non-dimensionalised as follow (refer *Appendix A* for complete non-dimensional properties):

$$\frac{\partial}{\partial X} \left( \frac{\bar{\rho} H^3}{\bar{\eta}} \frac{\partial P}{\partial X} \right)_{i,j} + k^2 \frac{\partial}{\partial Y} \left( \frac{\bar{\rho} H^3}{\bar{\eta}} \frac{\partial P}{\partial Y} \right)_{i,j} = \Psi \left( \left[ \frac{\partial(\bar{\rho} H U)}{\partial X} \right]_{i,j} + \left[ \frac{\partial(\bar{\rho} H V)}{\partial Y} \right]_{i,j} + \frac{R_x \bar{\rho}}{b} S^* \right) \quad (3.8)$$

where

$$\Psi = 12 \frac{u_{av} \eta_0 R_x^2}{P_h b^3}, S^* = \frac{\partial h / \partial t}{u_{av}}, k = \frac{b}{a} \quad (3.9)$$

The partial differential components in the non-dimensional Reynolds equation is then expanded using finite difference method. The finite difference method approximates the differential operator by replacing the derivatives using differential quotients. Hence, this gives:

$$\underbrace{\frac{\partial}{\partial X} \left( \frac{\bar{\rho} H^3}{\bar{\eta}} \frac{\partial P}{\partial X} \right)_{i,j}}_A + i k^2 \underbrace{\frac{\partial}{\partial Y} \left( \frac{\bar{\rho} H^3}{\bar{\eta}} \frac{\partial P}{\partial Y} \right)_{i,j}}_B = \psi \left( \left[ \underbrace{\frac{\partial(\bar{\rho} H U)}{\partial X}}_C \right]_{i,j} + \left[ \underbrace{\frac{\partial(\bar{\rho} H V)}{\partial Y}}_D \right]_{i,j} + \frac{R_x \bar{\rho}}{b} S^* \right)$$

The adoption of the finite difference strategy on the non-dimensional Reynolds equation can be summarised as follow:

- Central finite difference method is applied on the left hand side term or the *Poiseuille* term.
- Finite difference method for the terms on the right hand side or the *Coutte* term (excluding the squeeze term) is based on the weight factor,  $\beta$  with: 1) forward difference method being used when  $\beta = 0$ ; 2) backward difference method being used when  $\beta = 1$ ; 3) central difference method being used when  $\beta = 0.5$ .

For this numerical scheme, it is found that backward difference method produces a more stable numerical solution, where better numerical convergence can be achieved.

### 3.3 Numerical scheme

Moving all the terms to one side of the equation gives the residual term,  $F_{i,j}$ . This term enables the application of modified Newton-Raphson approach, where roots of the function can be approximated where the residual term,  $F \approx 0$ .

$$\begin{aligned}
F_{i,j} = & \frac{1}{2\Delta X^2} \left\{ \left[ \left( \frac{\bar{\rho}H^3}{\bar{\eta}} \right)_{i,j} - \left( \frac{\bar{\rho}H^3}{\bar{\eta}} \right)_{i-1,j} \right] P_{i-1,j} \right. \\
& - \left[ \left( \frac{\bar{\rho}H^3}{\bar{\eta}} \right)_{i,j} + 2 \left( \frac{\bar{\rho}H^3}{\bar{\eta}} \right)_{i,j} + \left( \frac{\bar{\rho}H^3}{\bar{\eta}} \right)_{i,j} \right] P_{i,j} \\
& \left. + \left[ \left( \frac{\bar{\rho}H^3}{\bar{\eta}} \right)_{i+1,j} + \left( \frac{\bar{\rho}H^3}{\bar{\eta}} \right)_{i,j} \right] P_{i+1,j} \right\} \\
& + \frac{k^2}{2\Delta Y^2} \left\{ \left[ \left( \frac{\bar{\rho}H^3}{\bar{\eta}} \right)_{i,j} - \left( \frac{\bar{\rho}H^3}{\bar{\eta}} \right)_{i,j-1} \right] P_{i,j-1} + \left[ \left( \frac{\bar{\rho}H^3}{\bar{\eta}} \right)_{i,j} - \left( \frac{\bar{\rho}H^3}{\bar{\eta}} \right)_{i,j+1} \right] P_{i,j+1} \right. \\
& \left. - \left[ \left( \frac{\bar{\rho}H^3}{\bar{\eta}} \right)_{i,j+1} + 2 \left( \frac{\bar{\rho}H^3}{\bar{\eta}} \right)_{i,j} + \left( \frac{\bar{\rho}H^3}{\bar{\eta}} \right)_{i,j-1} \right] P_{i,j} \right\} \\
& - (1 - \beta_x) \frac{(\bar{\rho}HU)_{i+1,j} - (\bar{\rho}HU)_{i,j}}{\Delta X} + \beta_x \frac{(\bar{\rho}HU)_{i,j} - (\bar{\rho}HU)_{i-1,j}}{\Delta X} \\
& - (1 - \beta_y) \frac{(\bar{\rho}HV^*)_{i+1,j} - (\bar{\rho}HV^*)_{i,j}}{\Delta Y} + \beta_y \frac{(\bar{\rho}HV^*)_{i,j} - (\bar{\rho}HV^*)_{i-1,j}}{\Delta Y} \\
& - \psi \frac{R_x}{b} (\bar{\rho}S^*)_{i,j}
\end{aligned} \tag{3.10}$$

In order to implement the intended modified Newton-Raphson method, equation (A.9) is first expanded using Taylor's series:

$$\begin{aligned}
\bar{F}_{i,j} = & F_{i,j} + \frac{\partial F_{i,j}}{\partial P_{i+1,j}} \Delta P_{i+1,j} + \frac{\partial F_{i,j}}{\partial P_{i-1,j}} \Delta P_{i-1,j} + \frac{\partial F_{i,j}}{\partial P_{i,j}} \Delta P_{i,j} \\
& + \frac{\partial F_{i,j}}{\partial P_{i,j+1}} \Delta P_{i,j+1} + \frac{\partial F_{i,j}}{\partial P_{i,j-1}} \Delta P_{i,j-1} + Err = 0
\end{aligned} \tag{3.11}$$

where  $\Delta P_{i,j} = \bar{P}_{i,j} - P_{i,j}$ . Assuming that the truncating error is small enough to be neglected, equation (3.12) can be rewritten as:

$$\begin{aligned}
-F_{i,j} &= \bar{J}_{ij,i-1j}\Delta P_{i-1,j} + \bar{J}_{ij,i+1j}\Delta P_{i+1,j} + \bar{J}_{ij,ij-1}\Delta P_{i,j-1} \\
&\quad + \bar{J}_{ij,ij+1}\Delta P_{i,j+1} + \bar{J}_{ij,ij}\Delta P_{i,j} + Err
\end{aligned} \tag{3.12}$$

where  $\bar{J}_{ij,kl} = \frac{\partial F_{i,j}}{\partial P_{k,l}}$ . The term  $\Delta P_{k,l}^n$  is calculated using

$$\Delta P_{k,l}^n = \frac{-J[5] - J[1]\Delta P_{k-1,l}^n - J[0]\Delta P_{k+1,l}^{n-1} - J[3]\Delta P_{k,l-1}^n - J[2]\Delta P_{k,l+1}^{n-1}}{J[4]} \tag{3.13}$$

The components of the Jacobian matrix are derived and given in *Appendix A*. For a given undeformed central separation gap,  $h_0$  and sliding velocity, the numerical scheme is then solved using Gauss-Seidel iterative method with the contact pressure term being relaxed using:

$$P_{i,j}^n = P_{i,j}^{n-1} + \Omega \Delta P_{i,j}^n \tag{3.14}$$

Once the solution for the contact pressure is obtained, the load carried by the contact can be calculated by integrating the contact pressure:

$$W = \int_{-\infty}^{\infty} P dX \tag{3.15}$$

The flow chart summarising the numerical scheme for solving the Reynolds equation based on the discussed iterative algorithm above is given in Figure 3.2. It is to note that the discussed iterative algorithm is programmed using C-language. The iterative calculation can then be repeated for different operating conditions, such as sliding velocity and applied normal load. Convergence to applied normal load can be achieved by adjusting the undeformed central separation gap,  $h_0$ . The term  $\Omega$  refers to the relaxation coefficient. For this study, it is realised that under relaxation ( $\Omega < 1$ ) allows for convergence of the numerical solution.

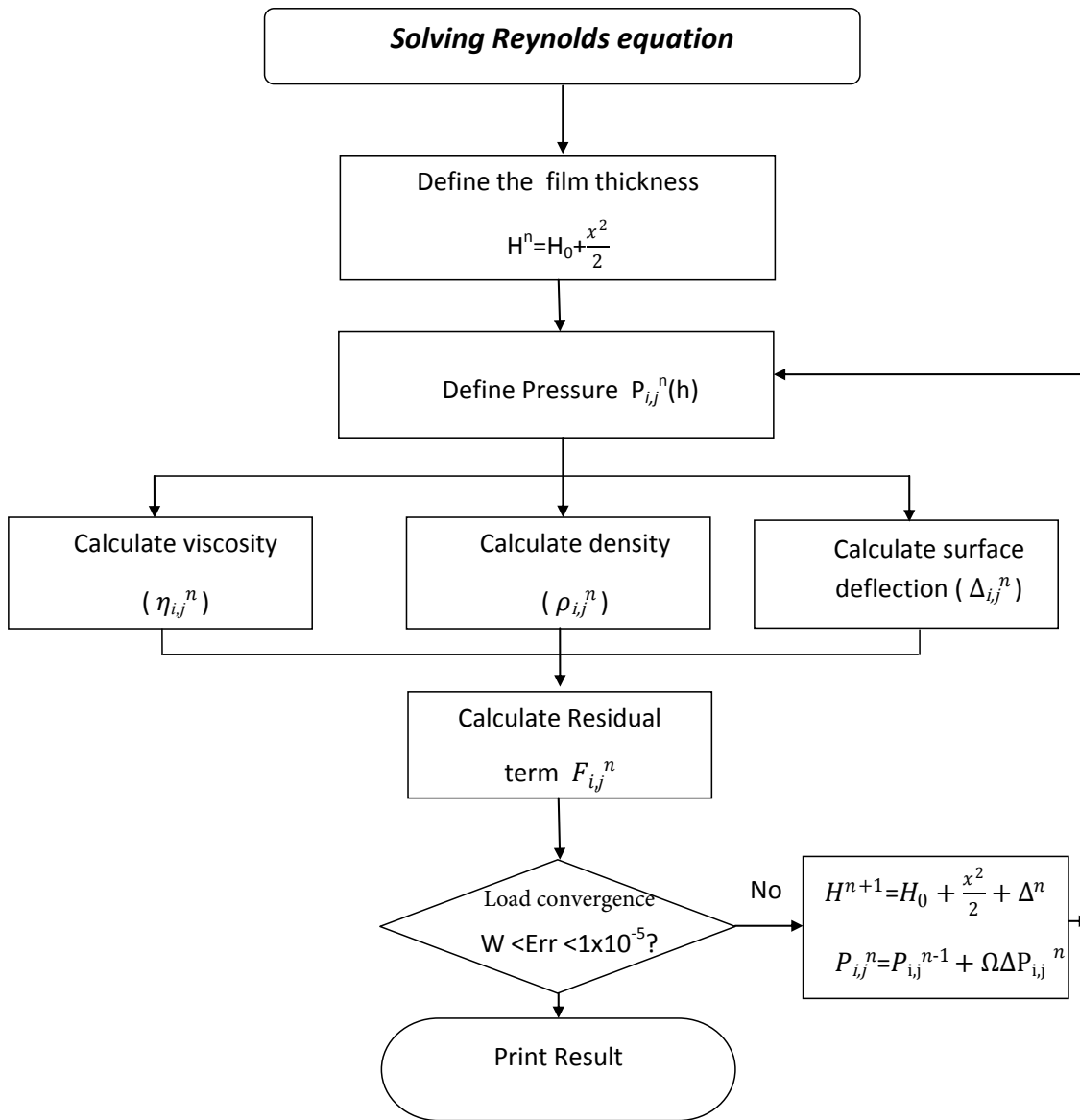


Figure 3.2: Flow chart of Reynolds equation iterative solution

### 3.4 Rough surface contact model

The current study adopts the friction predictive method similar to the one proposed by Teodorescu *et al.* [38], where a rough surface contact model is applied to determine the



frictional characteristics of a lubricated contact based on the lubricant fluid film formation properties, namely the contact pressure distribution and lubricant film thickness. The first step to simulate the tribological properties of commercially available SAE grade lubricants across the whole range of lubrication regimes is to use a numerical model for a two-dimensional Reynolds equation to determine the lubricant fluid film formation properties for a lubricated point contact. Only once these properties are determined, the frictional characteristics of such contact can be obtained using a rough surface contact model, which will be discussed in the next chapter. The parameters used in the simulation are provided in Table 3.1.

Table 3.1: Simulated tribological conjunction for point contact

<b>Parameter</b>	<b>Values</b>	<b>Units</b>
Curvature radius	5.0	mm
Young's modulus (flat surface)	210.0	GPa
Poisson's ratio (flat surface)	0.27	-
Young's modulus (pin with spherical end cap)	110.0	GPa
Poisson's ratio (pin with spherical end cap)	0.21	-
Applied normal load,	20	N

In the current study, friction along lubricated contact is taken to consist of viscous shear and boundary shear components. For a lubricated contact, fluid film lubrication plays an important role in HL and EHL regime. However, when the contact is in ML regime, fluid film could break down at surface asperity conjunction. In order to be able to predict friction along various lubrication regimes, the total friction for a lubricated rough surface contact can be described as:

$$f_{tot} = \int_{inlet}^{outlet} (df_v + df_b) dA_{app} \quad (3.16)$$

The term  $dA_{app}$  refers to the apparent contact area, while the term  $df_v$  refers to the viscous friction. Viscous friction dominates when the lubricant film is thick and pure shearing of the film occurs. However, when the lubricant film is thin, contact between the asperities could no longer be avoided. Therefore, the term  $df_b$ , which refers to the boundary friction component, exists as a result of the interaction between surface asperities. Boundary friction  $df_b$  can be determined as follow:

$$df_b = dA_a \left[ \tau_0 + \kappa \frac{dW_a}{dA_a} \right] \quad (3.17)$$

with  $dW_a$  being the total load carried by the surface asperities and  $dA_a$  being the actual contact area. The term  $\tau_0$  refers to the Eyring limiting shear stress of the lubricant, while the term  $\kappa$  refers to the pressure coefficient for boundary shear strength of the bounding surfaces.

In deriving the friction model, Greenwood and Williamson's fundamental theories of elastic contact and friction for rough surfaces are adopted. The model demonstrated dependency of the contact on the surface topography. Further findings by Greenwood and Tripp [48] emphasized on the fact that a two-rough surface model could have a similar behavior with a single rough surface model (see Figure 3.3). As a result of surface feature interactions, the actual contact area is most often smaller than the apparent contact footprint, creating a localized high compressive stress at each asperity pair contact.

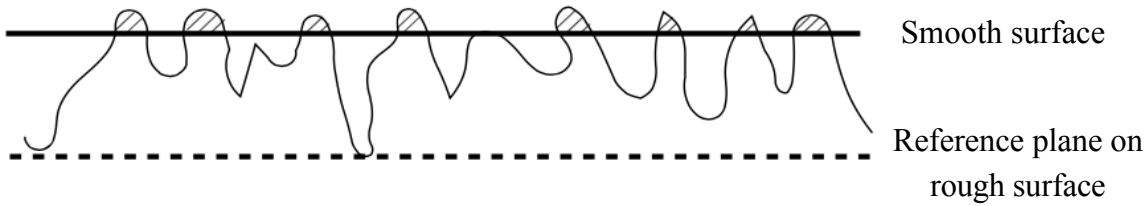


Figure 3.3: Contact of rough surfaces.

To include the surface roughness effect in predicting friction, the rough surface contact model by Greenwood and Tripp is adopted. The elemental contact load carried by the asperity,  $dW_a$  and the actual contact area,  $dA_a$  are defined as:

$$dW_a = dA_{app} \frac{8\sqrt{2}}{15} \pi (\zeta \beta \sigma)^2 \sqrt{\frac{\sigma}{\beta}} E^* f_{5/2}(\lambda) \quad (3.18)$$

$$dA_a = dA_{app} \pi^2 (\zeta \beta \sigma)^2 f_2(\lambda) \quad (3.19)$$

The surface asperity interaction properties based on the equations given above are shown to depend on the surface density of the asperity peaks,  $\zeta$ , the equivalent asperity curvature radius,  $\beta$  and the RMS surface roughness of the opposing surfaces,  $\sigma$ . The values for  $f_2$  and  $f_{5/2}$  are computed by Teodorescu *et al.* [93] and can be defined as:

$$f_2 = -\frac{18\lambda^5 - 281\lambda^4 + 1728\lambda^3 - 5258\lambda^2 + 8043\lambda - 5003}{10^4} \quad (3.20)$$

$$f_{5/2} = -\frac{46\lambda^5 + 574\lambda^4 - 2958\lambda^3 + 0.7844^2 - 1.0776\lambda + 0.6167}{10^4} \quad (3.21)$$

where  $\lambda$  refers to the separation parameter  $h_0/\sigma$ .

As the contact transits from HL to EHL and then ML and BL regimes, the lubricant film becomes thinner. Spikes [94] stressed on the importance of understanding the rheological properties of lubricants present in such thin films. Along the EHL regime, Habchi *et al.*[95] explained that shear thinning is going to give a significant impact towards friction prediction. Shearing of such thin films will no longer be Newtonian. To consider such properties, Larsson [96] included the effect of Eyring limiting shear stress to model the non-Newtonian shear of the lubrication film. The Newtonian and non-Newtonian behaviour of the lubricant can be separated by the Eyring limiting shear stress (see Figure 3.4).

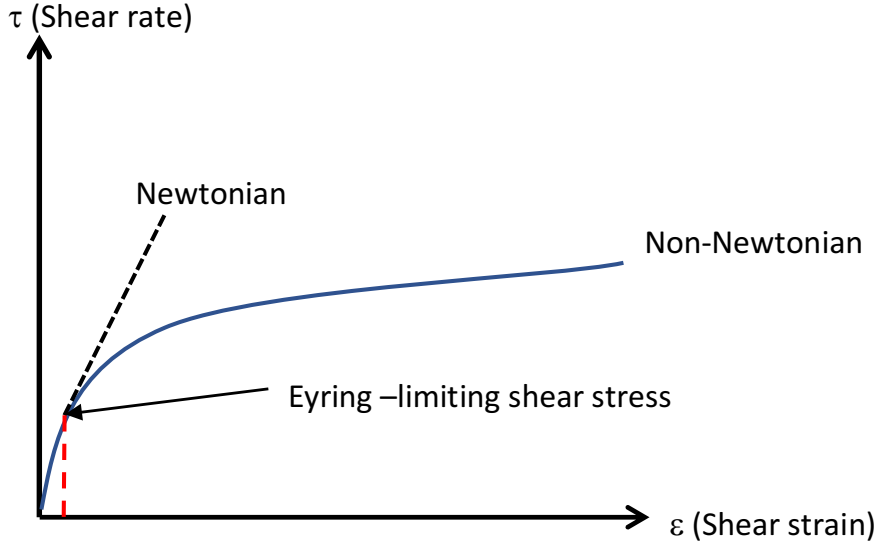


Figure 3.4: A non-Newtonian Shear-strain curve

Using this assumption along with the rough surface contact model, Teodorescu *et al.* introduced a set of mathematical equations to predict friction along a lubricated rough surface contact [93]. When the viscous shear stress,  $\tau$  ( $= \eta U/h$ ) is less than the Eyring limiting shear stress  $\tau_0$ , Newtonian viscous shear behaviour along a lubricated rough surface contact can be calculated as:

$$df_v = \tau(dA_{app} - dA_a) \quad (3.22)$$

Otherwise, when  $\tau$  is larger than or equal to  $\tau_0$ , the shear stress in the non-Newtonian condition is defined as [93]:

$$df_v = \tau_0 + \gamma p^* \quad (3.23)$$

where  $\gamma$  refers to the slope of the lubricant limiting shear stress pressure relation and  $p^*$  is the pressure exerted on the lubricant film and can be expressed as follow [93]:

$$p^* = \frac{dW - dW_a}{dA_a} \quad (3.24)$$

### 3.5 TaiCaan Laser Profilometer

To apply the rough surface contact model described above, the surface density of the asperity peaks,  $\zeta$ , the equivalent asperity curvature radius,  $\beta$  and the RMS surface roughness of the opposing surfaces,  $\sigma$  are measured using the TaiCaan Laser Profilometer. The laser profilometer is used to measure the surface topography for the test samples (pin and disc) before and after the test. The profilometer (see figure 3.5), measures the contact area, deformation and contact resistance in terms of the contact force and plane displacement, all whilst the surfaces are actually in contact [97].



Figure 3.5: Laser Profiler using TaiCaan<sup>TM</sup> machine

The test contact is mounted on a force sensor with an adjustable screw support, such that this sub-assembly can move into contact with the fixed transparent surface. The XYRIS 8600 CL (confocal laser), attached to the TaiCaan profilometer (see figure 3.6), is a compact, state of the art surface profiling system that is capable of measuring form and thickness of various surfaces. It incorporates a Charge Couple Devices (CCD) camera for on screen viewing of the surface under investigation, helping to identify areas or features of interest quickly and easily. Table 3.2 and 3.3 list the detail system specification and stage range on this state of art machine.

Table 3.2: Motion system specification

Travel	Resolution	Feedback	Bidirectional Repeatability	Max Speed
25mm	0.1 $\mu$ m 0.01 $\mu$ m	Linear encoder	0.2 $\mu$ m (over full 25mm range)	25mm/sec

Table 3.3: Motion stage range

Stages	Selection	Resolution	Travel	On axis accuracy	Maximum Speed
XYRIS 4000	Standard	0.1 $\mu$ m	25 mm x 25 mm	1.0 $\mu$ m	25 mm/s
	Option	0.6 nm			

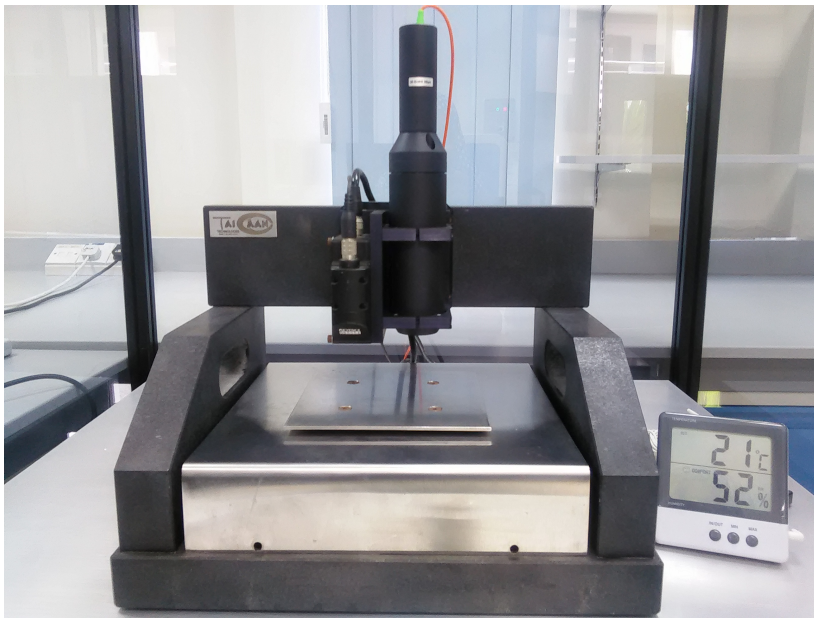


Figure 3.6: XYRIS 8600 CL

The profilometer has to be warmed up for 30 minutes before it can be used. The process is to allow the laser to drift to an equilibrium after startup. The sample is adjusted accordingly on the XY table of the profilometer. An oval coverage surface coupled with high resolution measurement is used for the measurements in this study. In this experiment, grid size is set in micron size of 0.3  $\mu$ m. This will ensure that the laser will focus on an exact area and shows the asperity peaks and valley as what being

discussed by Greenwood and Williamson theory. Once the measurement is done, the output data will be post-processed using BODDIES<sup>TM</sup>. This post processor can be used to conduct surface analysis. The surface analysis also generates the data required for the Green and Williamson model, such as peaks per unit area, mean peak height above a user selected level, individual peak heights, standard deviation of peak heights, radius of curvature for peaks. These data are to be used with the numerical simulation covered in this study.

### 3.6 Rheological properties for SAE grade lubricants

Along EHL and ML regime, lubricant viscosity-pressure influence is no longer negligible. For the current study, lubricant viscosity-pressure relation along the simulated tribological conjunction is taken into consideration based on the free-volume theory proposed by Wu *et al.* [98]. This method requires the lubricant viscosity-temperature relation as an input. In order to determine the lubricant viscosity-temperature relation, a Bohlin rotational Rheometer is used to characterise three commercially available SAE grade lubricants. The selected lubricants are SAE5W40, SAE10W40 and SAE15W40, each representing fully synthetic, semi-synthetic and mineral oil based lubricants, respectively. The lubricants are manufactured by Shell as shown in Appendix B. The experimental tests are carried out at a temperature range of 20°C to 100°C at 10/s shear rate and 1 Hz frequency. A Paltier cone plate with a dimension of 40 mm and 1° angle (CP 1°/40mm) was used to shear the samples. The cone plate was chosen because it minimises the turbulence during shearing of the lubricants. Figure 3.7 shows the schematic operation of rheological test conducted for this study.

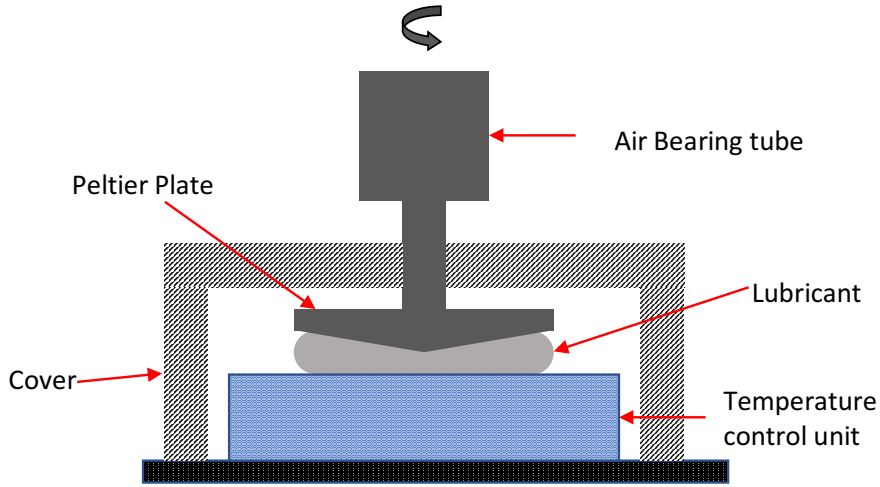


Figure 3.7: Schematic diagram for rheometer measurements

### 3.7 Results and discussion

This chapter focuses on determining the lubricant fluid film formation properties, such as contact pressure distribution and lubricant film thickness, for commercially available SAE grade lubricants. A two-dimensional Reynolds equation is solved iteratively for a lubricated point contact problem. In order to solve for the lubricated point contact problem, the selected SAE grade lubricant properties are first measured using a rheometer. Based on the method proposed by Wu *et al.* [98] in determining lubricant viscosity-pressure coefficient,  $\alpha$ , the lubricant viscosity-temperature relation of the lubricants are measured as given in Figure 3.8(a). This figure illustrates relationship between the dynamic viscosity of the selected lubricants with temperature. It is shown that, as temperature increased the lubricant viscosity decrease with mineral oil SAE15W40 dropped drastically. Meanwhile, for a fully synthetic oil, it is usually shows enhance resistance to deteriorate when exposed to temperatures changes[99].

For mineral oils and synthetic hydrocarbons, the lubricant viscosity-pressure coefficient,  $\alpha$  can be determined using [98]:

$$\alpha = (0.1593 + 0.2189 \log \eta_0) \times m' \quad (3.25)$$



where  $\log(\log(\eta_0 + 0.7)) = -m' \log T + N'$  with  $T$  referring to the lubricant temperature. The terms  $m'$  and  $N'$  are taken as the slope and the interception of the logarithmic linear relationship between lubricant dynamic viscosity and temperature. Figure 3.8(b) illustrates the change in lubricant viscosity-pressure coefficient,  $\alpha$  with temperature. Using the measured lubricant viscosity-pressure coefficient,  $\alpha$  at a given lubricant operating temperature, the fluid film formation characteristics of the simulated point contact can be computed iteratively by solving for the Reynolds equation as discussed above.

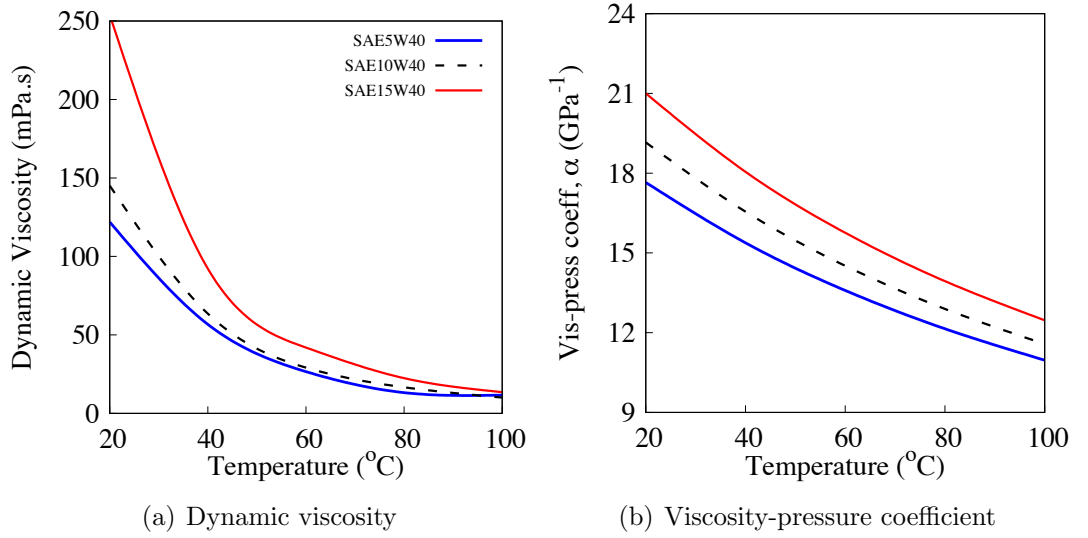


Figure 3.8: Experimentally measured on rheological properties at different temperatures for commercially available engine lubricants

Table 3.4: Simulated Rheological properties for commercially available SAE grade lubricants

Parameter	SAE5W40	SAE10W40	SAE15W40	units
Bulk viscosity, $\eta_0$	0.068	0.098	0.1639	mPa
Bulk density, $\rho_0$	842.1	858.9	878.7	kg/m <sup>3</sup>
Lubricant pressure viscosity index, $z$	0.4526	0.4812	0.492	-

The lubricant operating temperature is taken to be 35°C for this specific study. Table 3.4 summarise the lubricant properties for the simulated SAE grade lubricants. It is to note that lubricant pressure viscosity index,  $z$  is determined from the measured lubricant viscosity-pressure coefficient,  $\alpha$  at 35°C. Before proceeding to simulate the lubricated point contact problem, the expected operating lubrication regime for the selected SAE grade lubricants based on the selected lubrication regimes are predicted using the Greenwood chart. In the chart,  $g_E$  is equal to  $W^{*8/3}/U^{*2}$  and the term  $g_V$  is equal to  $G^*W^{*3}/U^{*2}$ . The terms  $G^*$  ( $= E/\alpha_0$ ),  $W^*$  ( $= W/ER_xL$ ) and  $U^*$  ( $= u\eta_0/ER_x$ ) are non dimensional terms for modulus Young of the contact materials, applied normal load and sliding velocity, respectively. Figure 3.9 illustrates the lubrication regime mapping for the selected SAE grade lubricants under the simulated operating conditions for a velocity range of 0.125 m/s to 4.0 m/s. It is shown that the simulated operating conditions for all the selected SAE grade lubricants fall in the visco-elastic regime, indicating hard EHL properties.

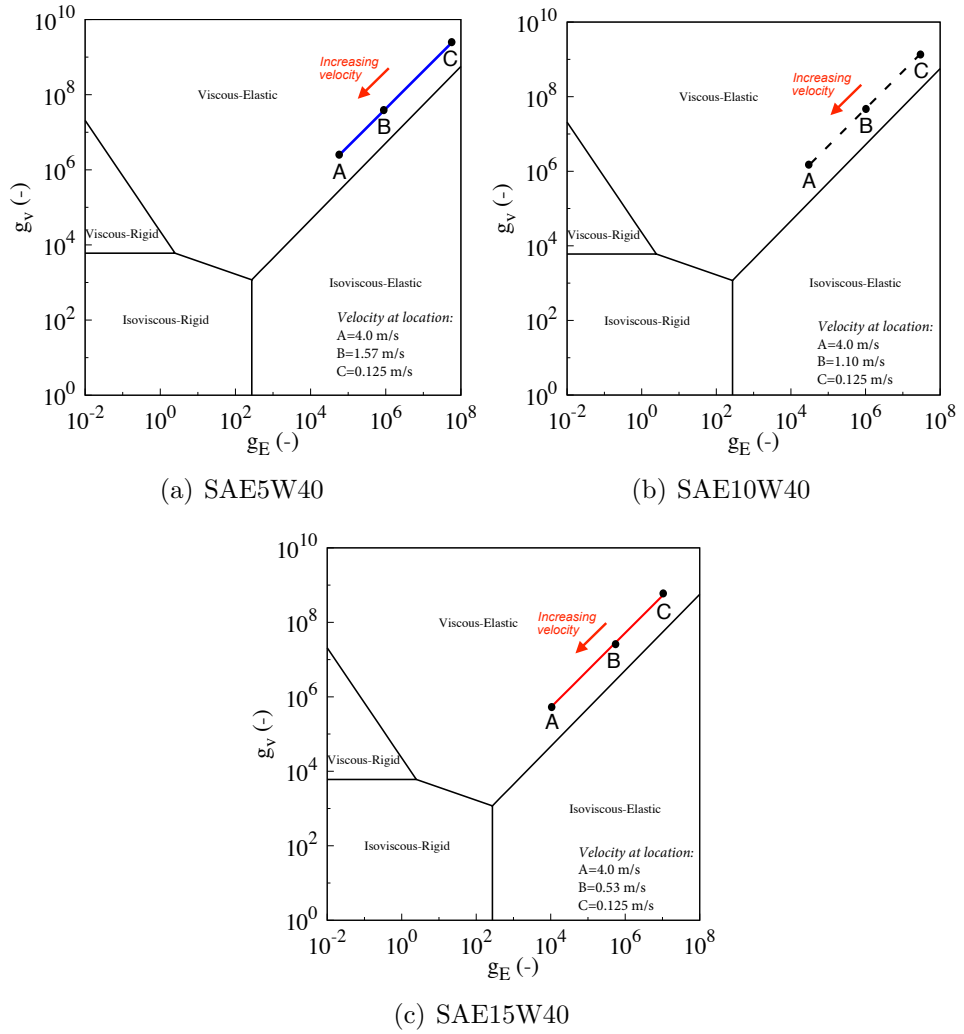


Figure 3.9: Lubrication regime mapping for simulated SAE grade lubricants based on simulated conditions

Using the numerical algorithm proposed for Reynolds equation together with the measured lubricant properties for SAE5W40, SAE10W40 and SAE15W40, Figure 3.10 shows the contact pressure distribution and lubricant film profile at sliding velocity of 4.0 m/s. At such sliding velocity, it can be seen that the contact pressure is in the range of GPa and also exhibits a secondary peak. Besides this, a horse-shoe lubricant film constriction can also be observed towards the trailing edge of the point contact, as depicted in Figure 3.10(b). The simulated fluid film properties correlate well with the mapped lubrication regime given in Figure 3.9, indicating viscous-elastic lubrication.

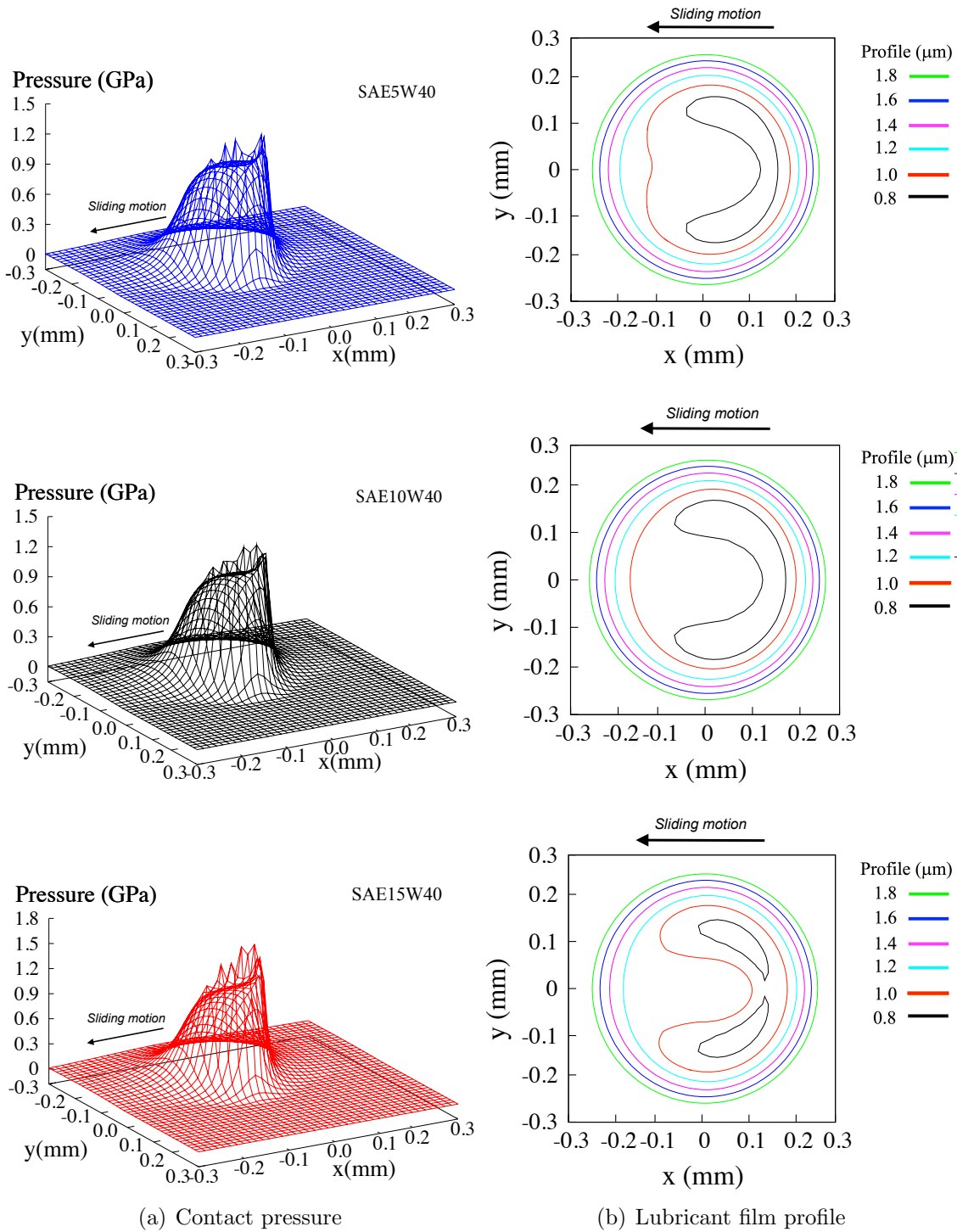


Figure 3.10: Contact pressure distribution and lubricant film profile for simulated point contact lubricated with selected SAE grade lubricants at sliding velocity of 4 m/s

The Reynolds solution is then applied to further solve for the point contact lubricated for the selected SAE grade lubricants at various sliding velocities as shown in Figure 3.11, 3.12 and 3.13. These figures show the central section of the contact pressure and lubricant film profile along x-axis and y-axis. As the sliding velocity decreases (from location A to location C as shown in Figure 3.9), the secondary peak of the contact pressure diminishes along the x-direction (where sliding occurs), eventually resembling a Hertzian like characteristic. These localised behaviours are demonstrated by all *three* simulated lubricants. It is to note that as pure sliding is only allowed along the x-direction. Therefore, the pressure distributions along y-axis are expected to be symmetrical as shown in the figures below.

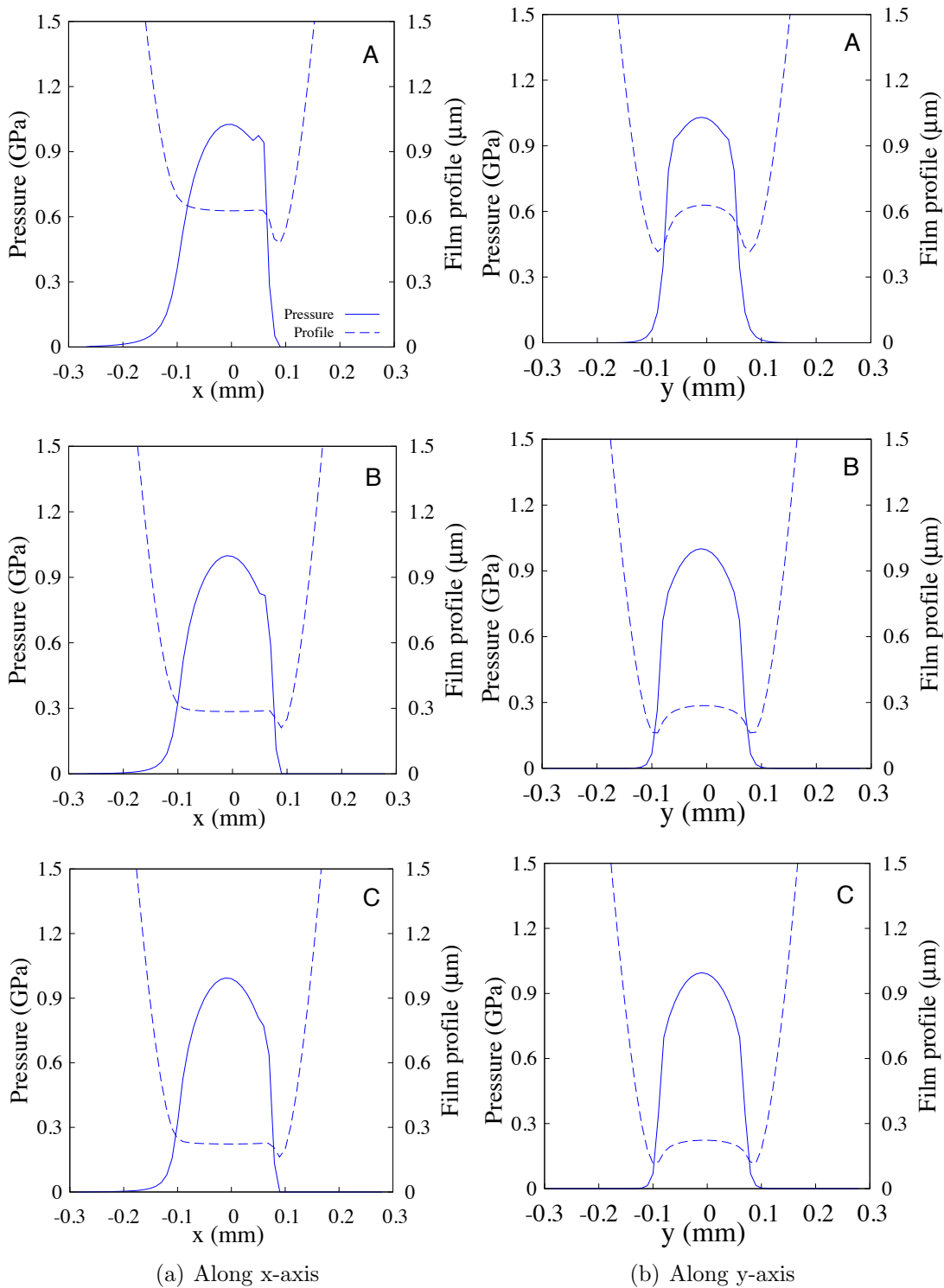


Figure 3.11: Contact pressure distribution and lubricant film profile for point contact lubricated with SAE5W40 grade engine lubricant

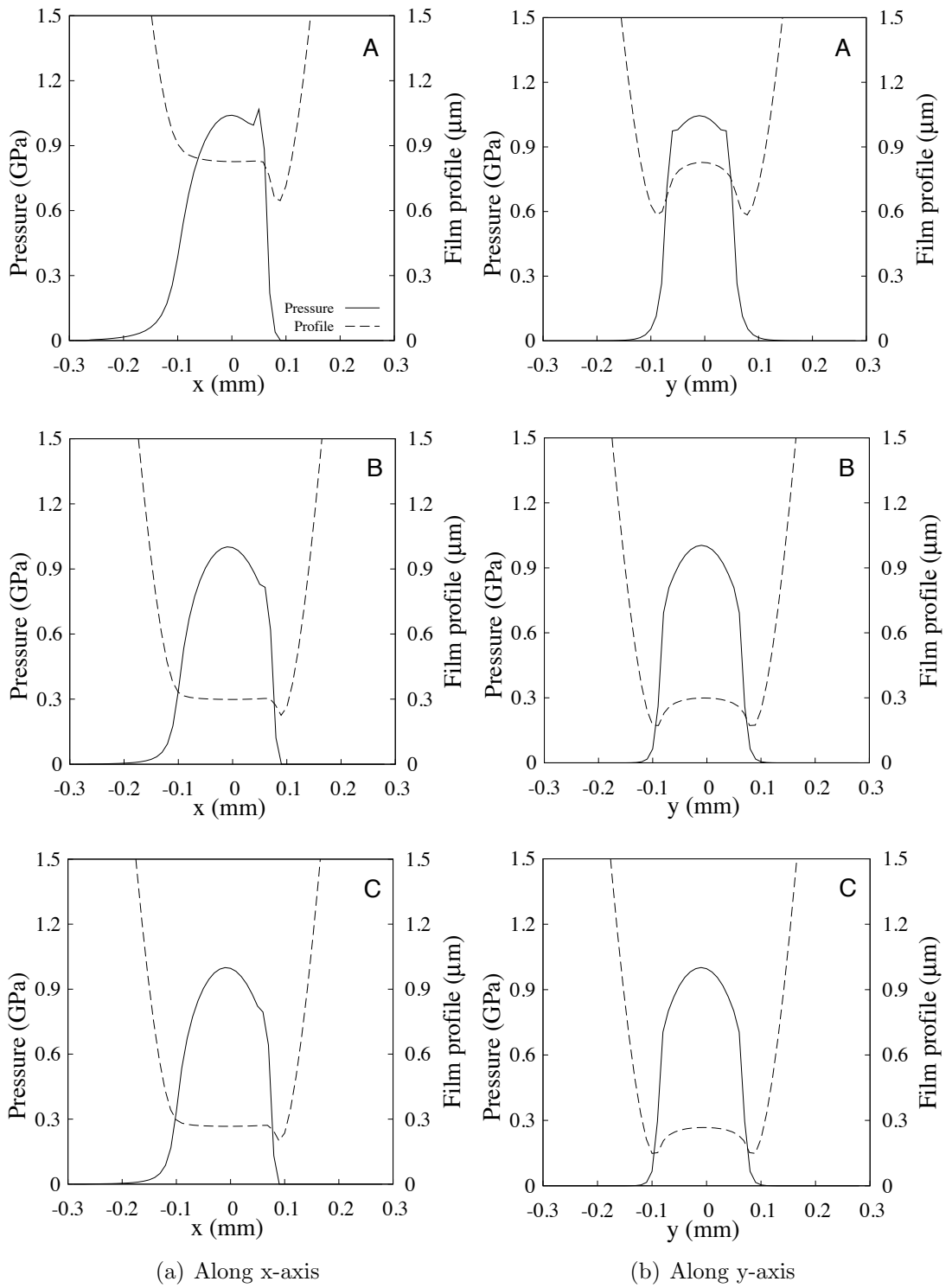


Figure 3.12: Contact pressure distribution and lubricant film profile for point contact lubricated with SAE10W40 grade engine lubricant

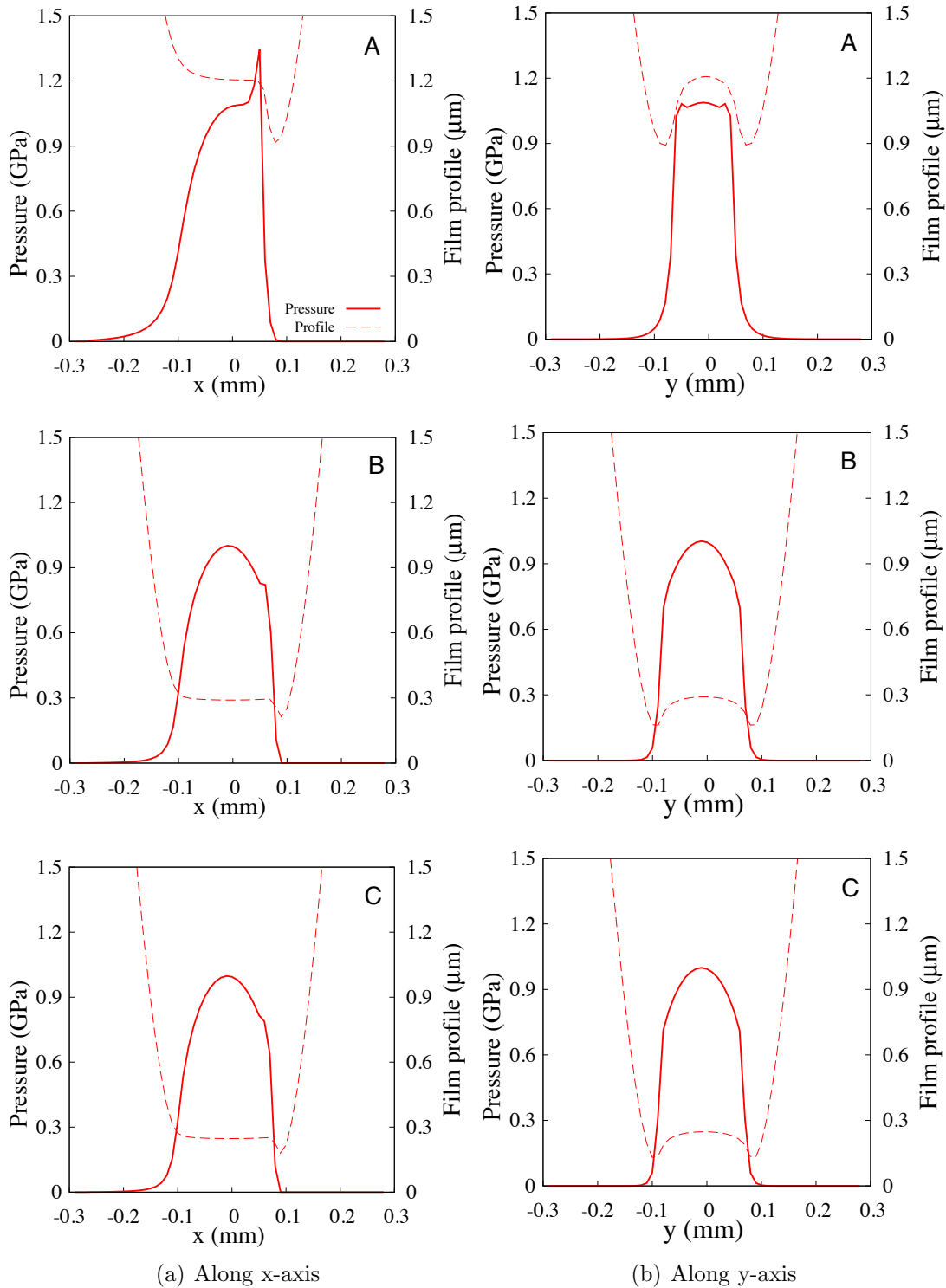


Figure 3.13: Contact pressure distribution and lubricant film profile for point contact lubricated with SAE15W40 grade engine lubricant



The lubricant film thickness along the pressurized region of the contact is also shown to be at sub-micron level. This is in similar order of magnitude as the measured composite surface roughness for the investigated contact ( $\approx 0.105 \mu\text{m}$ ), indicating possible surface asperity interactions that could significantly increase the friction generated along the opposing surfaces. For each lubricants, the central part of the contact have an almost uniform thickness. Together with the diminishing of pressure peak on the contact pressure distribution plots, the contact profile is deformed, forming a dimple close to the trailing edge, indicating visco-elastic lubrication properties.

As mentioned earlier, a lubricated point contact under pure sliding motion is simulated. Reynolds equation is used to determine the fluid film formation properties, such as contact pressure distribution and lubricant film profile along a point contact. The contact geometry for the Reynolds solution is taken to be perfectly smooth. Using the contact pressure and lubricant film profile determined from the Reynolds solution, the rough surface contact model as described above is then superimposed on the perfectly smooth contact geometry to compute the frictional properties of the simulated point contact, lubricated with commercially available SAE grade lubricants.

Table 3.5: Measured value of a rough surface contact parameters using Taicaan laser profilometer

<b>Parameter</b>	<b>Values</b>	<b>Units</b>
RMS surface roughness, $\sigma$	0.13	$\mu\text{m}$
Product of $\zeta\beta\gamma$	0.40	-
Ratio of $\sigma/\beta$	0.01	-
Pressure coefficient, $\kappa$	0.20	-

In order to understand the behaviour of the proposed friction model, a parametric study is conducted in this chapter. This is done to determine the sensitivity of the parameters from the rough surface contact model in predicting friction. At sliding velocity of 4.0 m/s (location A) for SAE 10W40 grade lubricant, Figure 3.14 shows a significant change in viscous shear based on the following assumptions used to compute friction along the sliding contact. The first assumption takes only bulk viscosity to calculate the viscous shear (see Figure 3.14(a)). This is followed by the second assumption where viscosity-pressure  $\eta(p)$  influence is taken into account as shown in

Figure 3.14(b). Both these assumptions consider Newtonian behaviour of the lubricant. When thin film is being sheared at high velocity, the liquid could transit from Newtonian to non-Newtonian behaviour [100]. The non-Newtonian behaviour will reduce the viscous shear (see Figure 3.14(c)) due to the Eyring limiting shear stress of the lubricant, also known as the maximum allowable shear stress (see Figure 3.4) in an EHL contact [100]. Beyond this limiting Eyring stress value, the shear stress will saturate.

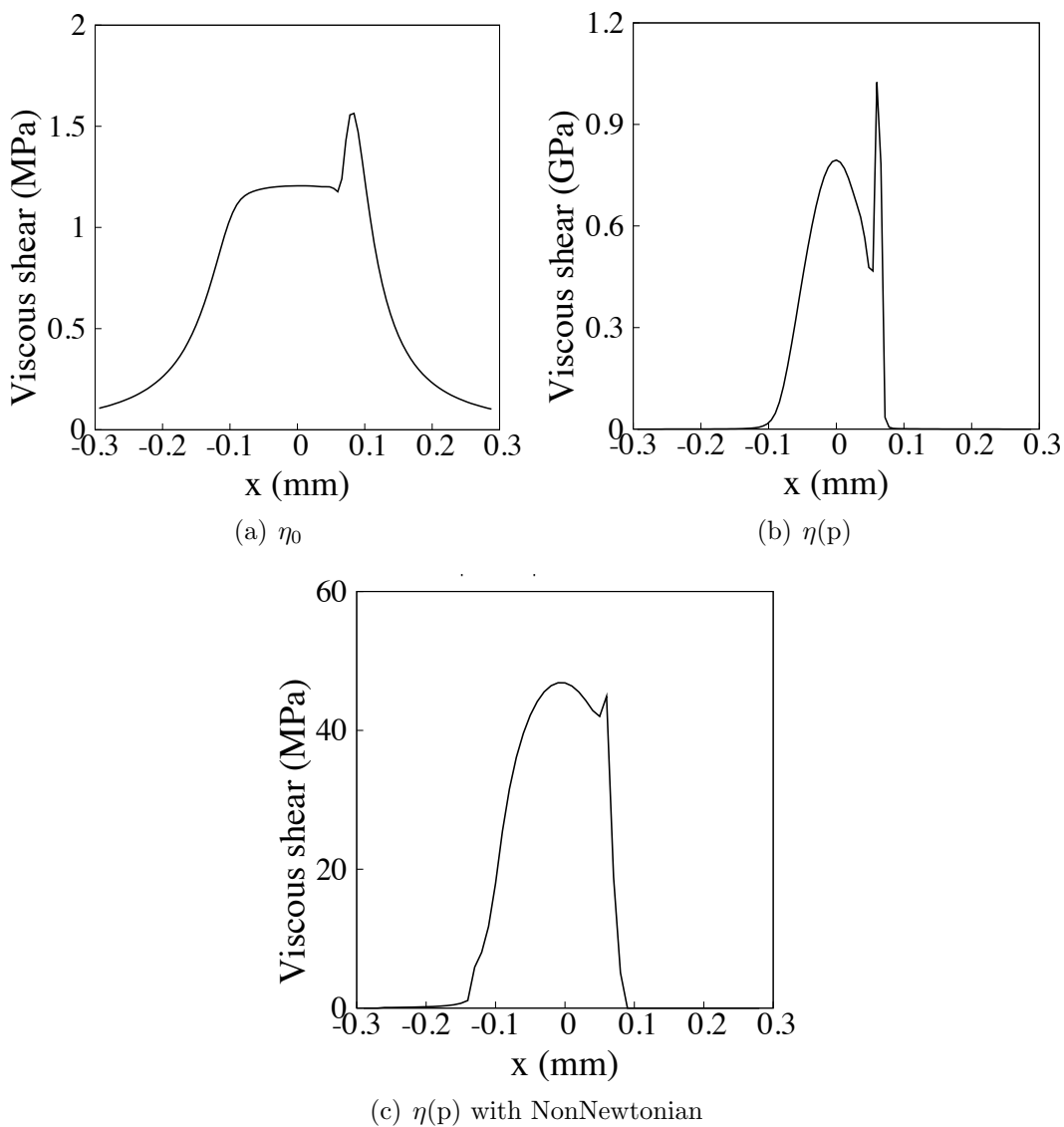


Figure 3.14: Viscous shear calculated using various formulation

The next step is to check the sensitivity of the non-Newtonian assumption. Applying different  $\tau_0$  and  $\gamma$  values, the non-Newtonian viscous shear is calculated for the lubricant as given in Table 3.6 and 3.7. It can be observed that, the effect of  $\tau_0$  is minimal when increased from 1 MPa to 4 MPa as observed in Figure 3.15. On the other hand,  $\gamma$  seems to give a significant effect on the viscous shear (see Figure 3.16). This shows that when pressure reaches 1 GPa, the pressure dependent  $\gamma$  has now become a dominant factor in affecting boundary shear of the lubricant [100].

Table 3.6: Friction value with constant  $\gamma = 0.08$

$\tau_0$	Viscous friction (N)
1 MPa	1.5741
2 MPa	1.5834
4 MPa	1.6122

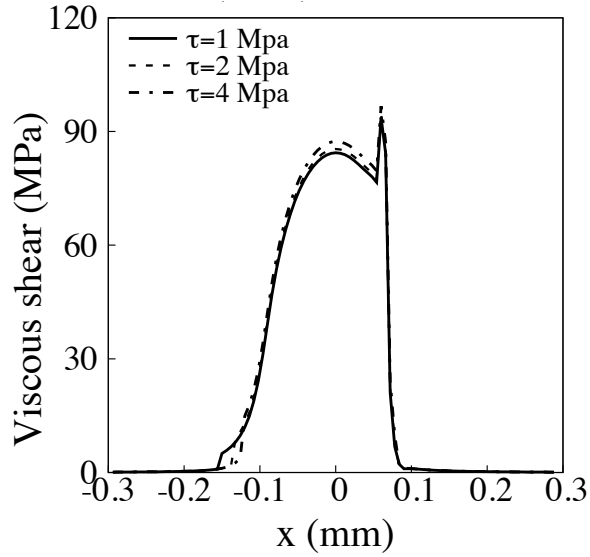


Figure 3.15: Viscous shear with  $\gamma = 0.08$  MPa

Table 3.7: Friction value with constant  $\tau_0 = 2$  MPa

$\gamma$	Viscous friction (N)
0.05	1.0312
0.08	1.5834
0.1	1.9516

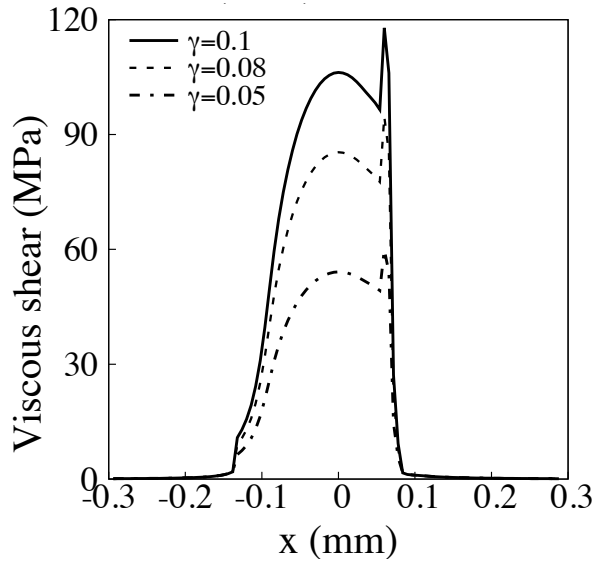


Figure 3.16: Viscous shear with  $\tau_0 = 2$  MPa

### 3.8 Summary

This chapter discussed on the lubricant fluid film formation properties for a point contact lubricated with commercially available SAE grade lubricants predicted using the develop numerical solution for Reynolds equation. The lubricant viscosity-pressure coefficient is determined using a free-volume theory, requiring the lubricant-temperature relation as input. Using the measured lubricant properties, the numerical method proposed in the previous chapter is adapted to solve for a lubricated point contact problem. The simulated lubricant fluid film formation properties are compared to the lubrication regime properties given by Greenwood chart. It is shown that the proposed numerical model is capable of simulating lubrication properties, corresponding to the visco-elastic lubrication properties as indicated in the Greenwood chart based on the simulated operating conditions. The next chapter will look at using the simulated lubricant fluid film formation properties computed in this chapter to predict frictional characteristics for the selected SAE grade lubricants using a rough surface contact model.

This chapter also describes the application of a rough surface contact model based on Greenwood and Tripp's approach in determining the frictional characteristics of a lubricated point contact, where the fluid film formation properties are determined using

the Reynolds solution discussed in the previous chapter. The rough surface contact model, using the contact pressure distribution and lubricant film profile predicted using the Reynolds solution, is shown to be capable of predicting viscous and boundary shear properties along the simulated tribological conjunction. The model also shows that the simulated point contact transits from fluid film lubrication to ML and BL regimes. In the next chapter, a set of friction tests are to be conducted in order to validate the mathematical model in predicting frictional properties of commercially available SAE grade lubricants.

# Chapter 4

## Friction Measurements

### 4.1 Introduction

This chapter focuses on measuring friction forces of lubricated sliding contacts in order to validate the mathematical model derived in the previous chapter, which has thus far been demonstrated to be capable of predicting fluid film formation (Reynolds solution) and frictional properties (rough surface contact) of lubricated point contact. Studies of lubrication can be validated using several types of friction testers or tribometers. The tribometer is useful for surface engineering and lubrication studies. It is mainly used to understand engineering surfaces in relative motion.

### 4.2 Friction testing using pin-on-disc tribometer

In this chapter, friction tests are carried out for the selected SAE grade lubricants to characterise their frictional properties under pure sliding motion at different lubrication regimes. The test is performed using a tribometer configured for a pin-on-disc setup (see Figure 4.1). The selection of a pin-on-disc configuration is to validate the simulated point contact lubricated with the tested SAE grade lubricants under pure sliding motion. Table 5.1 shows basic specification of a typical Pin-on-disc tribometer.

Table 4.1: Technical specification of a typical Pin-on-disc tribometer machine

Parameter	Specifications
Load Range	0.5 kg to 20 kg
Rotational Speed	100 to 2000 rpm
Frictional Force Measurement	0 to 200 N

In this study, a wear disc, fabricated from JIS SKD-11 tool steel (75 mm diameter and 4 mm thickness) is rotated against a stationary cast iron pin (10 mm diameter and 32 mm length). The cast iron pin has a spherical end cap with curvature radius of 5 mm. Both the pin and the wear disc are ground to give a composite RMS surface roughness,  $\sigma$  of  $0.13 \mu\text{m}$ . Before running the friction test, the pin and the wear disc are cleaned using an ultrasonic bath and then left to dry in a desiccator. This is to remove the residuals of tooling fluids from the machining process.

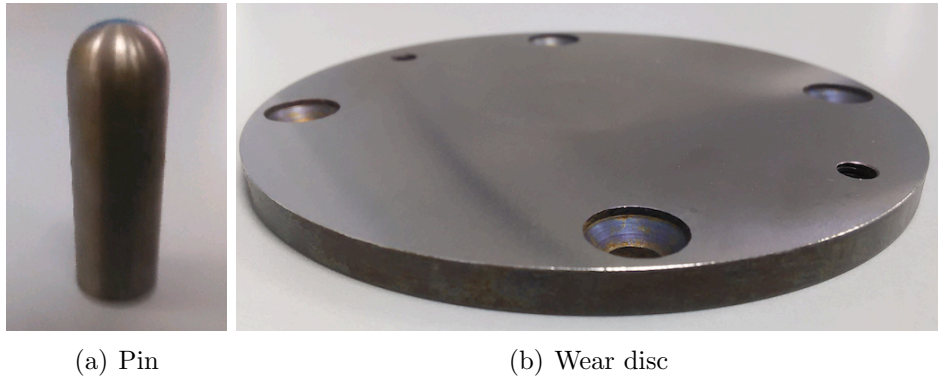


Figure 4.1: Pin (cast iron) and wear disc

The Ultrasonics bath (see Figure 4.2) is used to clean the samples before the friction test. This machine is set for 10 minutes at  $45^{\circ}\text{C}$ . As soon as the time ends, the samples have to be wiped and cleaned before being kept in a desiccator. Considering the material gets rusty easily, precaution must be taken during handling of the material.



Figure 4.2: Ultrasonic bath -SONICA

The experimental set-up for the friction test is shown in Figure 4.3. The schematic diagram in Figure 4.4(a) illustrates the friction test set-up, where a pin slides on a rotating horizontal wear disc. Figure 4.4(b) shows the loading mechanism for the pin-on-disc tribotester. Using this method, the wear disc is to be fixed on a rotating table, having a long vertical shaft clamped with screw from the bottom surface of the rotating plate.

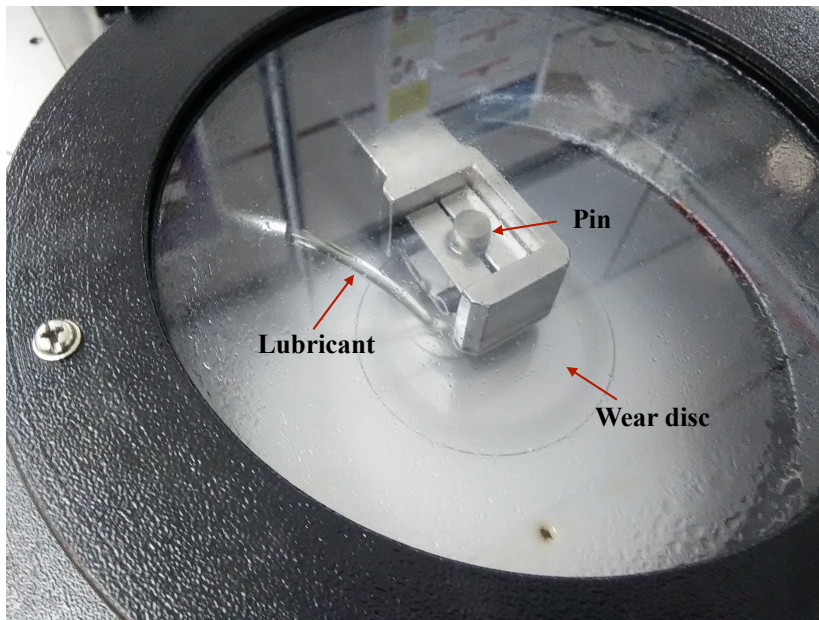


Figure 4.3: Experimental setup on pin-on-disc tribometer machine



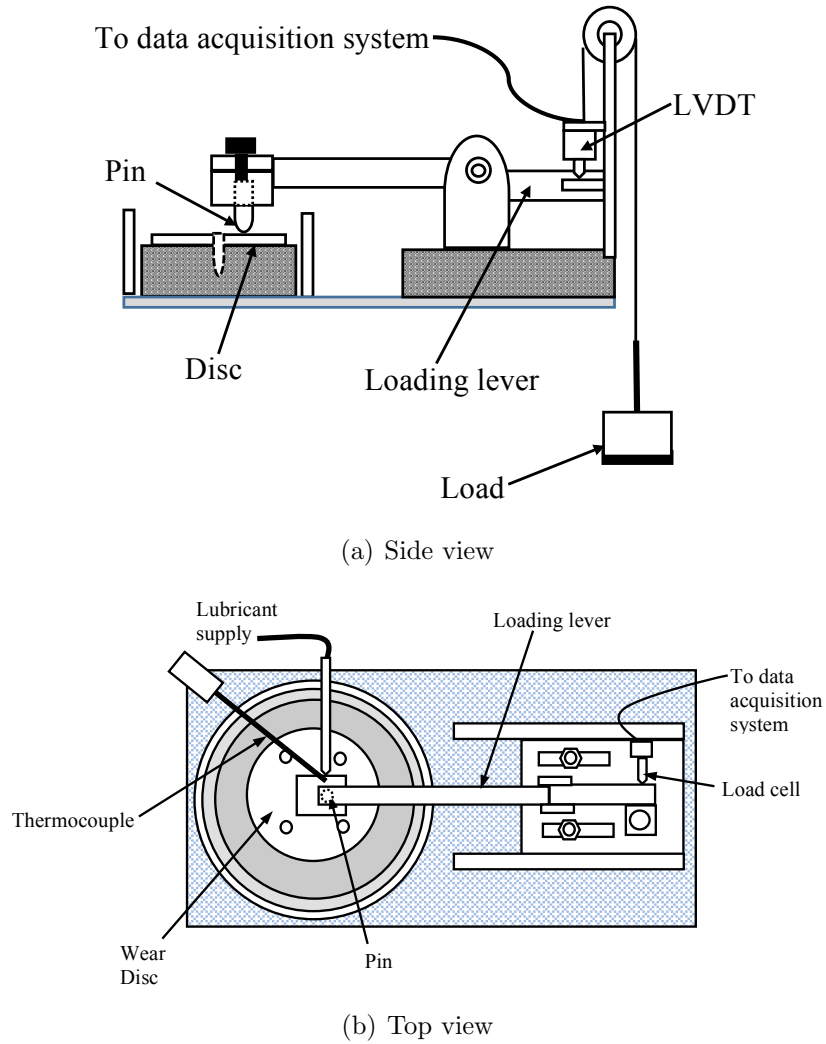


Figure 4.4: Schematic views of pin-on-disc tribometer

The friction tests are conducted under room temperature condition. During the test, the pin and wear disc are subjected to a constant normal load of 2 kg with wear disc rotational speed ranging from 100 rpm to 2000 rpm. The wear track is set at 20 mm, corresponding to wear disc linear sliding velocity between 0.125 m/s and 4.0 m/s. For the selected test conditions, the maximum Hertzian pressure for the contact is 0.96 GPa, calculated by taking the modulus of elasticity for cast iron and JIS SKD-11 tool steel as 110 GPa and 210 GPa with Poisson's ratio of 0.21 and 0.27, respectively. A lubricated run-in test is conducted for each lubricant with 2 kg normal loading in order

to flatten the initial high surface asperity peaks separated by deep valleys.

Adapting the approach by Kovalchenko et al. [101], the friction test starts at a wear disc rotational speed of 2000 rpm and decreased in a stepwise manner after three minutes of each speed until the minimum speed of 20 rpm is achieved. This procedure allows for the contact to move from fluid film lubrication to ML and then finally to BL regime. The amount for each lubricant engine oil prepared for the friction test around 1.0 liter. For the whole test duration, the tested lubricant is continuously supplied to the pin-disk contact/wear track through a pump to ensure a fully flooded lubricated conjunction. This is to reduce any possible chances of having lubricant starvation that might cause a higher friction due to the lack of lubricant entrainment at higher rotational speeds.

### 4.3 Friction measurements for SAE grade lubricants

In this study, the frictional characteristics of commercially available SAE grade lubricants, namely, SAE5W40, SAE10W40 and SAE15W40 are measured under pure sliding motion using a pin-on-disc tribometer. The measured frictional characteristics for these lubricants are then used to validate the simulated friction forces for a point contact based on the mathematical model described in the previous chapter.

The friction forces measured using the pin-on-disc tribometer at different sliding velocities for SAE5W40, SAE10W40 and SAE15W40 lubricants are shown in Figure 4.5. The repetitiveness test of friction force for the selected lubricant show that the maximum standard deviation for SAE5W40 is only 0.016N, while for SAE10W40 is 0.015N and finally for SAE15W40 represent only 0.035N among the tested sets of data. At low sliding velocities, the measured friction force values remain fairly constant for the lubricants, indicating boundary lubrication (BL) regime. Along this lubrication regime, load carrying capacity and frictional properties are dominated by surface asperity interactions, separated only by ultra-thin boundary adsorbed lubrication film. This thin film remains as the last barrier in preventing direct metal-to-metal contact. With increasing sliding velocity, the friction forces then drop into the ML regime, where the combination of surface asperity interactions and fluid film shearing become the underlying mechanism for friction contact.

The transitions from BL to ML regime for SAE5W40, SAE10W40 and SAE15W40

occur at 0.89 m/s, 0.25 m/s and  $\leq 0.125$  m/s respectively. Further increment in sliding velocity encourages lubricant entrainment into the contact, which increases the separation gap between opposing sliding surfaces. This eventually leads to a significantly reduced surface asperity interaction where fluid film lubrication will prevail. This can be seen to occur for all types of lubricant tested, SAE5W40, SAE10W40 and SAE15W40 at 1.12 m/s, 0.8 and 0.53 m/s, accordingly. The change in friction force values observed with increasing sliding velocities implies the characteristics of a lubrication Stribeck curve, showing the transition from BL to ML and finally to HL regime.

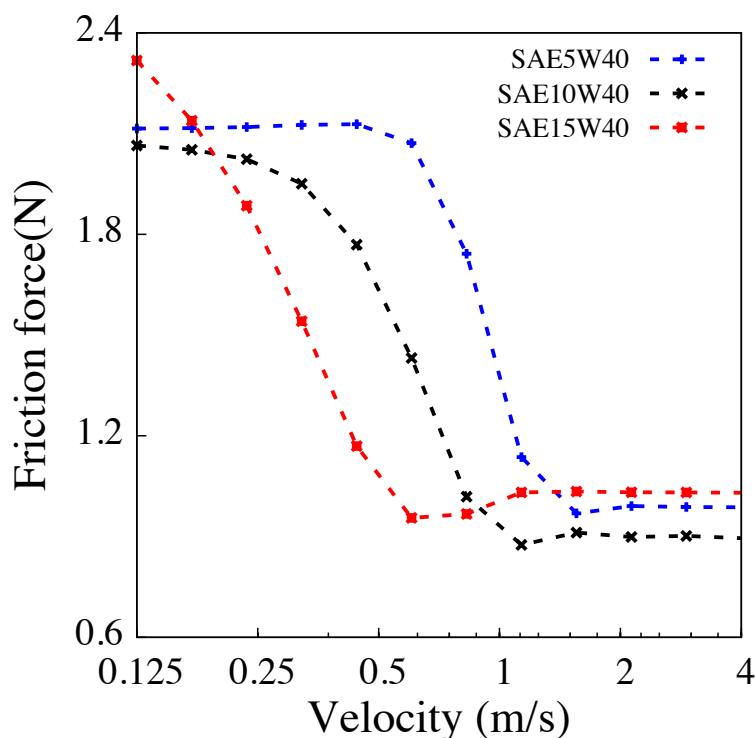


Figure 4.5: Stribeck curve of selected engine lubricant on pin-on-disc tribometer machine

#### 4.3.1 Correlating friction measurements *for SAE grade lubricants* with simulation

It is to note that the parameters required for the friction prediction model, namely the pressure coefficient,  $\kappa$  and the slope of lubricant limiting shear stress pressure relation,

$\gamma$  are not readily available. Also, it is realised that these parameters affect the magnitude of either BL and EHL friction forces. It is to note that adjusting the  $\kappa$  term affects the magnitude of the boundary friction. Based on the specifications provided by the lubricant manufacturer, all of the selected SAE grade engine lubricants consists of extreme-pressure additives in the form of zinc dialkyldithiophosphate (ZDDP), which forms an effective tribofilm to reduce wear. With rubbing between the surfaces happening under contact pressure in the range of GPa (computed using the derived mathematical tool), it is expected that such tribofilm to be formed between the opposing surfaces. Therefore, it is assumed that the pressure coefficient,  $\kappa$  is as a result of shearing the boundary film formed by ZDDP. The value for this term is measured using the Lateral Force Microscopy (LFM-Park XE7 from Park System ) [102] method as shown in Figure 4.6.

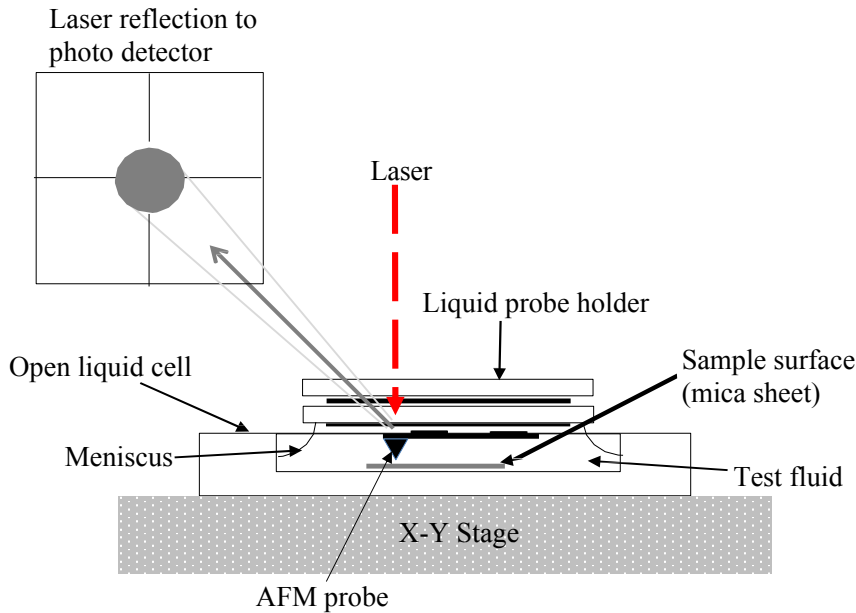


Figure 4.6: Lateral Force Microscopy (LFM) setup

The measurements from LFM are in voltage signal. Hence, a simplistic calibration method proposed by Buenviaje et al. [103] is used to convert the electrical signal to physical friction values. Adopting the method, known as the 'Blind' calibration approach, a lumped calibration factor, is tested on a silicon calibration sample, is calculated using:

$$\alpha = \frac{F_f(v)/F_n(nN)}{0.19} \quad (4.1)$$

where the denominator is the coefficient of friction for a silicon calibration sample. The AFM probe that has been used refers to PPP-Contscr model from Park System. This model is a contact type cantilever with backside reflects coating and it is used in the application for lateral or friction force mode [104].

The values for corresponding to the applied normal loads are then subsequently used to convert the friction trace-retrace signal in voltage to physical friction value based on the following equation:

$$F_n(nN) = \frac{F_f(v)}{\alpha(V/nN)} \quad (4.2)$$

The friction force against applied normal load measured using LFM for an AFM tip sliding on the wear disc lubricated by ZDDP is as given in Figure 4.7. The term  $\zeta$  is assumed to be equivalent to the slope of the measured friction values, which is approximated to be 0.324. The linear curve fitting of the measured friction force using (LFM) gives an R-squared value of 0.9904.

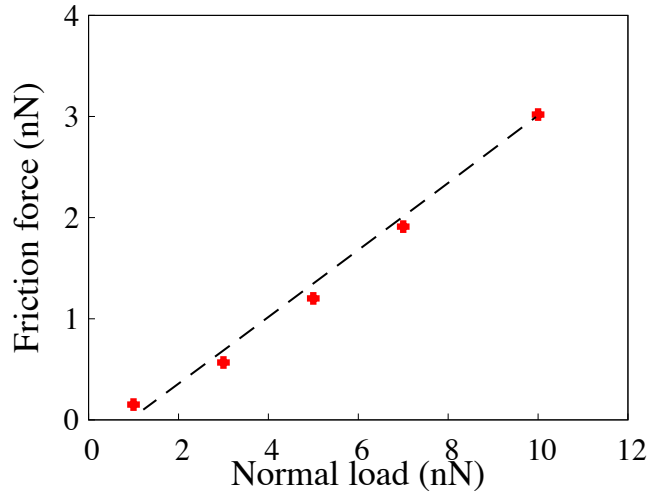


Figure 4.7: Measured friction force for wear disc surface lubricated with ZDDP using Lateral Force Microscopy

In order to correlate the simulation data to the experimental data, the slope of

lubricant limiting shear stress pressure relation,  $\gamma$  is also crucial. This term affects the magnitude of friction along fluid film lubrication regime, especially EHL and ML regimes where non-Newtonian behaviour of the lubricants might prevail. Typically, this value can be measured using an MTM. However, as this equipment is not available for the current study, it is decided that the value of  $\gamma$  is obtained by fitting the simulation data to the measured parameters. This is similar to the approach adopted by Evans and Johnson [105], where they used a disc machine traction test to determine the rheological properties of lubricants under EHL. Hence, Table 4.2 summarises the  $\gamma$  values for each SAE grade lubricants, adjusted accordingly in order to ensure good correlation between simulation and experimental data. It is to note that the values obtained are within the range measured for typical mineral oil based lubricants as reported by Morgado et al. [88].

Table 4.2: Parametric values of simulated lubricant study for SAE grade lubricant

Type of lubricant	Lubricant limiting shear stress pressure relation, $\gamma$
SAE5W40	0.0505
SAE10W40	0.0440
SAE15W40	0.0505

In this study, the surface roughness properties of the surfaces in contact are assumed to be consistent for all test samples. Therefore, by simulating across the sliding velocity range of the measured lubricant Stribeck curve, Figure 4.8 illustrates the predicted Stribeck curve for the point contact lubricated by the commercially available SAE grade lubricants. The simulated Stribeck curves shown in Figure 4.8 are found to correlate well with the measured coefficient of friction values. This indicates that the mathematical model used in the current analysis is capable of capturing the lubrication regime transition from EHL to ML and then finally to BL regime. From the same figure, the viscous friction component is shown to diminish with slower sliding velocity. The reducing viscous friction indicates a smaller lubricant film thickness, leading to increased surface asperity interaction. As a result of this, boundary friction began to increase, giving rise to ML regime. At even slower sliding velocity, the lubricated point contact eventually reaches BL regime, where friction is now dominated by the

boundary friction component.

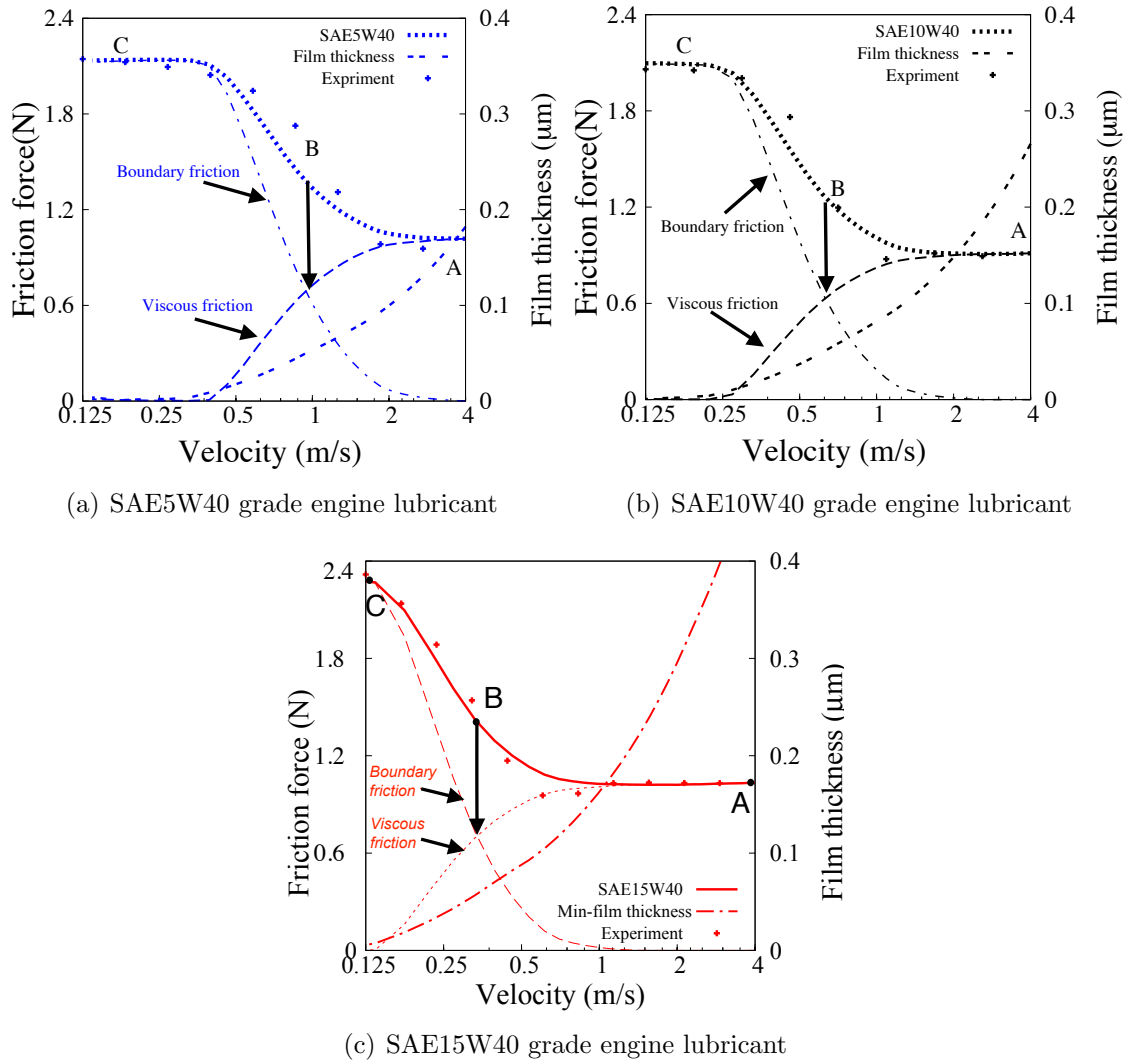


Figure 4.8: Simulated lubricant Stribeck curve for selected commercially available engine lubricant

Figures 4.9 to 4.11 illustrate the viscous and boundary shear components along the simulated point contact, lubricated with SAE5W40, SAE10W40 and SAE15W40 engine lubricant at different sliding velocities. For the simulated point contact lubricated with SAE5W40, it is shown that at location A, only viscous shear component exists. This means that no boundary interaction occurs along the lubricated contact. However, when the sliding velocity is decreased (at location B), it can be observed that boundary shear component now exists along with viscous shear. Decrease in sliding velocity (at location C) further increases the contribution from the boundary shear component as a result of smaller separation along opposing surfaces, exhibiting the characteristic of boundary lubrication regime. Similar trend is also observed for the simulated point contact lubricated by SAE10W40 (see Figure 4.10) and SAE15W40 (see Figure 4.11).



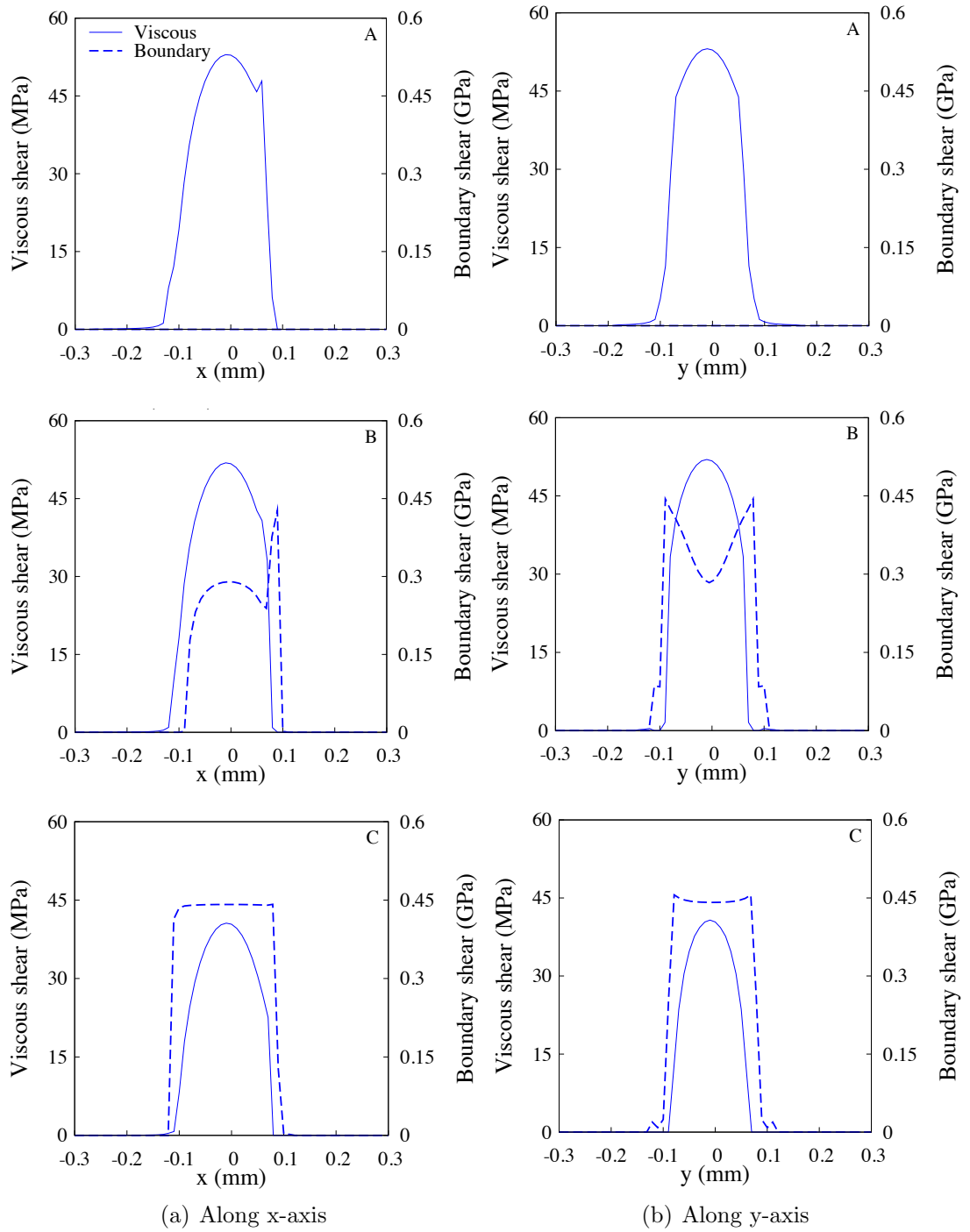


Figure 4.9: Viscous and boundary shear properties for point contact lubricated with SAE5W40 grade engine lubricant.

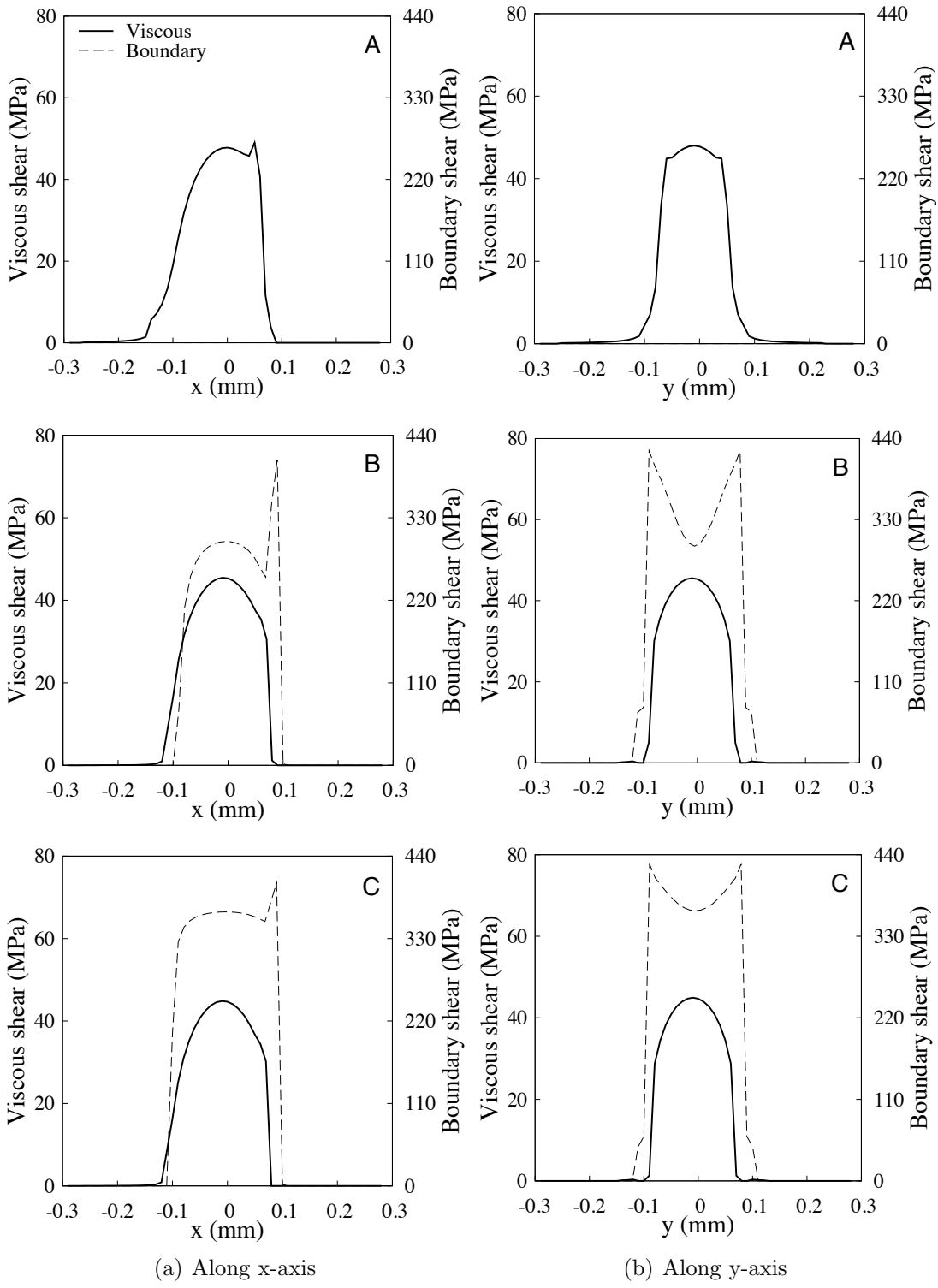


Figure 4.10: Viscous and boundary shear properties for point contact lubricated with SAE10W40 grade engine lubricant.

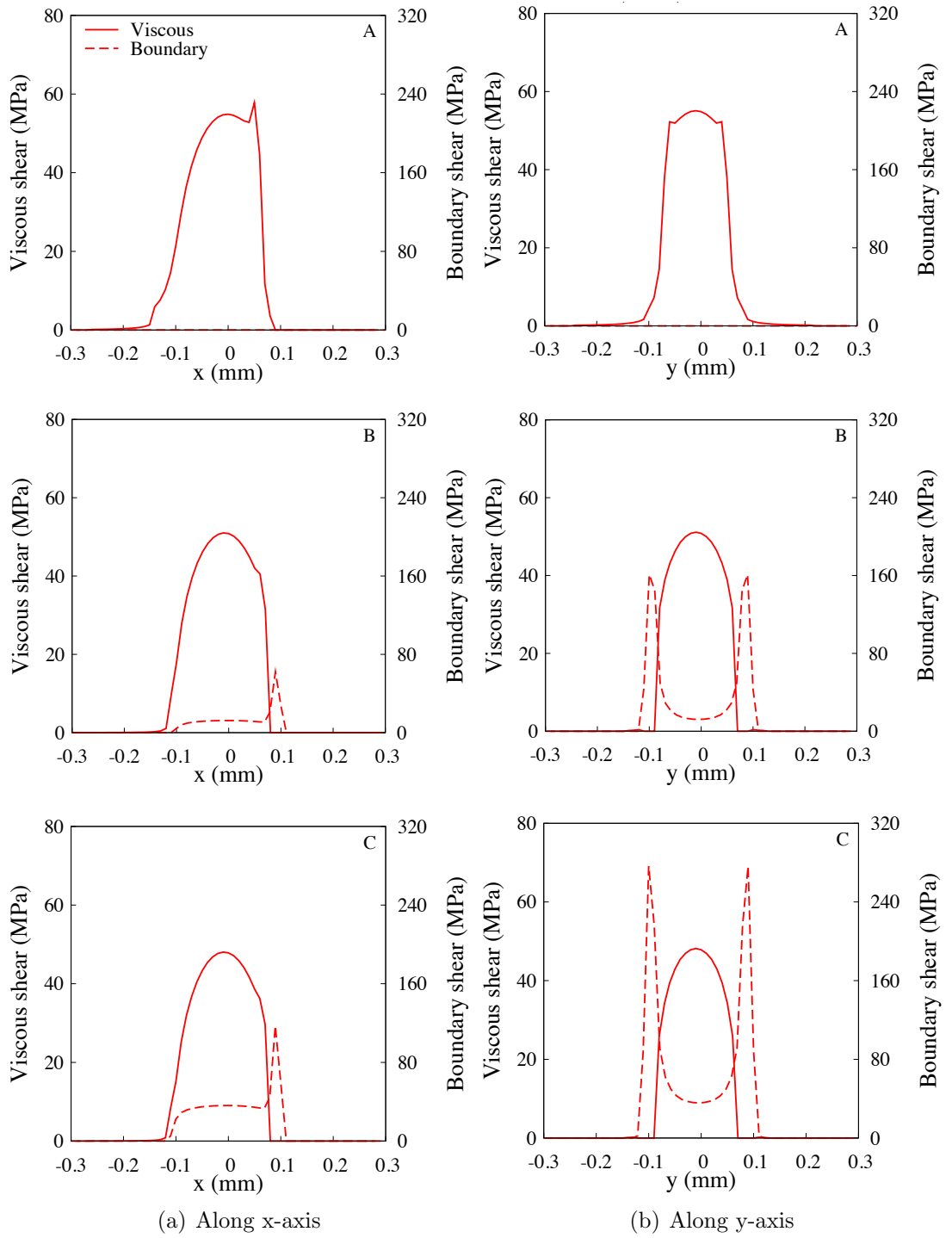


Figure 4.11: Viscous and boundary shear properties for point contact lubricated with SAE15W40 grade engine lubricant

## 4.4 Biodiesel production using transesterification process

In the current study, laboratory-grade biodiesel is synthesized using various types of feedstocks. Generally, biodiesel can be produced from any triglycerides of vegetable oil or animal fat origins through the transesterification process. The process requires a simple global reaction involving the reactants of triglycerides and alcohol reacted at sufficient temperatures with the assistance of acid, alkaline or lipase catalysts. The reaction will produce methyl esters (biodiesel) and the co-product of crude glycerol. The possibility of using any combinations of triglycerides and alcohols mean that biodiesel can have a range of physical properties and chemical compositions.

In this chapter, biodiesels derived from commercially available feedstocks, such as palm, coconut, soybean, olive, canola, and hydrogenated vegetable oil (shortening) were selected. The fatty acid methyl ester compositions for the tested biodiesels are given in Table 4.3. The selection of various types of feedstocks is aimed at representing the entire saturated-unsaturated and monounsaturated-polyunsaturated FAME ranges as illustrated in the ternary plot in Figure 4.12.

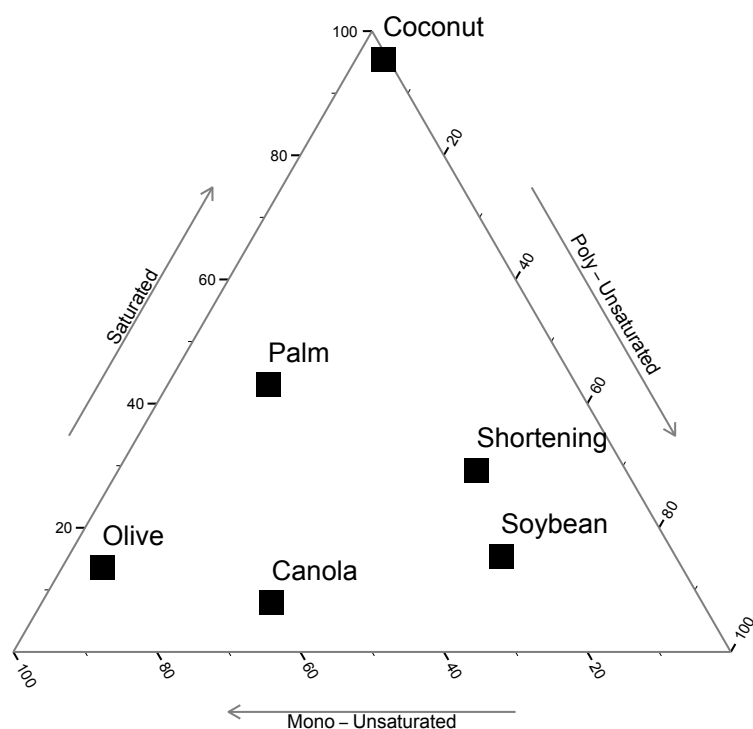


Figure 4.12: Ternary plot describing the fatty acid methyl ester composition for the tested biodiesels

Transesterification or alcoholysis replicates the process similar to hydrolysis, which displaces an alcohol from an ester to another type of chemical reaction [106]. There are three general methods in deriving biodiesels: 1) transesterification, 2) pyrolysis and 3) micro-emulsification [107]. The transesterification reaction produces biodiesel with small amount of glycerol and free fatty acids [62]. The flow chart of biodiesel process is shown in Figure 4.13, and the general transesterification reaction is given in Figure 4.14.

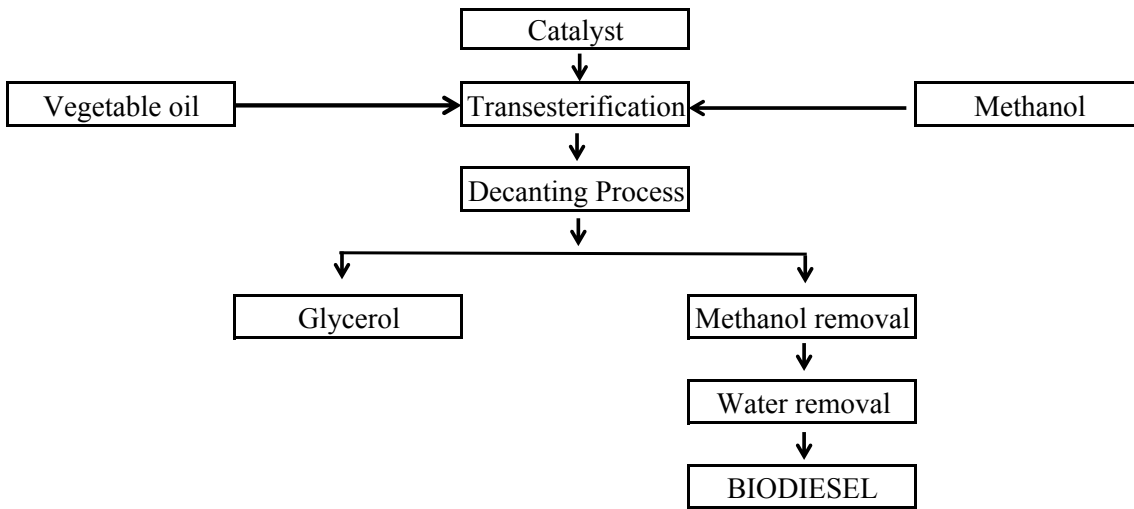


Figure 4.13: Flow chart of a biodiesel process

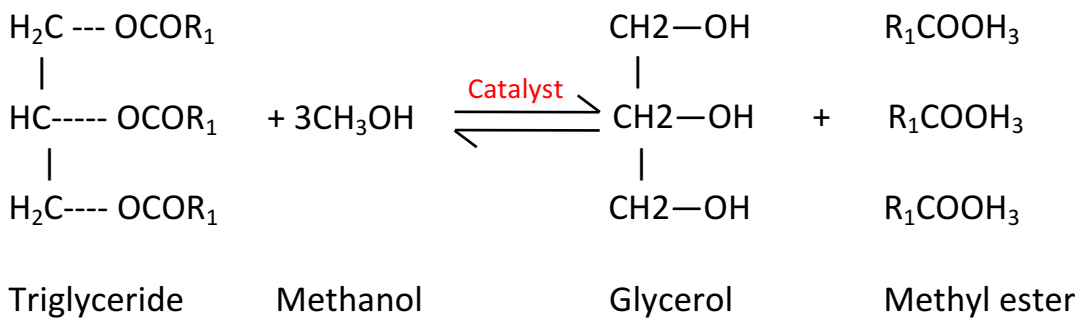


Figure 4.14: Transesterification reaction derived from vegetable oil

Table 4.3: Fatty acid methyl ester compositions for tested biodiesels [108][109]

<b>Type of biodiesel</b>	<b>8:0</b>	<b>10:0</b>	<b>12:0</b>	<b>14:0</b>	<b>16:0</b>	<b>18:0</b>	<b>18:1</b>	<b>18:2</b>	<b>18:3</b>
Coconut	8.3	6.0	46.7	18.3	9.2	2.9	6.9	1.7	0
Canola	0	0	0	0.1	3.9	3.1	60.2	21.1	11.1
Olive	0	0	0	0	11	3.6	75.3	9.5	0.6
Palm	0	0	0.9	1.3	43.9	4.9	39.0	9.5	0.3
Shortening	0	0	0	0.5	23.4	5.0	29.4	34.0	3.2
Soybean	0	0	0	0.1	10.3	4.7	22.5	54.1	8.3

All of the biodiesels are produced using the same method, where pre-heated triglycerides from vegetable oil, hydrogenated vegetable oil and duck fat are reacted with premixed lye and methanol. The triglycerides are preheated at a fixed temperature of 55°C for an hour to ensure that all of the feedstocks are in liquid phase. A 1%wt catalyst loading of potassium hydroxide (KOH) and triglyceride-to-methanol molar ratio of 6:1 is used in the reaction to ensure minimal soap production. The reactants then undergo the transesterification process in a reacting vessel at 55°C for a residence time of four hours. Crude glycerol as co-product is removed and the biodiesel is washed to remove soap and another contaminant. The process of producing biodiesel is completed when water is completely evaporated away from the biodiesels at the high temperature of 120°C. This process is to ensure that the biodiesel yield is at least 96.5% (m/m) of ester content (as required by EN 14214 biodiesel standards). Upon completion of the transesterification process, the kinematic viscosities and densities for the selected biodiesels are measured and given in Table 4.4.

Table 4.4: Bulk density for selected biodiesels

Type of biodiesel	Density (g/cm <sup>3</sup> )
Canola	0.8784
Coconut	0.8742
Olive	0.8779
Palm	0.8730
Shortening	0.8397
Soybean	0.8854

## 4.5 Friction measurements *for biodiesel*

In this section, frictional characteristics of biodiesel derived from vegetable oils (coconut, soybean, palm, olive and canola) and hydrogenated vegetable oil (shortening) are measured under pure sliding motion using a tribometer configured for pin-on-disc setup. A detailed analysis is conducted to interpret the friction force and the transition points at each of the lubrication regimes experienced by the contact lubricated with the selected biodiesels. It is to note that the same type of wear disc and pin as the ones used for SAE grade lubricant friction testings are used for biodiesel friction testing.

The curves plotting the coefficient of friction against linear sliding velocity for the tested biodiesels are given in Figure 4.15. The calculated standard deviation were found to be very small and ranged from 0.00015N to 0.0041N with respect to the coefficient of friction.

With increasing sliding velocity, it can be seen that all the tested biodiesels show a distinct transition from BL to ML and finally to EHL regime. However, these characteristic curves seem to shift horizontally along the linear sliding velocity axis, showing a varying transition velocity (to be known as critical velocity) from EHL to ML regime for different types of biodiesels. Through the friction test, coconut and shortening biodiesels are observed to transit from ML to EHL regime at the lowest and highest critical velocity, respectively. This shows that coconut biodiesel has the capability of sustaining fluid film lubrication for a larger range of linear sliding velocities as compared to the other types of biodiesels. Roegiers and Zhmud [15] relate such behaviour



to an increased friction modifier effect, where the protective layer, adsorbing to the metal surfaces, functions to expand the borders of the fluid film lubrication regime to withstand a larger operating range of sliding velocity, eventually delaying the onset of boundary lubrication.

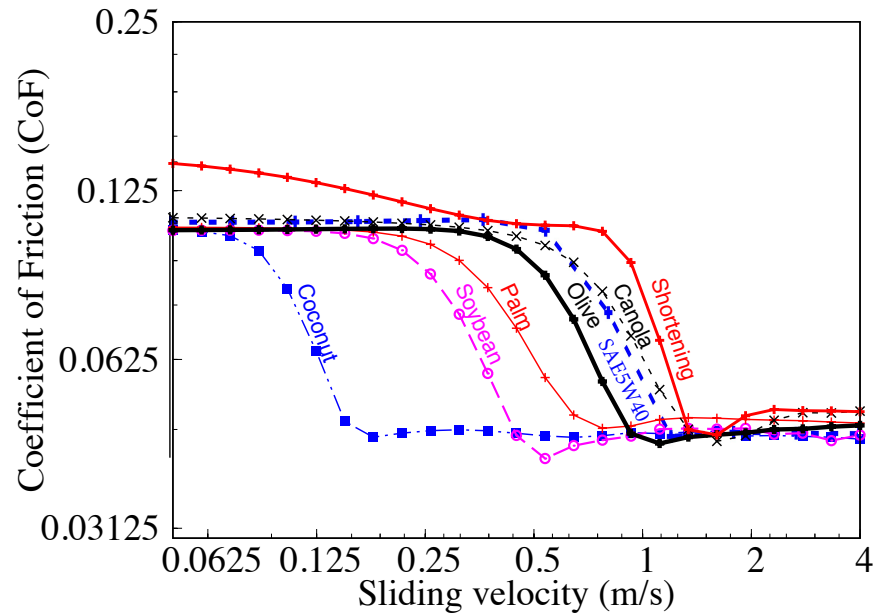
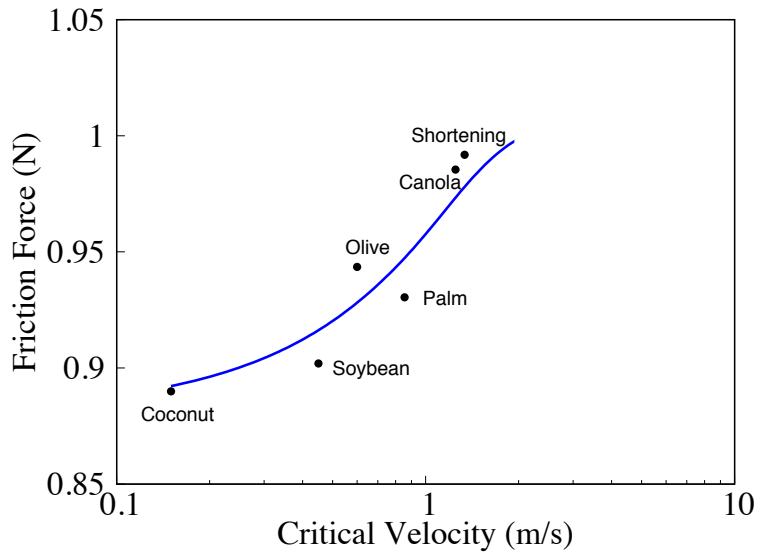
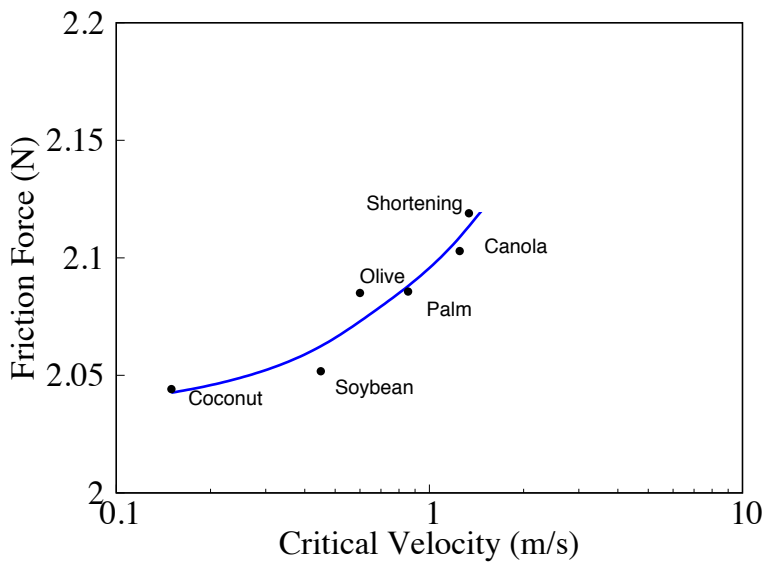


Figure 4.15: Coefficient of friction (CoF) measured at varying sliding velocity at 20N load for tested biodiesels compared with SAE5W40 standard lubricant

With the tested biodiesels showing different friction modifier effect (varying critical velocities), the influence of the critical velocity values towards the frictional properties for the tested biodiesels are investigated as shown in Figure 4.16. The friction forces are taken as the average friction values along EHL and BL regimes respectively. For the tested biodiesels, Figure 4.16(a) illustrates the increase in friction force along the EHL region when the critical velocity increases before plateauing at approximately 2 m/s. Such increase in friction with higher critical velocity is because of the reduced friction modifier effect (see Figure 4.15), resulting in a less effective fluid film lubrication along the EHL regime. In Figure 4.16(b), the boundary friction is plotted against the critical velocity for the tested biodiesels.



(a) Average friction force along elasto-hydrodynamic lubrication (EHL) regime



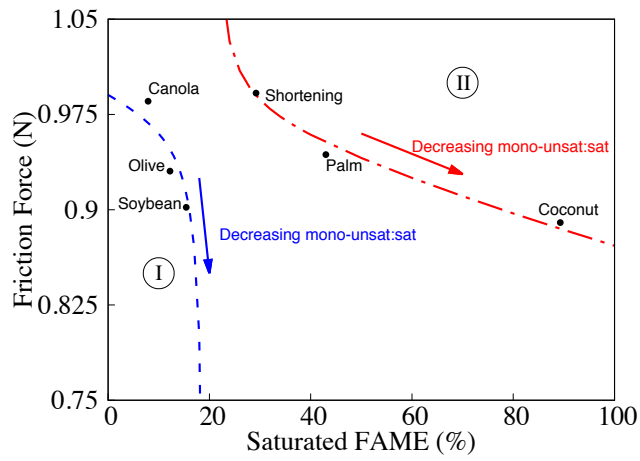
(b) Average friction force along boundary lubrication (BL) regime

Figure 4.16: Average friction force variation with critical velocity values at (a) EHL (b) and BL regimes for tested biodiesels

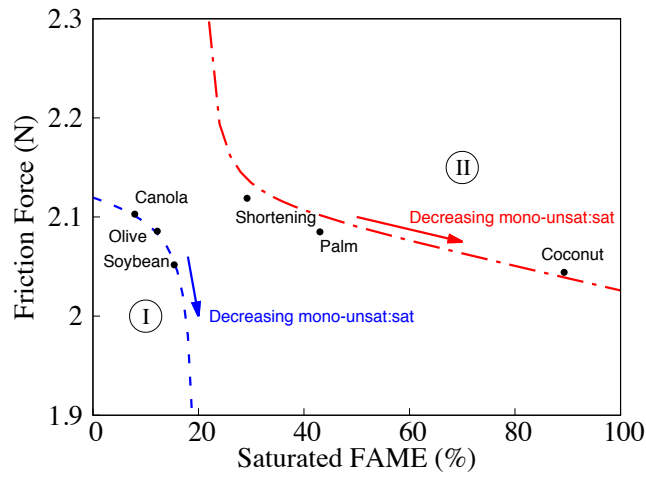
Along the BL regime, lubrication is typically through the formation of boundary adsorbed thin film, which provides the final barrier to inhibit direct surface-to-surface interaction. For the selected test conditions at room temperature, coconut biodiesel, with the lowest critical velocity value, exhibits a more effective boundary lubrication property than the other types of tested biodiesels. Such characteristic portrayed by coconut biodiesel is similar to those of anti-wear agent and/or extreme-pressure additives. With escalating critical velocity, the boundary friction is observed to have increased by 3.3%. The increased friction force along this region could potentially lead to the rupture of the boundary-adsorbed film. This can be observed in Figure 4.15 for shortening biodiesel, where the coefficient of friction begin to increase beyond its boundary friction value below sliding velocities of 0.5 m/s, respectively, indicating dry contact occurrence as a result of the boundary adsorbed thin film rupturing along the contact region under pure sliding motion.

The results thus far focus mainly on the friction forces of the tested biodiesels. To determine the undermining factor affecting the varying friction modifier effect, Figure 4.17 illustrates the influence of the FAME saturation level towards the frictional properties for each of the tested biodiesels. By using a rational function to curve fit the average friction force along the EHL region against percentage of the total saturated FAME content, two distinct groups of biodiesels are observed. For each of the distinct groups, average friction force reductions can be seen with higher saturation level of FAME composition. This is because the saturated molecules have higher tendency to align themselves to the surface to form a more compact and effective lubrication layer [110].

From Figure 4.17, the first group (to be known as Group I) consists of canola, olive and soybean derived biodiesels while the second group (to be known as Group II) consists of shortening, palm, and coconut derived biodiesels. The distinction between the two groups can be made based on the melting temperature for each of the feedstocks used to derive the tested biodiesels. Referring to Table 4.5, the melting temperatures for the feedstocks used to derive Group I biodiesels are observed to occur at sub-zero temperatures while the opposite can be seen for the feedstocks used to derive Group II biodiesels. It is to note that Group I biodiesels are derived mainly from winter crops (canola, olive and soybean) while Group II biodiesels are derived from summer crops (palm and coconut), and hydrogenated vegetable oil (shortening).



(a) Average friction force along elasto-hydrodynamic lubrication (EHL) regime



(b) Average friction force along boundary lubrication (BL) regime

Figure 4.17: Average friction force along (a) EHL and (b) BL regimes with the amount of saturated fatty acid composition

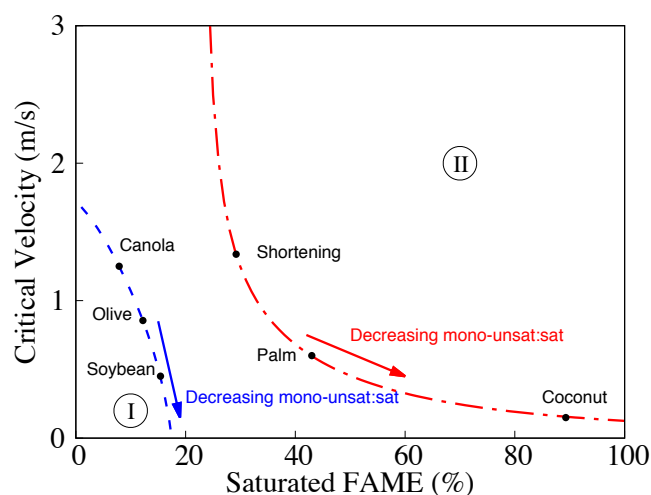
Table 4.5: Melting temperature for feedstocks used to derive the tested biodiesels

Type of feedstock	Melting temperature ( $^{\circ}\text{C}$ )
<b><i>Group 1</i></b>	
Canola	-10
Olive	-6
Soybean	-16
<b><i>Group 2</i></b>	
Coconut	25
Palm	35
Shortening	48

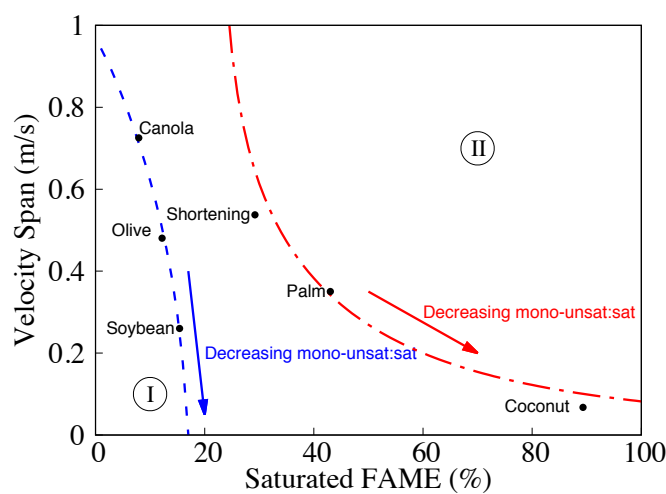
Following the trend lines for each of the groups (blue and red dotted lines) respectively, the average friction force along the EHL regime is seen to decrease with lower ratio of mono-unsaturated to total saturated FAME content. In Figure 4.17(b), similar characteristic is also being observed for the average friction force along the BL regime, where the tested biodiesels are divided into the two similar distinct groups as shown in Figure 4.17(a). A decreasing boundary friction is also measured when the biodiesel composition consists of lower ratio of mono-unsaturated to total saturated FAME content.

As pointed out earlier, the critical velocity, where the transition from ML to EHL occurs, plays an important role in determining the friction modifier effect portrayed by a lubricant, especially for the tested biodiesels in this study. Figure 4.18(a) shows the critical velocity for the tested biodiesels as the function of the saturated FAME content. Similar to that of Figure 4.17, the biodiesels can also be divided into the two similar distinct groups (Group I and Group II). The critical velocity values are also observed to reduce with decreasing ratio of mono-unsaturated to total saturated FAME content for both Group I and Group II biodiesels. This reflects on an improved friction modifier effect when the amount of mono-unsaturation level in the biodiesel is reduced with respect to the saturation level. Along ML regime, both the fluid film and also the asperity pairs in contact share the load carrying capacity of the contact. In Figure 4.18(b), the velocity span (where ML regime occurs) is shown to shrink with reduced ratio of mono-unsaturated to total saturated FAME content. A smaller ML

velocity span (e.g. coconut biodiesel) would see to an abrupt leap from ML to BL regime, resulting in a near-sudden undesirable increase in friction. This could be as a consequence of the fluid film having smaller load carrying capacity, which would result in a faster and easier fluid film rupture when being sheared under high contact pressure, leading to increased boundary interaction that imparts higher friction.



(a) Critical velocity



(b) Mixed lubrication velocity span

Figure 4.18: Friction modifier properties: (a) Critical velocity and (b) Mixed lubrication velocity span of the biodiesels

From the measured frictional properties, it is to note that no trend could be found

relating the weighted average chain length to the lubrication properties of the tested biodiesels (each of the biodiesels in Group I and Group II has an average chain length of 18 and 17 carbon atoms, with the only exception being coconut derived biodiesel, which has an average chain length of 13 carbon atoms), which is aligned to the suggestion by Wadumesthrige *et al.* [110]. For the analysis conducted thus far, there is also no net evidence that could be observed in terms of the effect of polyunsaturated FAME compositions towards the lubrication properties of the tested biodiesels.

#### 4.5.1 Ternary plot mapping of biodiesel frictional properties

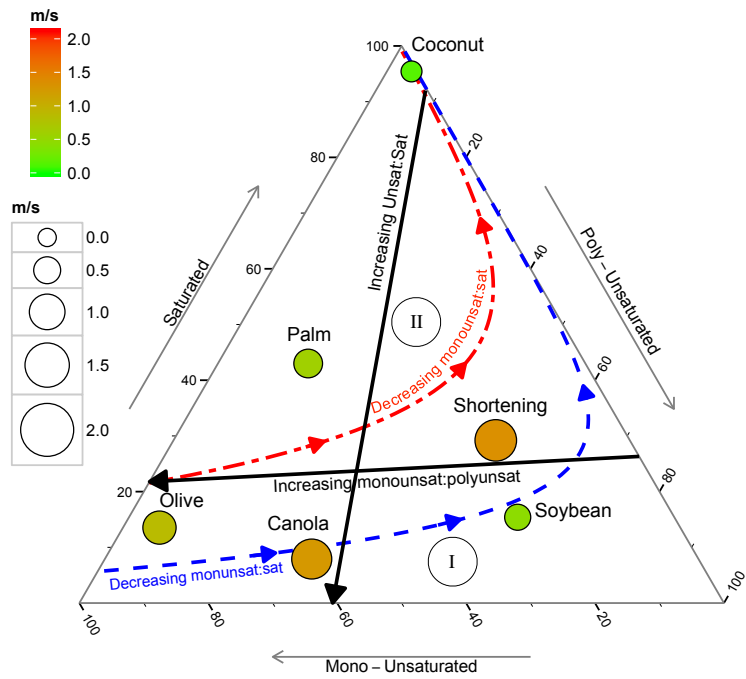
Both sets of Figures above show a relation between the fatty acid composition and the frictional properties for each of the tested biodiesels, dividing them into Group I and Group II. To further understand the influence of the fatty acid composition on the biodiesel lubrication properties, Figure 4.19 maps the critical velocity and ML velocity span on a ternary plot, indicating the fatty acid composition for each of the tested biodiesels. Adopting a ternary plot in this study allows for the mapping of the frictional properties with respect to the tri-axial saturated, mono-unsaturated and poly-unsaturated FAME compositions for each of the tested biodiesels.

As an initial step to map the critical velocity and ML velocity span using a ternary plot, two global axes, showing: 1) increasing ratio of unsaturated to saturated and 2) mono-unsaturated to poly-unsaturated FAME content, are determined from the fatty acid composition for the selected biodiesel types. It is interesting to note that the axis representing the increasing ratio of mono-unsaturated to poly-unsaturated FAME content splits the biodiesel types into the two groups (Group I and Group II) identical to the ones obtained in Figure 4.17 and Figure 4.18. This shows a reasonably good correlation between the two distinct approaches considering that the ternary plot approach takes into account only the FAME composition of the biodiesels.

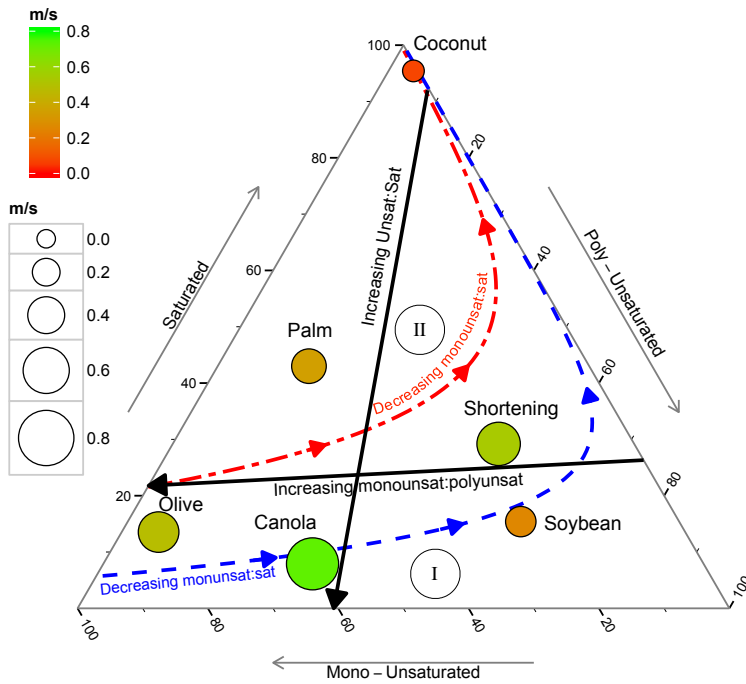
In the ternary plots given in Figure 4.19(a) and (b), the direction of the blue (Group I) and red (Group II) dotted lines represent the decreasing ratio of the mono-unsaturated to total saturated FAME content, calculated from the FAME composition of the tested biodiesels, which coincidentally also indicates a trend in decreasing critical velocity (see Figure 4.19(a)) and ML velocity span (see Figure 4.19(b)) for the selected biodiesels. Both these trends obtained are consistent with the observations in Figure

4.17 and Figure 4.18. This shows further proof that the frictional properties of the tested biodiesels are influenced by the ratio of mono-unsaturated to total saturated FAME content, once they are categorised into the two distinct groups based on the melting temperatures of the feedstock used to derive the respective biodiesels.





(a) Critical velocity



(b) Mixed lubrication velocity span

Figure 4.19: Ternary plot describing the change in critical velocity with the fatty acid composition for the tested biodiesels

## 4.6 Summary

In order to validate the point contact model lubricated by commercially available SAE grade lubricants under pure sliding, friction tests are carried out using a tribometer with a pin-on-disc setup. Friction forces are measured at various sliding velocities in order to obtain the tribological characteristics of the lubricants at different lubrication regimes. Through the measured friction forces, all the tested lubricants exhibit lubricant transition properties, similar to a lubrication Stribeck curve. Using the same sliding velocity range, the mathematical model for a lubricated point contact as discussed in the previous chapters are used to simulate the conditions of the friction test. It can be shown that the mathematical approach, coupling Reynolds solution in determining fluid film formation and rough surface contact model in determining viscous and/or boundary shear properties of the contact, is capable of predicting lubrication Stribeck curves that correlate well with the measured properties.

Besides these, coupling the mathematical model and the experimental approach, when correlating simulation to measured data, allowed for the determination of lubricant non-Newtonian properties along EHL and ML regimes (i.e. the lubricant limiting shear stress pressure relation  $\gamma$ ) and boundary lubrication properties along BL regime (i.e. pressure coefficient,  $\kappa$ ). Such empirical approach could prove to be beneficial in characterising the tribological properties of lubricants. With the mathematical model in predicting fluid film formation and friction validated for contacts lubricated with typical lubricants, the next chapter will proceed to the final phase of the study in determining the frictional properties of vegetable oil derived biodiesel. This will include the discussion on synthesizing of fatty acid methyl esters (FAME), which have great potential to be used as lubricant and/or lubricant additives. The chapter will also discuss on the measured frictional characteristics of the derived FAMEs.

This chapter also discussed on the frictional properties of biodiesel, derived from various types of vegetable oil, at different lubrication regimes under pure sliding motion. Based on the feedstocks' melting temperatures, it is shown that the frictional properties of the biodiesels can be divided into two distinct groups: Group I (feedstocks from winter crops) and Group II (feedstocks from summer crops and hydrogenated vegetable oil). For each of the groups, when the ratio of mono-unsaturated to total saturated FAME content decreases, friction forces for both EHL and BL regimes reduce because

of improved friction modifier effect, delaying the onset of ML and BL regimes. Among the selected biodiesels, coconut biodiesel exhibits the better friction modifier effect with the smallest friction force along both the EHL and BL regimes.

While these properties improve with lower ratio of mono-unsaturated to total saturated FAME content, the load carrying capacity of the lubricated contact along the ML regime reduces, increasing the rupture ability of the fluid film. It is recommended that an ideal lubricant should have the lowest possible friction force values with the highest possible load carrying capacity. Therefore, by coupling the friction force curves together with the ternary plots, it could then be deduced that soybean biodiesel actually boast a more balanced set of lubrication properties, showing better potential as a bio-lubricant/additive when compared with the other tested biodiesels.

Based on the work covered in this chapter, frictional properties of biodiesel are now better understood. In the next chapter, using the measured frictional properties, the current study attempts to apply the derived mathematical model, for predicting fluid film formation and friction forces along typical lubricated contact, to simulate a point contact lubricated by biodiesel.

# Chapter 5

## Simulation of biodiesel tribological properties

### 5.1 Preliminary simulation findings

This section discusses on preliminary simulated tribological findings of biodiesel using the Reynolds solution discussed in earlier chapters. The Reynolds solution has been used to validate for the tribological properties of SAE grade lubricant. Table 5.1 refers to the rheological properties for the selected biodiesels used in predicting contact pressure distribution and lubrication film profiles. As mentioned in the previous chapter, the wear discs and pins used for biodiesel friction testings are the same as the ones used for SAE grade lubricants. Hence, the Greenwood and Tripp rough surface parameters follow the one given in Table 3.5.

Table 5.1: Experimentally measured rheological properties of selected biodiesels

Type of biodiesel	Bulk Viscosity $\eta_0$ (mPa.s)	Density $\rho_0$ , (kg/m <sup>3</sup> )
Coconut	3.2011	874.2
Palm	5.1459	873.0
Soybean	4.7894	885.4

Also, as shown in the earlier chapters, to simulate a lubricated contact, it is essential to consider the viscosity-pressure and density-pressure properties of the lubricant itself,

especially along lubrication regimes, such as EHL and ML. Unlike mineral oil-based lubricants, for biodiesel, recent research conducted by Chum-in *et al.* [111] and Phankosol *et al.* [112] showed that biodiesel viscosity and density model for high pressure applications can be described using Gibbs energy additivity approach. The biodiesel viscosity and density relation with pressure and temperature can be calculated from its average carbon number ( $z_{ave}$ ) and average number of double bonds ( $nd_{ave}$ ) [111]. The equation for biodiesel viscosity and density relation with pressure and temperature can be determined as below:

$$\begin{aligned} \ln(\eta_0) = \ln(\eta_{atm}) + p' \times & \left( 0.0006 - 0.000011 \times z - 0.00022 \times nd_{ave} \right. \\ & \left. + \frac{0.0415 + 0.0103 \times z_{ave} + 0.054 \times nd_{ave}}{T} \right) \end{aligned} \quad (5.1)$$

$$\begin{aligned} \ln(\rho_p) = \ln(\rho_{atm}) + p' \times & \left( 0.000228 - 0.0000026 \times z_{ave} - 0.000006 \times nd_{ave} \right. \\ & \left. + \frac{-0.0416 + 0.000317 \times z_{ave} + 0.00223 * nd_{ave}}{T} \right) \end{aligned} \quad (5.2)$$

where the average number of carbon atom ( $z_{ave}$ ) and the average number of double bonds ( $nd_{ave}$ ) for the FAME compositions can be calculated accordingly using the equation below. Table 5.2 shows the average number of carbon atom ( $z_{ave}$ ) and the average number of double bonds ( $nd_{ave}$ ) for biodiesels selected for the current study.

$$z_{ave} = \frac{\sum_{i=1}^n x_i z_i}{\sum_{i=1}^n x_i} \quad (5.3)$$

$$n_{d(ave)} = \frac{\sum_{i=1}^n x_i n_{d(i)}}{\sum_{i=1}^n x_i} \quad (5.4)$$

Table 5.2: Average carbon number and average number of double bond for vegetable oil derived biodiesel [111]

Type of biodiesels	$z_{ave}$	$nd_{ave}$
Coconut	12.97	0.103
Palm	17.01	0.591
Soybean	17.79	1.556

To apply these viscosity and density equations to the Reynolds solution proposed in this study, discretisation as given below for these equations are used.

$$\bar{\rho}_{i,j} = e^{\frac{Ph \times P[i][j] - P_{atm}}{P_{atm}}} \times 0.000228 - 0.0000026 \times z_{ave} - 0.000006 * nd_{ave} + \frac{-0.0416 + 0.000317 \times z_{ave} + 0.00223 \times nd_{ave}}{T} \quad (5.5)$$

$$\bar{\eta}_{i,j} = e^{\frac{Ph \times P[i][j] - P_{atm}}{P_{atm}}} \times 0.0006 - 0.000011z - 0.00022 \times nd_{ave} + \frac{0.0415 + 0.0103z + 0.054 \times nd_{ave}}{T} \quad (5.6)$$

Figure 5.1 shows the contact pressure distribution and lubricant film profile of palm biodiesel and soybean biodiesel. Using the current Reynolds solution at sliding velocity equal to 4.0 m/s, it is found that fluid film thickness is predicted to be smaller as compared to the surface roughness of the given material (refer to Table 3.5) by one order of magnitude. Under this condition, it will lead to higher possibilities of having surface asperity contacts between the two surfaces, thus, causing boundary friction to appear. However, the measured coefficient of friction values for palm and soybean biodiesel is around 0.05 (see Figure 4.15) at 4.0 m/s, indicating EHL regime with possibly little to none boundary interaction. It is to note that for coconut biodiesel, the current set of mathematical solution failed to converge when used to simulate the fluid film formation properties of this biodiesel.

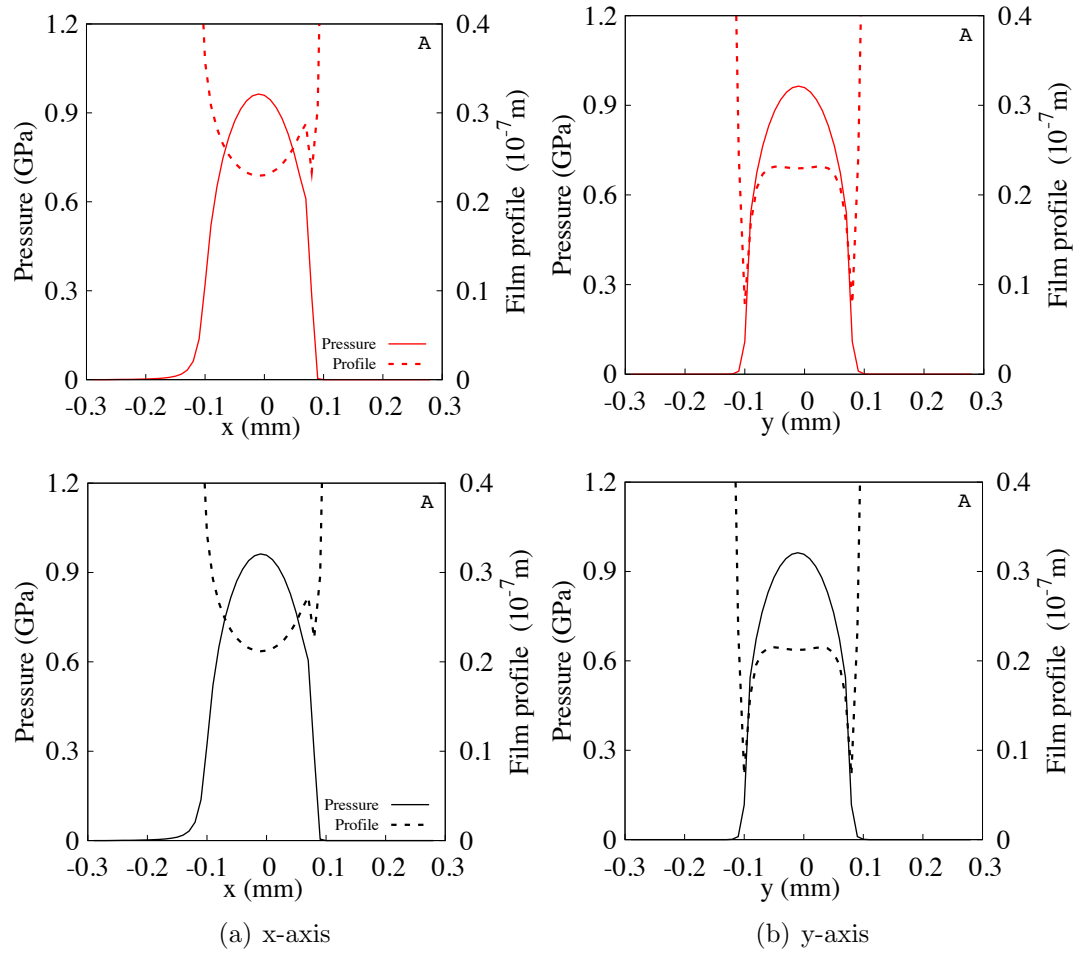


Figure 5.1: Contact pressure distribution and lubricant film profile for simulated point contact lubricated with palm and soybean biodiesel at sliding velocity of 4 m/s

In view of the vast difference between the predicted and measured operating lubrication regimes for palm and soybean biodiesel at 4.0 m/s, it is imperative that modifications will be required for the current set of mathematical models in better predicting the tribological properties for biodiesel. As mentioned earlier, the wear discs and pins used for the friction tests are taken to be the same for both SAE grade lubricants and biodiesel. Hence, this will then leave only the fluid film formation prediction component to be explored in improving the correlation of the simulated frictional properties of biodiesel as compared to the measured data.

## 5.2 Modified mathematical approach for biodiesel

In the current chapter, it is proposed that a simple modification to the classical Reynolds equation be applied for biodiesel. The proposed modified Reynolds equation is written as follow:

$$\frac{\partial}{\partial x} \left[ \frac{\rho h^3}{\eta} \frac{\partial p}{\partial x} \right] + \frac{\partial}{\partial y} \left[ \frac{\rho h^3}{\eta} \frac{\partial p}{\partial y} \right] = 12\chi \left[ \frac{\partial(\rho h U)}{\partial x} + \frac{\partial(\rho h V)}{\partial y} + \frac{\partial(\rho h)}{\partial t} \right] \quad (5.7)$$

where the term  $\chi$  is a factor introduced in an attempt to correlate two important parameters affecting biodiesel's lubrication properties: 1) average number of carbon atom ( $z_{ave}$ ) and 2) average number of double bonds ( $nd_{ave}$ ). As an initial approximation, the term  $\chi$  will be adjusted accordingly in order to fit the simulation to the experimental measurements for the selected biodiesels. From this approach, an equation for the term  $\chi$  as a function of average number of carbon atom and average number of double bonds for the biodiesels will then be derived.

The focus of this chapter is to mathematically predict the lubrication properties of biodiesel, derived using different feedstocks. Through a detailed series of simulation, it is expected that the modified Reynolds equation proposed in this chapter can be described as a function of average number of carbon atoms and average number of double bonds of the biodiesel's FAME composition. This will require integration of simultaneous solutions of the proposed modified Reynolds equation to define the fluid film thickness and its contact pressure distribution along a lubricated point contact. The output from the modified Reynolds solution will then be used to predict friction force using a rough surface contact model based on Greenwood and Tripp model.

As an initial approximation, the simulation is executed for point contact lubricated by biodiesels derived from coconut, palm and soybean vegetable oil. The lubrication Stribeck curves for coconut, palm and soybean vegetable oil derived biodiesels are simulated and given in Figure 5.2. In order to achieve good correlation between the simulation and experimental data, the term  $\chi$  introduced to the modified Reynold equation are adjusted accordingly, giving values of **365**, **53** and **61** for coconut, palm and soybean derived biodiesels, respectively. For these simulated parameters, it is demonstrated that the mathematical model based on the modified Reynolds equation is capable of capturing lubrication regime transition, from EHL to ML and finally BL



regime, with decreasing sliding velocities.

Table 5.3: Predicted values for friction estimation

Type of biodiesels	Pressure coefficient ( $\kappa$ )	Limiting shear stress-pressure relation $\gamma$
Coconut	0.1254	0.045
Palm	0.1075	0.048
soybean	0.1064	0.045

By measuring the pressure coefficient of the boundary shear strength,  $\kappa$  using the LFM approach similar to the ones for SAE grade engine lubricants and by fitting the simulation data to the measured frictional values for the  $\gamma$  values, Table 5.3 tabulates the input parameters required to compute friction forces using the derived mathematical model based on the modified Reynolds equation.

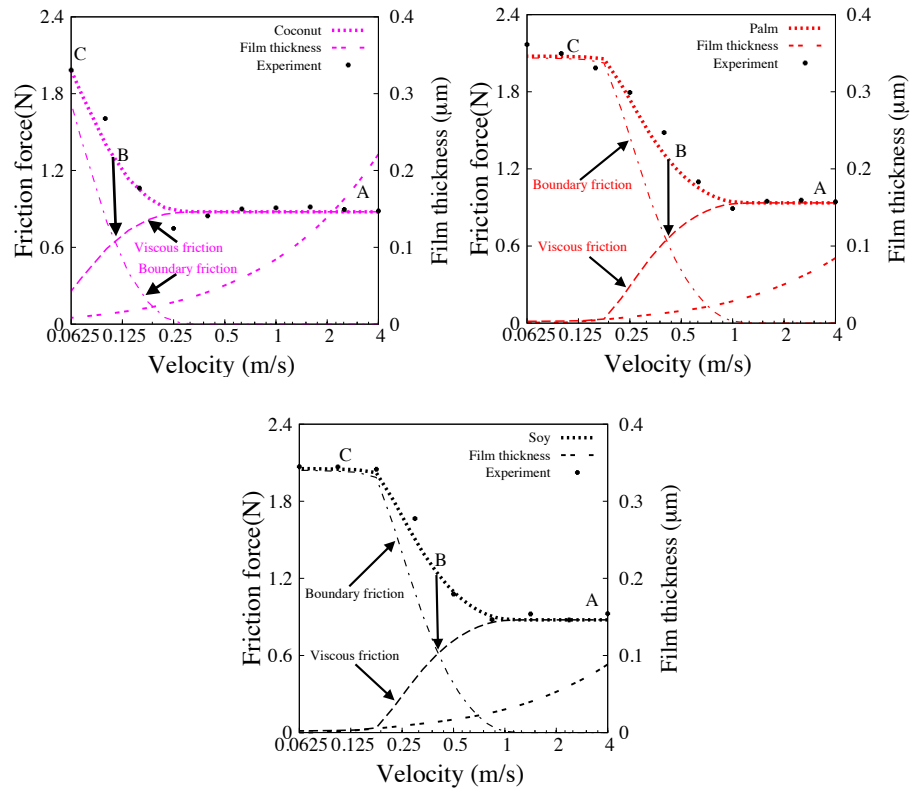


Figure 5.2: Lubrication Stribeck curve validation

Based on the proposed modifications to the mathematical model in predicting fluid film formation, Figure 5.3 shows the tribological properties of the simulated point contact lubricated with biodiesels, derived from coconut, palm and soybean, at sliding velocity of 4.0 m/s. At such sliding velocity, it can be seen that the contact pressure is in the range of GPa, showing a Hertzian like contact pressure. The contour of the lubricant film profiles for the simulated contacts are also included in Figure 5.3. The contact pressure distribution and lubricant film profile along the central cross section of x-axis and y-axis for biodiesels, derived from coconut, palm and soybean vegetable oil, are given in Figures 5.4, 5.5 and 5.6, respectively. The selected location A, B and C are annotated in Figure 5.2, representing fluid film lubrication, ML and BL regimes respectively for each of the simulated biodiesels.

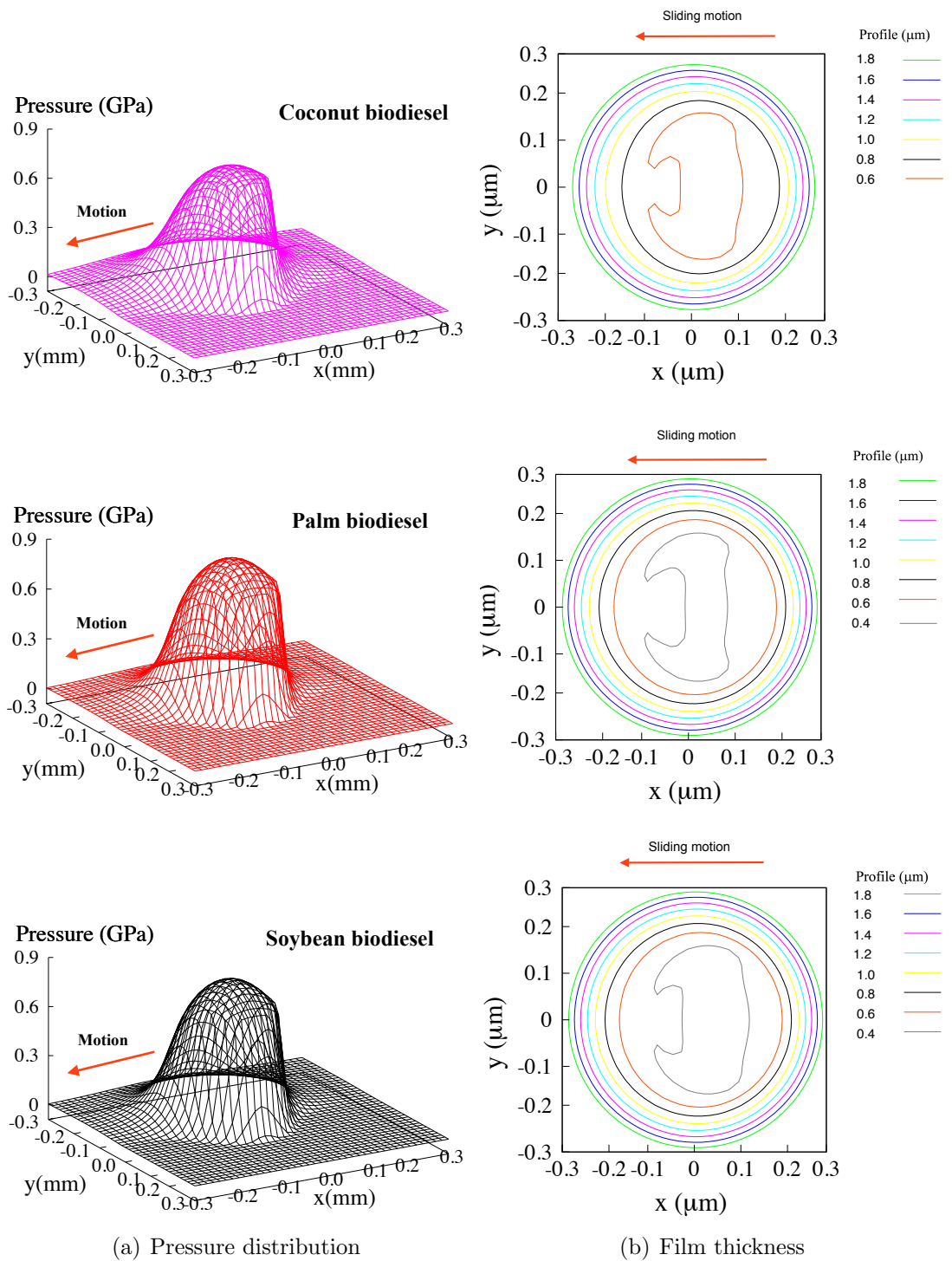


Figure 5.3: Contact pressure distribution and lubricant film profile for simulated point contact lubricated using biodiesels at sliding velocity of 4 m/s

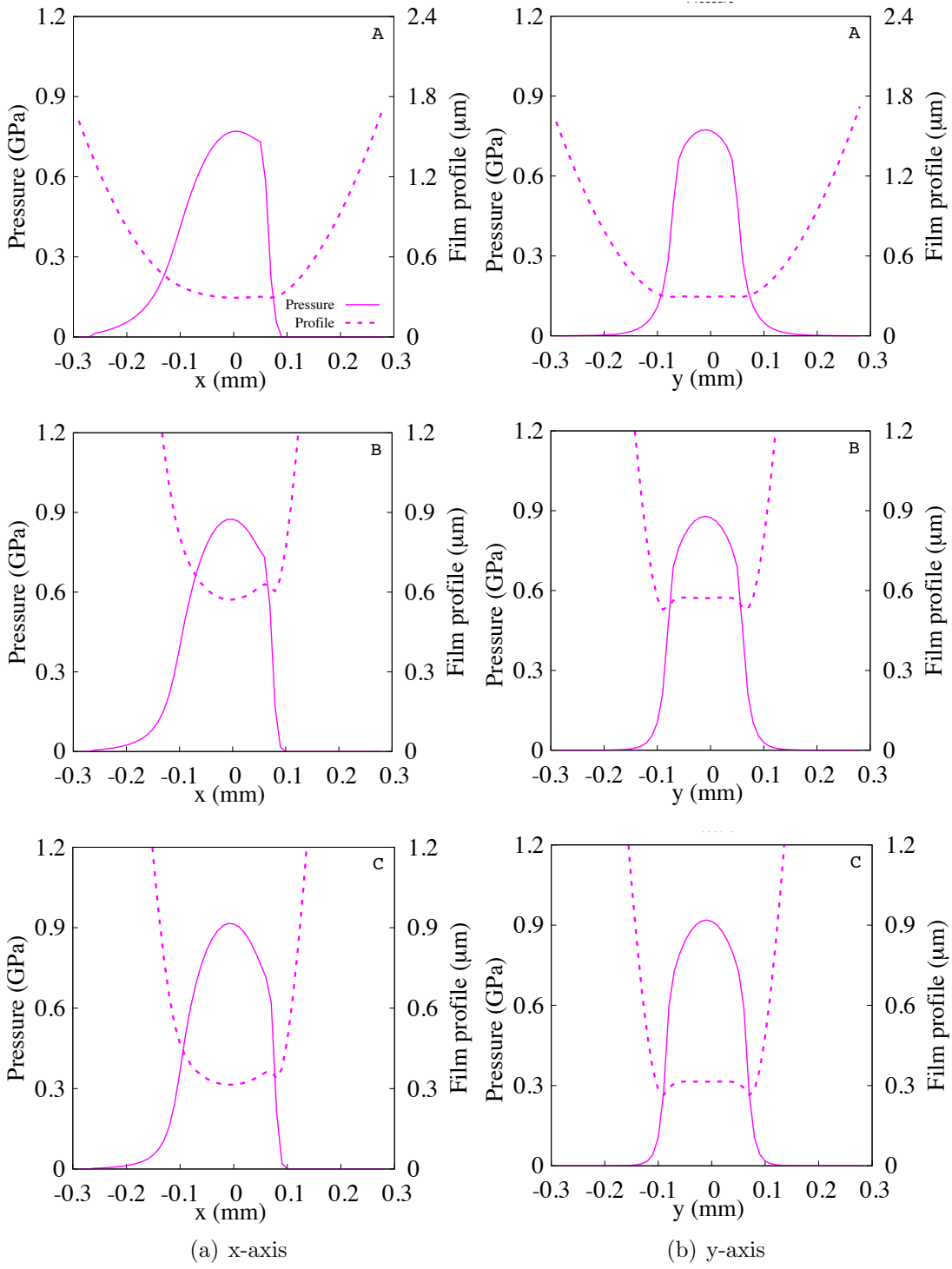


Figure 5.4: Contact pressure distribution and lubricant film profile at point contact lubricated for Coconut biodiesel

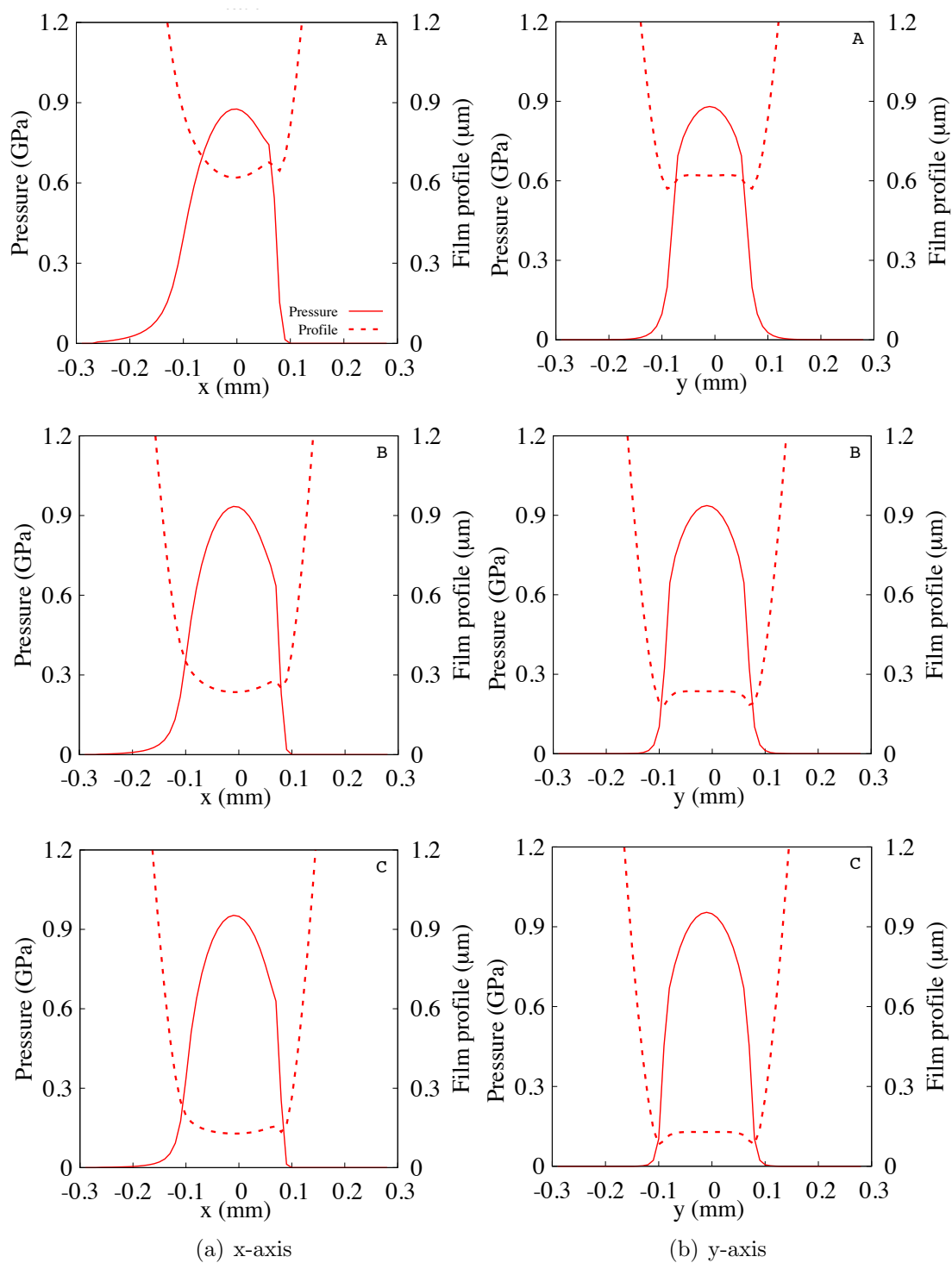


Figure 5.5: Contact pressure distribution and lubricant film profile at point contact lubricated for Palm biodiesel

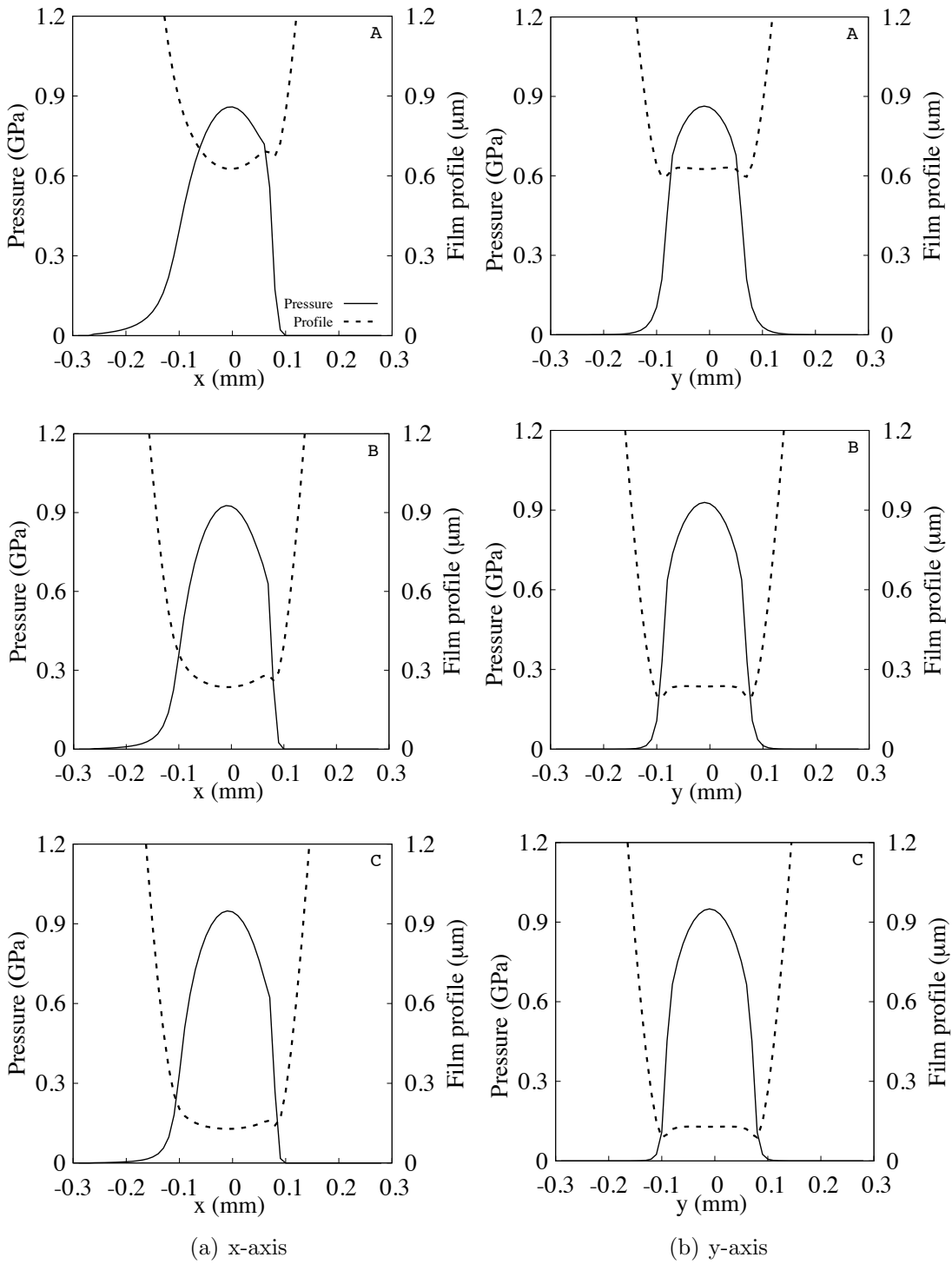


Figure 5.6: Contact pressure distribution and lubricant film profile at point contact lubricated for soybean biodiesel

Sliding velocity together with fluid film thickness play an important role in determining the lubrication regimes of any form of lubricants. With a smaller magnitude of fluid film appearing, there will be a higher chance of surface asperity contacts between the two surfaces, leading to more significant boundary friction. Referring to Figures 5.7 to 5.9, at location A (fluid film lubrication regime), it is clearly shown that viscous shear is dominating the overall friction for all three types of biodiesels. At this point, there are no possible asperity contact. For location B, where ML regime is expected, it is observed that for the tested biodiesels, the predicted shear properties show a mixture of viscous and boundary shear components. Meanwhile, at location C, the mathematical model illustrates a dominating boundary shear component for all the simulated biodiesels, indicating BL regime as shown in Figure 5.2.

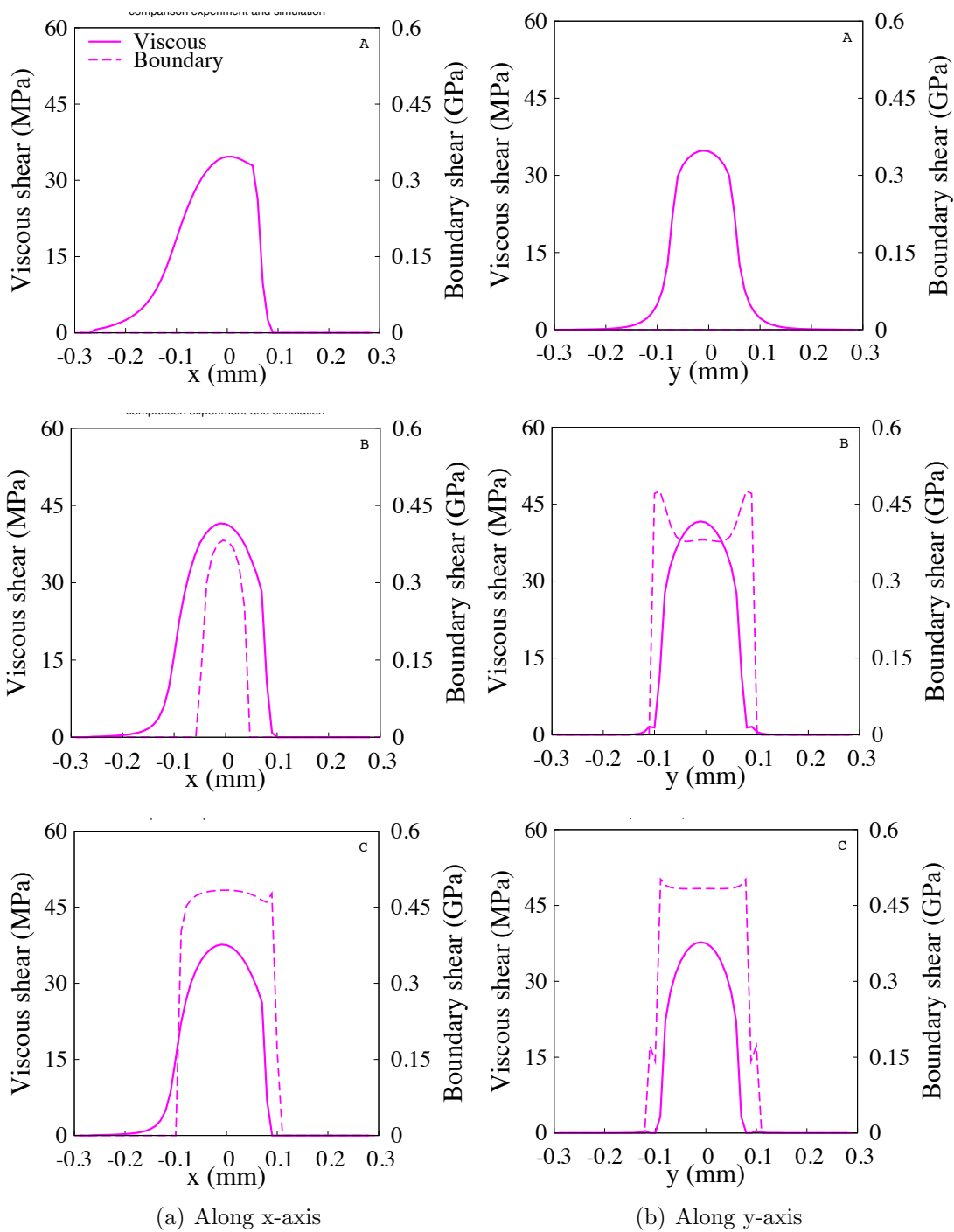


Figure 5.7: Viscous and boundary shear properties for point contact lubricated with Coconut biodiesel



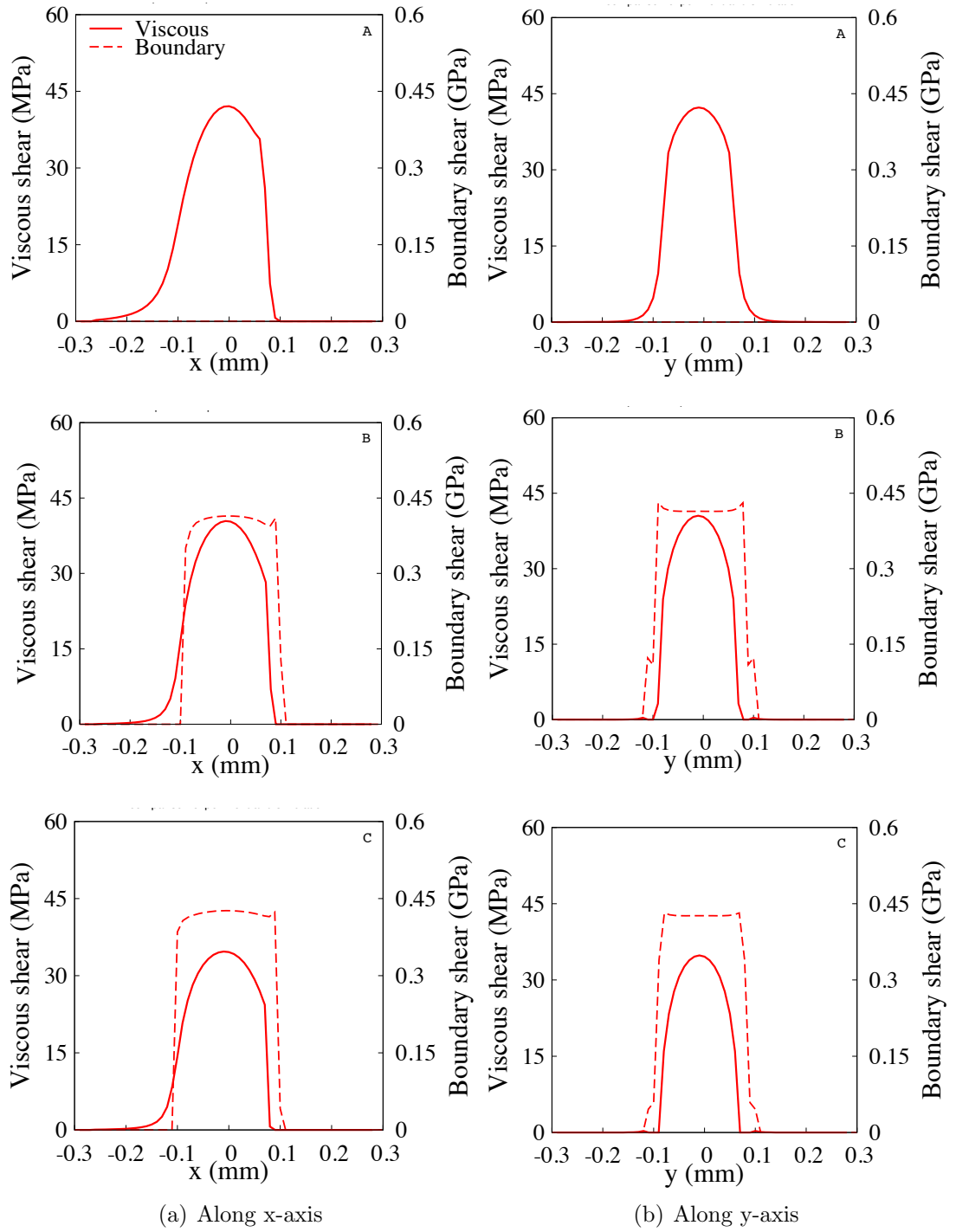


Figure 5.8: Viscous and boundary shear properties for point contact lubricated with Palm biodiesel

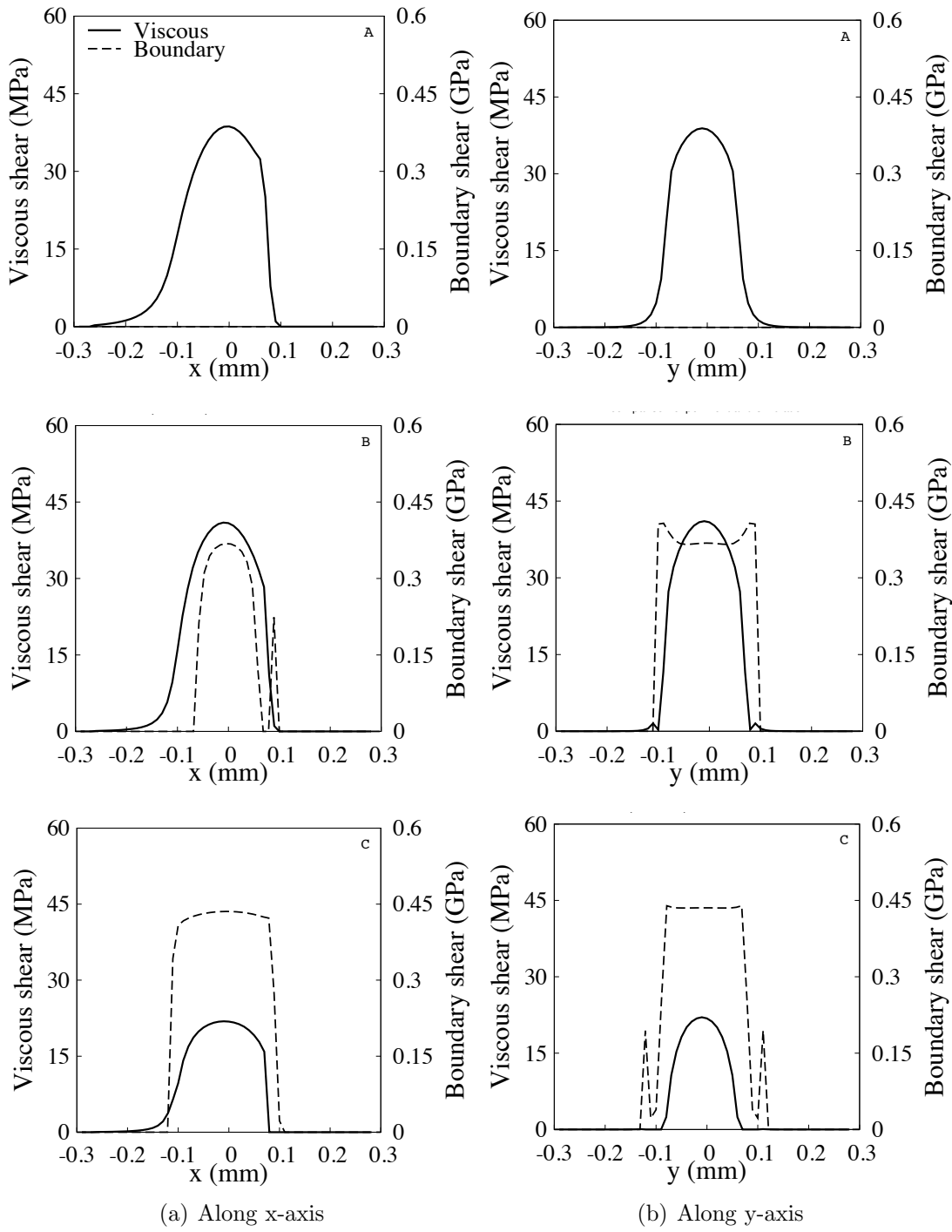


Figure 5.9: Viscous and boundary shear properties for point contact lubricated with soybean biodiesel

### 5.3 Relationship between FAME compositions and Reynolds equation

Table 5.4: Average carbon number and average number of double bond for vegetable oil derived biodiesel [111]

Type of biodiesels	$z_{ave}$	$nd_{ave}$
Canola	17.92	1.364
Olive	17.78	0.961

Table 5.5: Biodiesel rheological parameters

Type of biodiesel	Bulk Viscosity $\eta_0$ (mPa.s)	Bulk density $\rho_0$ , (kg/m <sup>3</sup> )
Canola	5.1716	871.1
Olive	5.5960	870.6

With good level of confidence on the ability of the proposed modified Reynolds equation discussed above, the model is then used to simulate other types of biodiesels, derived from canola and olive vegetable oil, with the relevant simulation input parameters given in Tables 5.4 and 5.5. By adjusting the term  $\chi$  to curve fit the simulation data with measured friction force values, the simulated lubrication Stribeck curves for these biodiesels are given in Figure 5.10. In order to correlate the predicted friction forces with the measured values, the  $\chi$  values are **26 and 32** for canola and olive biodiesel, respectively. Through this, the parameters required to determine the frictional properties along EHL and BL regimes for these biodiesels can also be ascertained and are given in Table 5.6. Figures 5.11 to 5.14 demonstrate the fluid film formation and shear properties across the contact conjunction when lubricated with biodiesel derived from canola and olive oil.

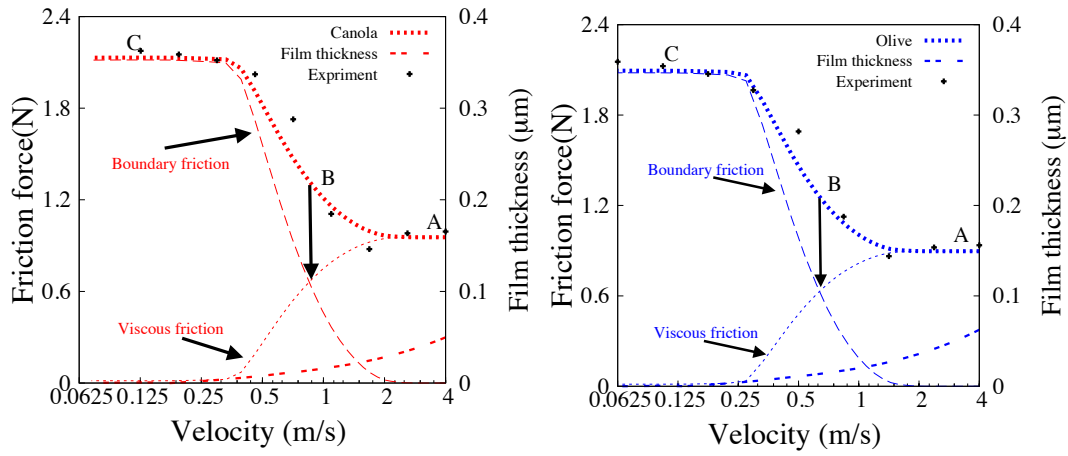


Figure 5.10: Stribeck curve validation

Table 5.6: Predicted values for friction estimation

Type of biodiesels	Pressure coefficient ( $\kappa$ )	Limiting shear stress-pressure relation $\gamma$
Canola	0.1104	0.049
Olive	0.1085	0.046

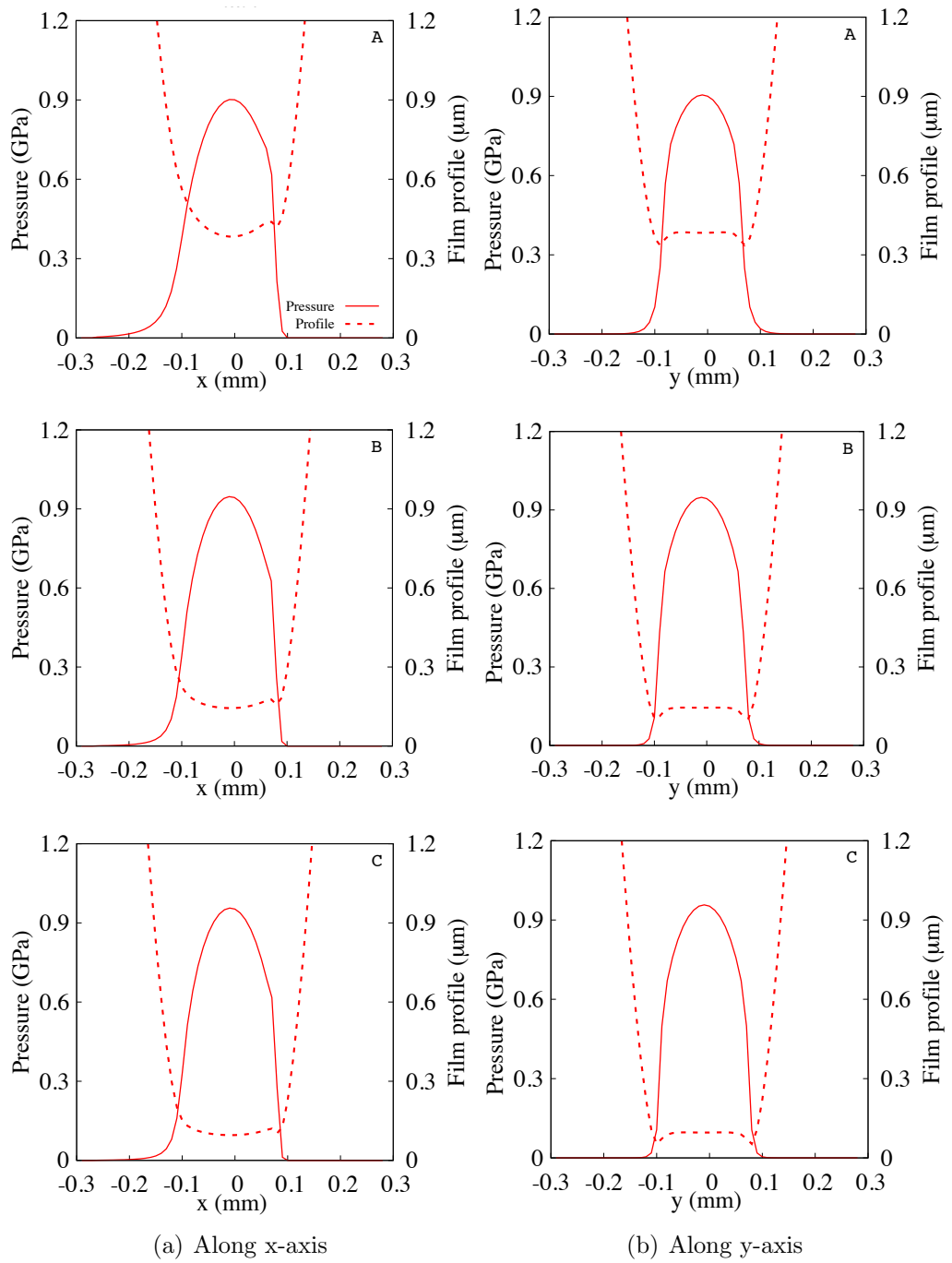


Figure 5.11: Contact pressure distribution and lubricant film profile for point contact lubricated with canola biodiesel

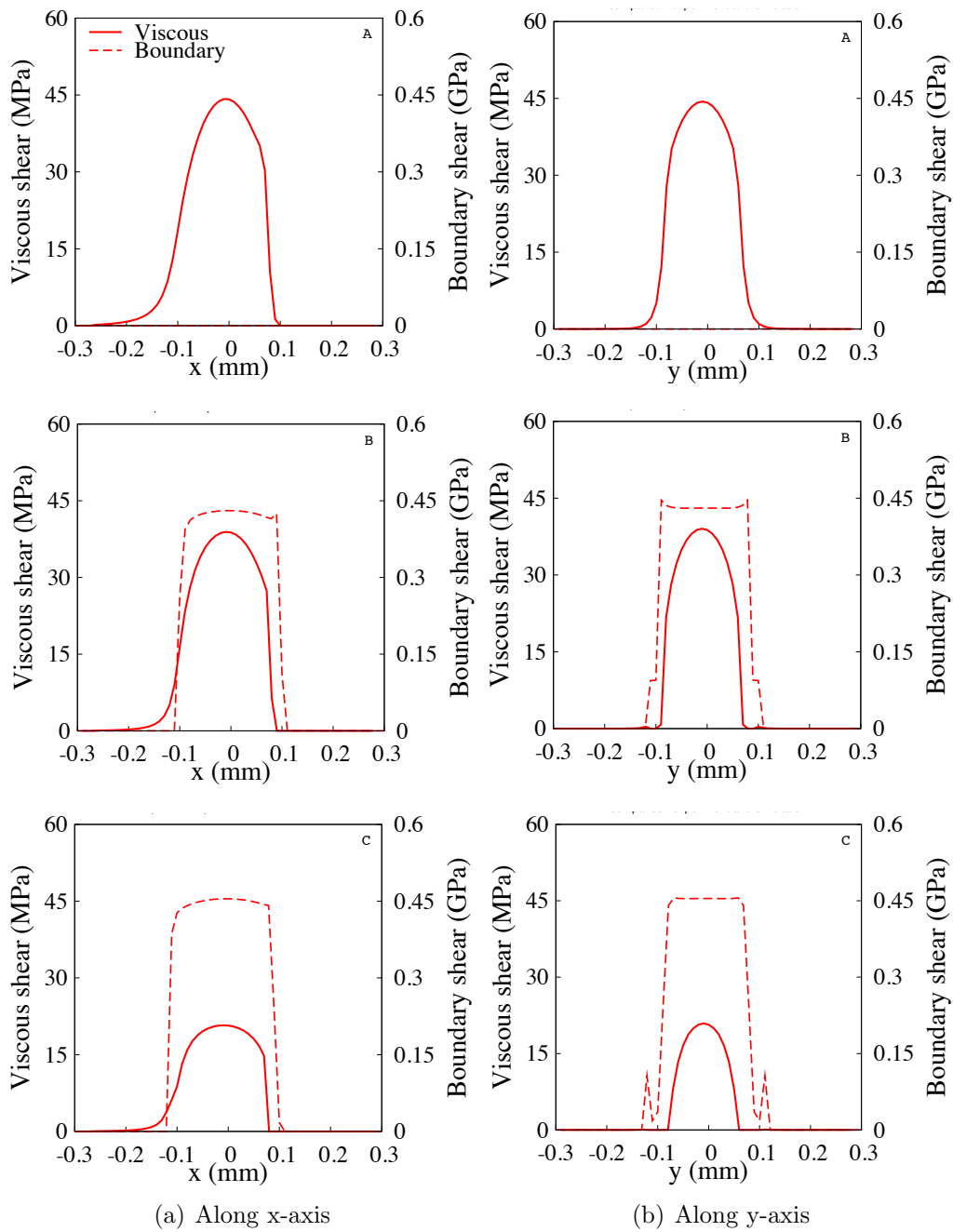


Figure 5.12: Viscous and Boundary shear properties for point contact lubricated with canola biodiesel

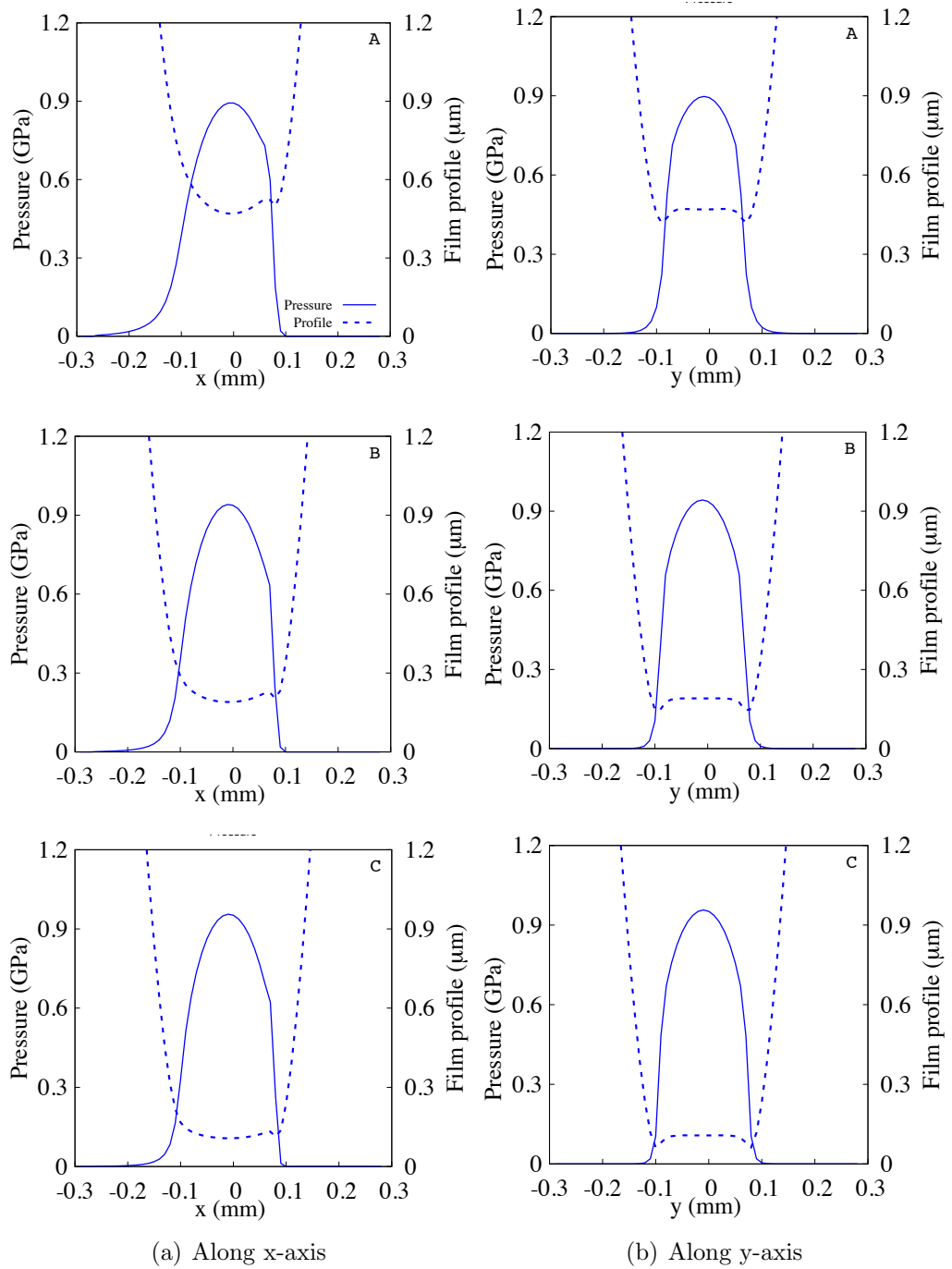


Figure 5.13: Contact pressure distribution and lubricant film profile for point contact lubricated with olive biodiesel

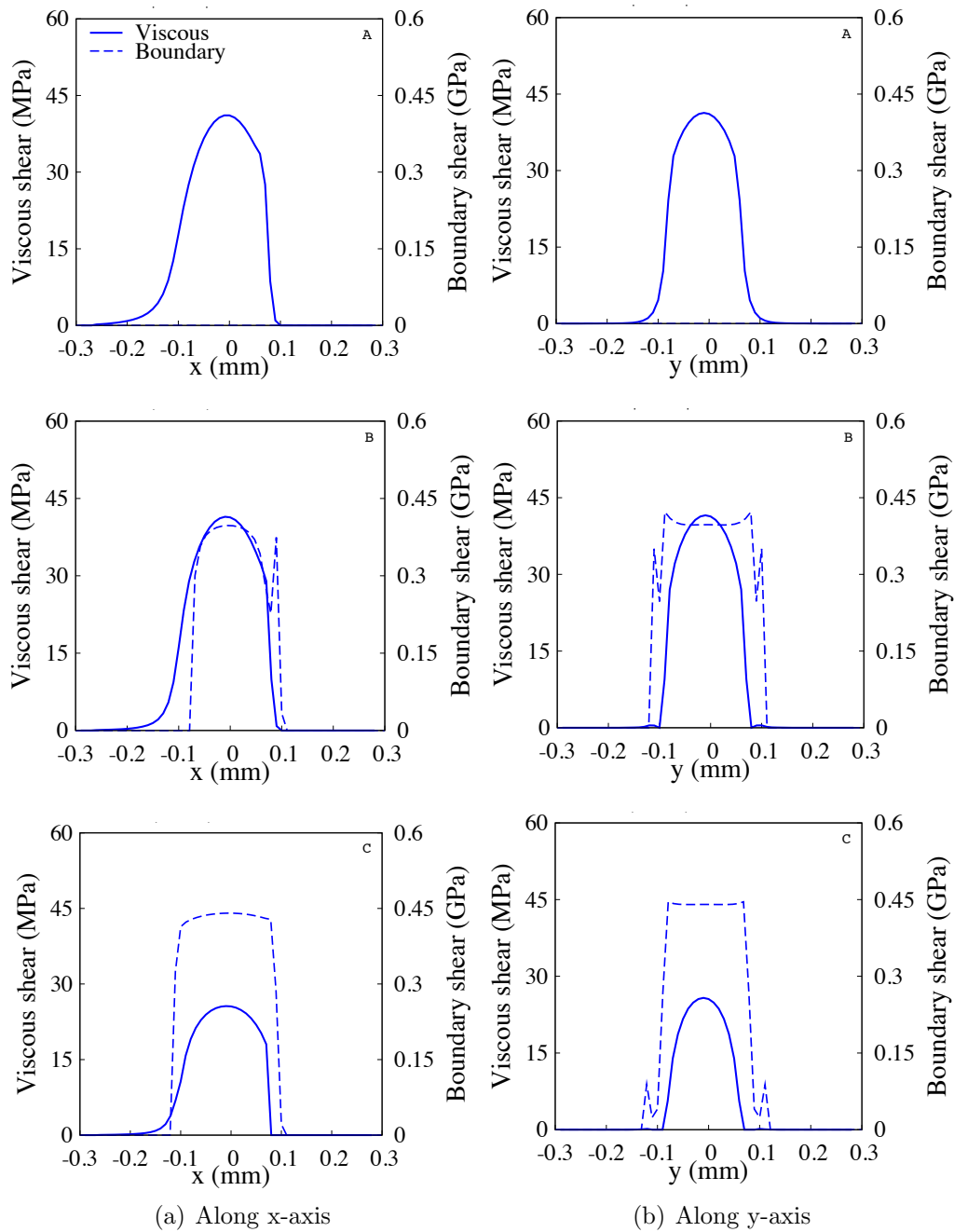


Figure 5.14: Viscous and Boundary shear properties for point contact lubricated with olive biodiesel

In order to relate the term  $\chi$  to the average number of carbon atom and also average number of double bonds of the biodiesels, Figure 5.15 plots the change in the



term  $\chi$  with respect to the product of the average number of carbon atom and the average number of double bonds for the simulated biodiesels. A polynomial curve fitting equation as given below is obtained through this plot as an initial attempt to correlate the modified Reynolds equation to the FAME composition of biodiesels.

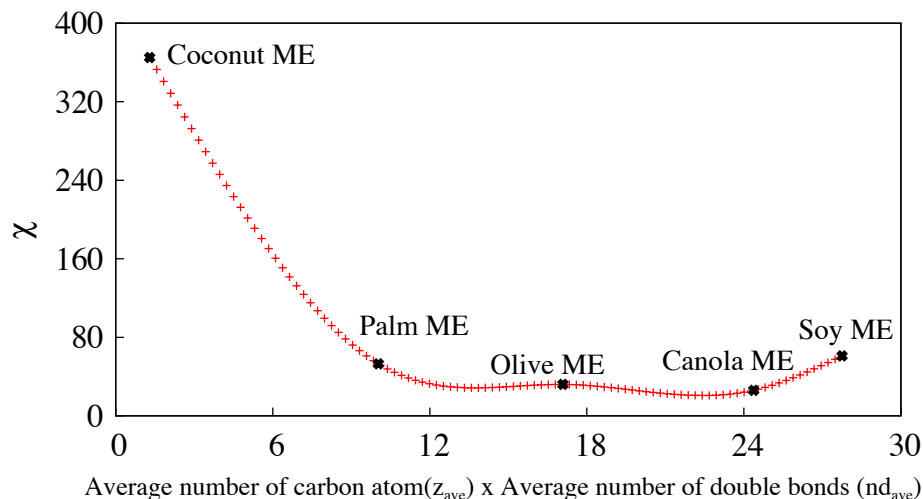


Figure 5.15: Coefficient of  $\chi$

$$\begin{aligned} \chi = & 5.0636e^{-3} \times (\text{ME}_{factor})^4 - 3.5062e^{-1} \times (\text{ME}_{factor})^3 \\ & + 8.9936 \times (\text{ME}_{factor})^2 - 1.0303e^2 \times (\text{ME}_{factor}) + 4.8426^2 \end{aligned} \quad (5.8)$$

where  $\text{ME}_{factor} = z_{ave} \times nd_{ave}$

## 5.4 Verification and validation of modified Reynolds equation

Table 5.7: Average carbon number and average number of double bond for vegetable oil derived biodiesel [111]

Type of biodiesels	$z_{ave}$	$nd_{ave}$
Shortening	17.49	1.120

Table 5.8: Biodiesel rheological properties

Type of biodiesel	Bulk Viscosity $\eta_0$ (mPa.s)	Bulk density $\rho_0$ , (kg/m <sup>3</sup> )
Shortening	4.7894	832.7

To verify and validate the modified Reynolds equation, the  $\chi$  value for shortening biodiesel is computed from the polynomial equation above. The simulation input parameters for shortening biodiesel are summarised in Tables 5.7 and 5.8. Applying the same method in validating canola and oil biodiesel, the lubricant Stribeck curve for shortening biodiesel has been simulated and exhibits good correlation between the measured and computed data as depicted in Figure 5.16. Therefore, it is proved that using this  $\chi$  value, the simulated lubrication Stribeck curve is fitted and matched the measured data for each of the chosen biodiesels. The parameters required to determine the frictional properties along EHL and BL regimes for shortening biodiesel can also be deduced and are given in Table 5.9. Figures 5.17 and 5.18 illustrate the fluid film formation and shear properties for shortening biodiesel.

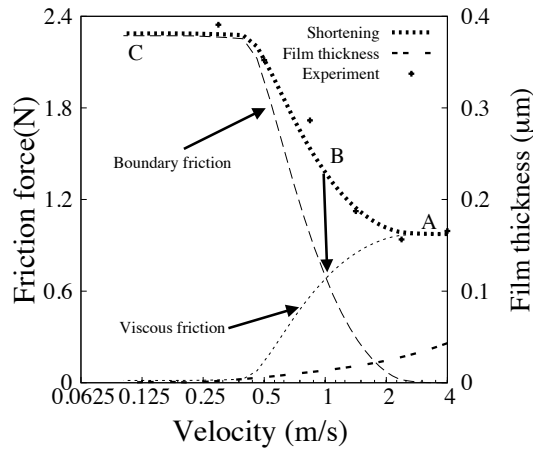


Figure 5.16: Stribeck curve validation

Table 5.9: Predicted values for friction estimation

<b>Type of biodiesels</b>	<b>Pressure coefficient (<math>\kappa</math>)</b>	<b>Limiting shear stress-pressure relation <math>\gamma</math></b>
Shortening	0.1185	0.050

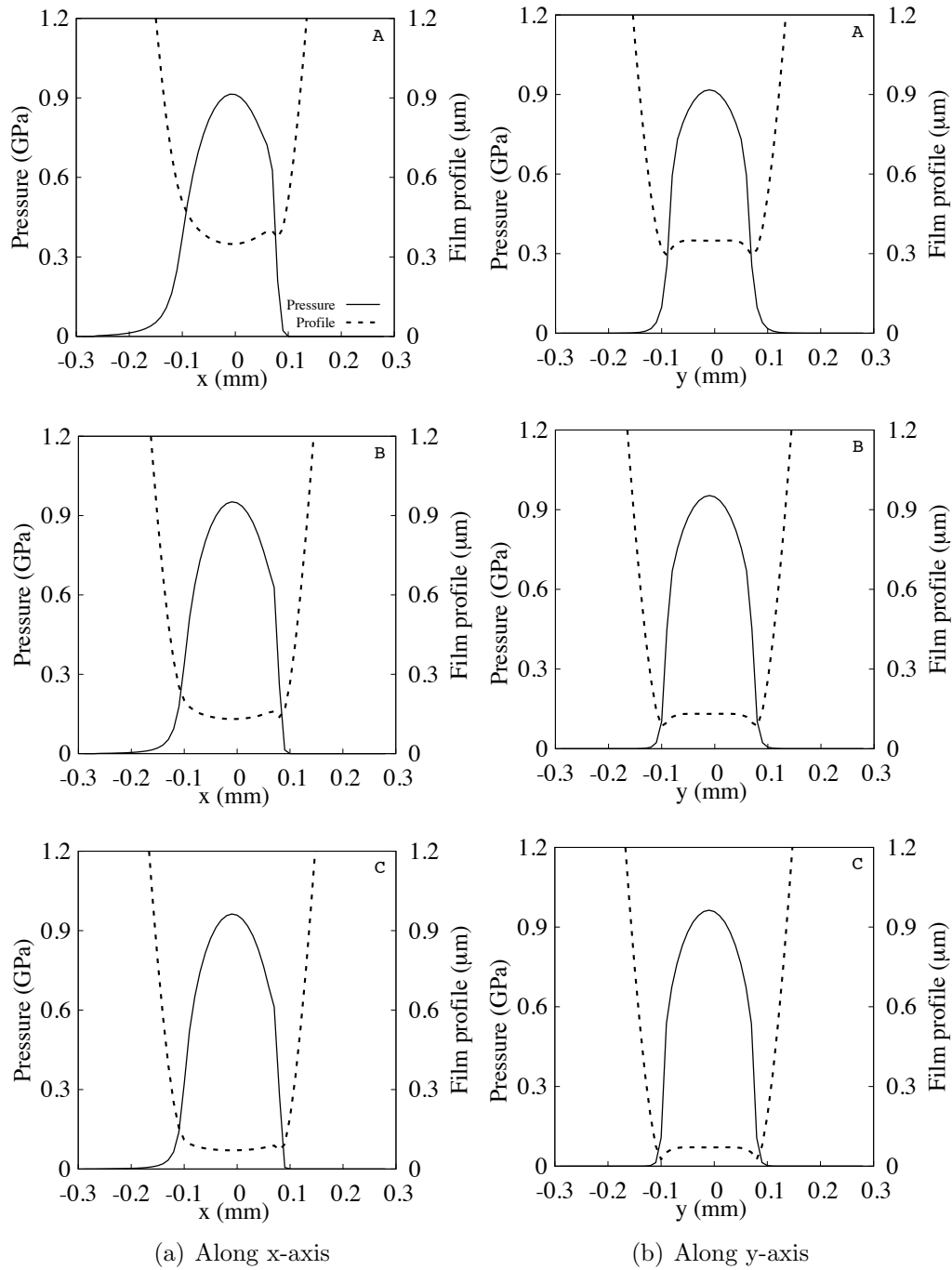


Figure 5.17: Contact pressure distribution and lubricant film profile for point contact lubricated with shortening biodiesel

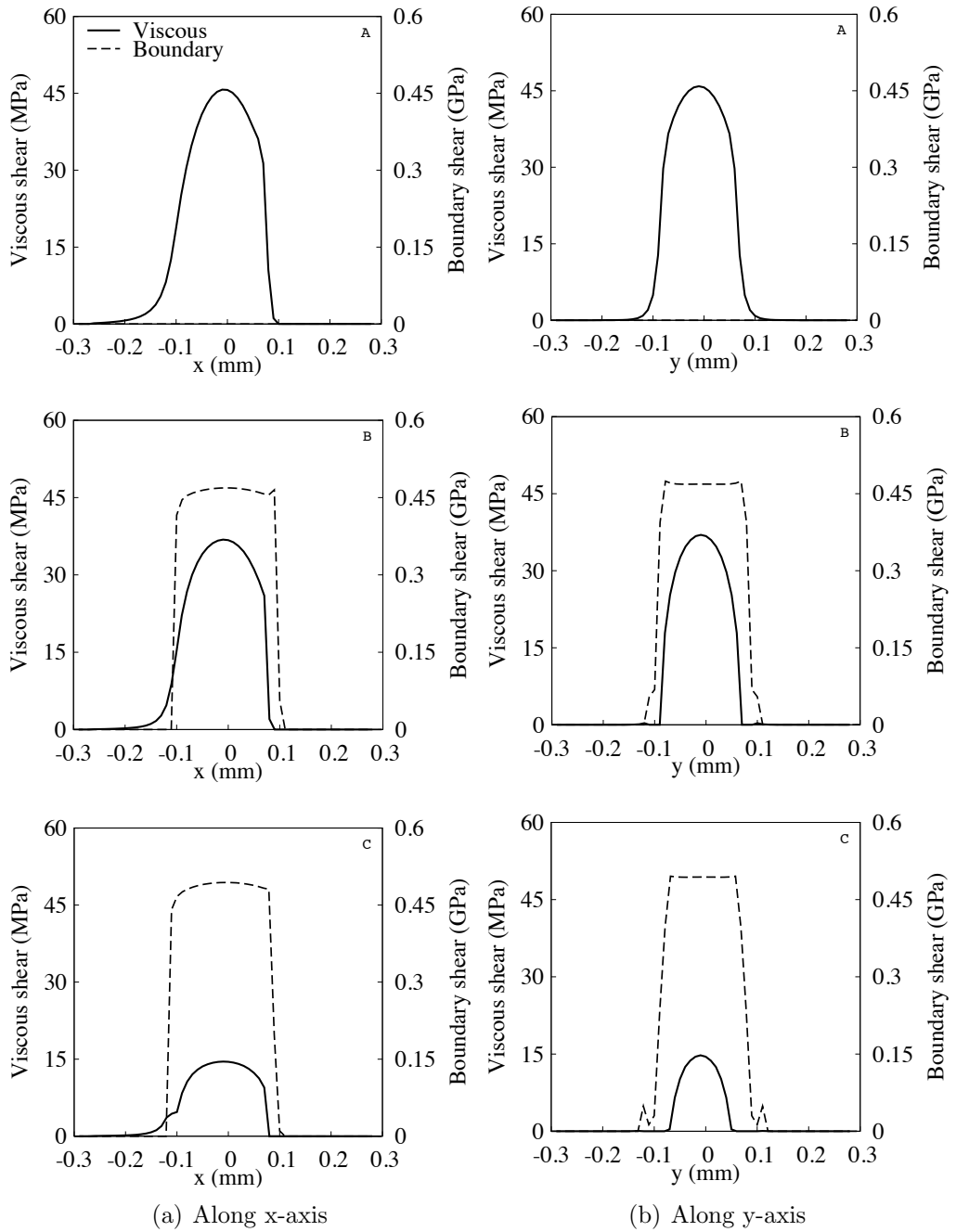


Figure 5.18: Viscous and Boundary shear properties for point contact lubricated with shortening biodiesel

## 5.5 Summary

The validation of the proposed modified Reynolds equation, relating fluid film formation of biodiesels to their FAME compositions, has been discussed in this chapter. Two parameters, namely 1) average number of carbon atom ( $z_{ave}$ ) and 2) average number of double bonds ( $nd_{ave}$ ) for the biodiesels are considered when attempting to introduce the effect of FAME compositions to the classical Reynolds equation. The term  $\chi$  has been introduced to the Reynolds equation to correlate these two parameters. The value for the term  $\chi$  is determined by fitting the simulated lubrication Stribeck curve to the measured data for each of the selected biodiesels. Through this, a polynomial correlation is then obtained for the term  $\chi$  as a function of the product of average number of carbon atoms and average number of double bonds for the biodiesels. The next chapter will conclude the work covered for this study and discuss on possible future work that can be conducted to further improve on the current analysis.

# Chapter 6

## Conclusion and Future work

### 6.1 Conclusion

The study aims to fundamentally understand the tribological properties of biodiesel, to be considered as an alternative lubricant. The emphasis of the study is on investigating the interfacial phenomena governing fluid film formation and determining the mechanisms underlying friction generated by contacts lubricated with biodiesel. In order to achieve the aim, the study is divided into three (3) phases, with each phase having its own objectives.

#### 6.1.1 Phase 1

For phase 1 of the study, two (2) objectives have been identified. For the first objective, *a numerical model for Reynolds solution to predict fluid film formation along a lubricated contact has been developed.*

- A mathematical model is derived using Reynolds equation to predict fluid film formation.
- A lubricant viscosity-pressure coefficient is determined using a free-volume theory, requiring the lubricant-temperature relation as input.
- The simulated lubricant fluid film formation properties are compared to the lubrication regime properties given by Greenwood chart as verification.

- The proposed numerical model is shown to be capable of simulating lubrication properties, corresponding to the visco-elastic or EHL lubrication properties as indicated in the Greenwood chart based on the simulated operating conditions.

For the second of objective of phase 1, *a rough surface contact friction model to predict friction for a lubricated contact along the whole range of lubrication regimes has been formulated.*

- Fluid film formation properties predicted using Reynolds solution is coupled with a rough surface contact model based on Greenwood and Tripp's approach in determining the frictional characteristics of a lubricated point contact.
- The predicted contact pressure distribution and lubricant film profile using Reynolds equation are used to predict viscous and boundary shear properties along the simulated tribological conjunction.
- This model is shown to be capable of simulating the transition of fluid film formation from ML to BL regimes.

### 6.1.2 Phase 2

For phase 2, two research objectives are identified. In the first objective, *frictional properties of lubricated contact of selected SAE grade engine lubricants for the whole range of lubrication regimes has been measured using a tribometer.*

- The friction tests have been carried out using a pin-on-disc tribometer setup.
- Friction forces are measured at various sliding velocities in order to obtain the tribological characteristics of typical lubricants, such as SAE5W40, SAE10W40 and SAE15W40 at different lubrication regimes.
- All tested lubricants exhibit lubricant transition properties that replicate the lubrication Stribeck curve.

The second objective for this phase requires that *friction for a lubricated contact measured using a tribometer be compared with predicted values using the developed mathematical tools.*



- Using the same sliding velocity range, the mathematical model for a lubricated point contact as discussed earlier are used to simulate the conditions of the friction test.
- Along EHL and ML regimes, the lubricant limiting shear stress pressure relation  $\gamma$  is introduced and for boundary lubrication properties along BL regime, pressure coefficient,  $\kappa$  is used.
- Comparing with measured friction data, the non-Newtonian properties are determined by correlating simulation with measured data.
- The results from the mathematical model, coupling Reynolds equation and rough surface contact model, are shown to be capable of estimating the lubrication Stribeck curves that correlate well with the measured properties.

### 6.1.3 Phase 3

Three research objectives are identified for the final phase of the study. For the first objective, *laboratory grade biodiesel from various types of vegetable oil have been derived using transesterification process.*

- Selected vegetable oils are coconut, canola, olive, palm, vegetable shortening and soybean.
- The transesterification process in synthesising fatty acid methyl ester (FAME) from the selected vegetable oil involves the use of potassium hydroxide (KOH) as the catalyst.
- Upon completion of the transesterification process, the kinematic viscosities and densities for the selected biodiesels are measured.

As for the second research objective, *frictional properties of various types of vegetable oil derived biodiesel have been characterised using a tribometer.*

- Based on the feedstocks' melting temperatures, it is shown that the frictional properties of the biodiesels can be divided into two distinct groups: Group I

(feedstocks from winter crops) and Group II (feedstocks from summer crops and hydrogenated vegetable oil).

- For each of the groups, when the ratio of mono-unsaturated to total saturated FAME content decreases, friction forces for both EHL and BL regimes reduce because of improved friction modifier effect, delaying the onset of ML and BL regimes.
- While these properties improve with lower ratio of mono-unsaturated to total saturated FAME content, the load carrying capacity of the lubricated contact along the ML regime reduces, increasing the rupture ability of the fluid film.
- Coconut biodiesel exhibits the better friction modifier effect with the smallest friction force along both the EHL and BL regimes.

Finally, for the third research objective, *shear properties of biodiesel lubricated contact has been simulated using the developed mathematical tools and has been shown to correlate well with measured properties.*

- From the experimental observations, it is realised that frictional properties of contact lubricated with biodiesel is influenced by their FAME compositions.
- The current study proposed a modified Reynolds equation based on two parameters, namely 1) average number of carbon atom ( $z_{ave}$ ) and 2) average number of double bonds ( $nd_{ave}$ ) for biodiesels.
- The term  $\chi$  is also introduced to the modified Reynolds equation to correlate these two parameters.
- The value for the term  $\chi$  is shown to be able to be determined by fitting the simulated lubrication Stribeck curve to the measured data for each of the selected biodiesels.

## 6.2 Main contribution to knowledge

- A mathematical tool has been developed to predict friction values for contacts lubricated using typical lubricants (e.g. SAE5W40, SAE10W40 and SAE15W40) using a free-volume theory in determining lubricant viscosity-pressure relation.
- A modified Reynolds equation, introducing the term  $\chi$  to correlate average number of carbon atom and average number of double bonds for biodiesels, is proposed and used to predict frictional properties of biodiesel for the whole range of lubrication regimes.

## 6.3 Future work

In order to promote green technology, one of the measures proposed by the Malaysian government is to increase the amount of biodiesel added to conventional petro-diesel by volume from 7% (B7) to 10% (B10) [113]. Investigations showed that engine lubricant dilution will be more severe when biodiesel fuel is used since this fuel tends to concentrate in the lubricant [114, 115] because of its higher boiling point than petro-diesel fuel [116]. It is found that post-injected petro-diesel fuel blended with 20% biodiesel (B20) could lead to as much as 40% methyl ester accumulation on the cylinder walls [117].

With good lubrication properties, biodiesel dilution of engine lubricant is expected to improve the tribological performance along the piston ring-liner contact. However, the introduction of biodiesel blended with petro-diesel fuel raised concerns from major automotive manufacturers with regards to the possible tribological impact on the engine lubricant when diluted by this alternative fuel. More importantly, it is also suggested that for petro-diesel fuel blended with 10% biodiesel (B10), a dilution level beyond 50% threshold could lead to premature engine wear failure if engine lubricant is not changed more frequently [117].

Limited work has been reported in literature on the effect of biodiesel dilution on the lubrication properties of engine lubricants. Among those include the work by Fang *et al.*, who investigated the wear characteristics of the biodiesel contaminated engine lubricant using HFRR and four ball tester [118]. They concluded that biodiesel can

lead to increased engine wear. This is a result of the methyl ester molecules diluting the engine lubricant, forming complexes with the anti-wear additives, such as zinc-di-alkyldithiophosphate (ZDDP), which affects such additives from forming a protective coating on the metal surfaces [119].

In view of the intended increased use of biodiesel in petro-diesel fuel, the essence learnt from this study serves as a fundamental platform in order to better understand the frictional implications when biodiesel dilutes typical lubricants. For future work, it would be interesting to investigate and measure the effect of tribological properties of biodiesel diluted lubricants. A modified model will be required and extended to consider the interactions between FAME and lubricant additives such as ZDDP.

# References

- [1] “Exxon mobile: The outlook for energy: a view to 2040,” <https://Cdn.exxonmobil.com/Media/Global/Files/Outlook-for-Energy/2016/2016-Outlook-for-Energy.pdf>, pp. 1–80, 2016.
- [2] “International energy agency : World energy outlook 2015,” <https://www.iea.org/publications/freepublications/publication/WEO2015.pdf>, 2015.
- [3] A. E. K. Holmberg, P. Andersson, “Global energy consumption due to friction in passenger cars,” *Tribology International* 47:221–234, 2012.
- [4] W. Chong, J.-H. Ng, S. Rajoo, and C. Chong, “Passenger transportation sector gasoline consumption due to friction in southeast asian countries,” *Energy Conversion and Management*, vol. 158, pp. 346 – 358, 2018.
- [5] “Grand view research: Lubricants market analysis by product, industrial (process oils, general industrial oils, metal working fluids, industrial engine oils), automotive (heavy-duty engine oils, hydraulic and transmission fluid, gear oil, passenger vehicle engine oils, automatic transmission fluid, gear oil) and segment forecasts to 2022,” <https://www.grandviewresearch.com/industry-analysis/lubricants-market>, 2014.
- [6] V. W. Wong and S. C. Tung, “Overview of automotive engine friction and reduction trends—effects of surface, material, and lubricant-additive technologies,” *Friction*, vol. 4, no. 1, pp. 1–28, 2016.

- [7] P. Jost, “Green tribology,” in *A Footprint Where Economics and Environment Meet. Address to the Fourth World Tribology Congress, Kyoto, Japan*, vol. 5, 2009.
- [8] M. Nosonovsky and B. Bhushan, “Green tribology: principles, research areas and challenges,” *Philosophical Transactions of Royal Society A*, vol. 368, pp. pp. 4677–4694, 2010.
- [9] S. Hamdan, W. Chong, J.-H. Ng, C. Chong, and S. Rajoo, “A study of the tribological impact of biodiesel dilution on engine lubricant properties,” *Process Safety and Environmental Protection*, vol. 112, pp. 288–297, 2017.
- [10] M. Andrae, H. Fang, and K. Bhandary, “Biodiesel and fuel dilution of engine oil,” tech. rep., SAE Technical Paper, 2007.
- [11] E. Sendzikiene, V. Makareviciene, P. Janulis, and D. Makareviciute, “Biodegradability of biodiesel fuel of animal and vegetable origin,” *European Journal of Lipid Science and Technology*, vol. 109, no. 5, pp. 493–497, 2007.
- [12] K. S. Tyson and R. L. McCormick, “Biodiesel handling and use guidelines,” *National Renewable Energy Laboratory Golden, CO*, 2006.
- [13] H. Rahnejat, S. Balakrishnan, P. King, and S. Howell-Smith, “In-cylinder friction reduction using a surface finish optimization technique,” *Proceedings of the Institution of Mechanical Engineers, Part D: Journal of Automobile Engineering*, vol. 220, no. 9, pp. 1309–1318, 2006.
- [14] O. M. Ali, R. Mamat, N. R. Abdullah, and A. A. Abdullah, “Analysis of blended fuel properties and engine performance with palm biodiesel–diesel blended fuel,” *Renewable Energy*, vol. 86, pp. 59–67, 2016.
- [15] R. Gohar and H. Rahnejat, *Fundamentals of tribology*. Imperial College Press, London, 2008.
- [16] O. Reynolds, “On the theory of lubrication and its application to mr. beauchamp tower’s experiments, including an experimental determination of the viscosity of olive oil.,” *Proceedings of the Royal Society of London*, vol. 40, no. 242-245, pp. 191–203, 1886.

- [17] B. Jakobsson and L. Floberg, *The finite journal bearing, considering vaporization*. Gumperts Förlag, 1957.
- [18] K. O. Olsson, *Cavitation in dynamically loaded bearings*. Scandinavian Univ. Books, 1965.
- [19] W. W. F. Chong, M. Teodorescu, and N. D. Vaughan, “Cavitation induced starvation for piston-ring/liner tribological conjunction,” *Tribology International*, vol. 44, no. 4, pp. 483–497, 2011.
- [20] D. Zhu and Q. J. Wang, “Elastohydrodynamic lubrication: a gateway to interfacial mechanics-review and prospect,” *Journal of Tribology*, vol. 133, no. 4, p. 041001, 2011.
- [21] A. Grubin, “Fundamentals of the hydrodynamic theory of lubrication of heavily loaded cylindrical surfaces,” *Investigation of the Contact Machine Components*, vol. 2, 1949.
- [22] A. Ertel, “Hydrodynamic lubrication based on new principles,” *Akad. Nauk. SSSR, Prikladnaya Matematika i Mekhanika*, vol. 3, no. 2, pp. 41–52, 1939.
- [23] A. Petrusevich, “Fundamental conclusions from the contact -hydrodynamics theory of lubrication,” *Izv. Akad. nauk. SSR Otd. Tekh. Nauk 2 pp 209-233*, 1951.
- [24] B. J. Hamrock, “Film thickness for different regimes of fluid-film lubrication,” *NASA Technical Memorandum 81550*, 1980.
- [25] M. Esfahanian and B. Hamrock, “Fluid-film lubrication regimes revisited,” *Tribology Transactions*, vol. 34, no. 4, pp. 628–632, 1991.
- [26] D. Dowson and G. Higginson, “A numerical solution to the elasto-hydrodynamic problem,” *Journal of Mechanical Engineering Science*, vol. 1, no. 1, pp. 6–15, 1959.
- [27] D. Dowson, “New roller-bearing lubrication formula,” *Engineering Lond.*, vol. 192, p. 158, 1961.

- [28] D. Dowson and G. R. Higginson, *Elasto-hydrodynamic lubrication: the fundamentals of roller and gear lubrication*, vol. 23. Pergamon Press, 1966.
- [29] M. Kushwaha and H. Rahnejat, “Transient elastohydrodynamic lubrication of finite line conjunction of cam to follower concentrated contact,” *Journal of Physics D: Applied Physics*, vol. 35, no. 21, p. 2872, 2002.
- [30] M. Teodorescu, M. Kushwaha, H. Rahnejat, and S. Rothberg, “Multi-physics analysis of valve train systems: from system level to microscale interactions,” *Proceedings of the Institution of Mechanical Engineers, Part K: Journal of Multi-body Dynamics*, vol. 221, no. 3, pp. 349–361, 2007.
- [31] M. A. Malik, S. A. Qasim, U. F. Chaudhri, and R. A. Mufti, “Non-newtonian elastohydrodynamic lubrication fluid flow modeling of piston skirts considering low speed effects in initial engine start up,” *ASME 2010 International Mechanical Engineering Congress and Exposition*, pp. 547–556, 2010.
- [32] M. De la Cruz, W. Chong, M. Teodorescu, S. Theodossiades, and H. Rahnejat, “Transient mixed thermo-elastohydrodynamic lubrication in multi-speed transmissions,” *Tribology international*, vol. 49, pp. 17–29, 2012.
- [33] M. Masjedi and M. Khonsari, “Theoretical and experimental investigation of traction coefficient in line-contact ehl of rough surfaces,” *Tribology International*, vol. 70, pp. 179–189, 2014.
- [34] Y.-Z. Hu and D. Zhu, “A full numerical solution to the mixed lubrication in point contacts,” *ASME J. Tribol*, vol. 122, no. 1, pp. 1–9, 2000.
- [35] S. Bair and W. Winer, “A rheological model for elastohydrodynamic contacts based on primary laboratory data,” *ASME, Transactions, Journal of Lubrication Technology*, vol. 101, pp. 258–264, 1979.
- [36] D. Zhu and Y.-Z. Hu, “A computer program package for the prediction of ehl and mixed lubrication characteristics, friction, subsurface stresses and flash temperatures based on measured 3-d surface roughness,” *Tribology Transactions*, vol. 44, no. 3, pp. 383–390, 2001.



- [37] D. Zhu, J. Wang, and Q. J. Wang, "On the stribek curves for lubricated counter-formal contacts of rough surfaces," *Journal of Tribology*, vol. 137, no. 2, p. 021501, 2015.
- [38] M. Teodorescu, D. Taraza, N. A. Henein, and W. Bryzik, "Simplified elasto-hydrodynamic friction model of the cam-tappet contact," *SAE Technical Paper*, 2003.
- [39] D. Dowson, G. Higginson, and J. Archard, "Elastohydrodynamic lubrication," *SI ed. Pergamon Press, Oxford*, 1977.
- [40] J.A.Greenwood and J.H.Tripp, "The contact of two nominally flat rough surfaces," *Proceedings of the institution of mechanical engineers*, vol. 185, no. 1, pp. 625–633, 1970.
- [41] C.R.Evans and K. K.L.Johnson, "The rheological properties of elasto-hydrodynamic lubricants," *Proceedings of the Institution of Mechanical Engineers, Part C: Journal of Mechanical Engineering Science*, vol. 200, no. 5, pp. 303–312, 1986.
- [42] D.Vijayaraghavan and T. T.G.Keith Jr, "Development and evaluation of a cavitation algorithm," *Tribology Transactions*, vol. 32, no. 2, pp. 225–233, 1989.
- [43] W. W. F. Chong, M. Teodorescu, and H. Rahnejat, "Mixed thermo-elastohydrodynamic cam-tappet power loss in low-speed emission cycles," *International Journal of Engine Research*, vol. 15, no. 2, pp. 153–164, 2014.
- [44] W. Chong and M. De la Cruz, "Elastoplastic contact of rough surfaces: a line contact model for boundary regime of lubrication," *Meccanica*, vol. 49, no. 5, pp. 1177–1191, 2014.
- [45] R. L. Jackson and I. Green, "A finite element study of elasto-plastic hemispherical contact against a rigid flat," *Transactions of the ASME-F-Journal of Tribology*, vol. 127, no. 2, pp. 343–354, 2005.
- [46] J. Archard, "Elastic deformation and the laws of friction," in *Proceedings of the Royal Society of London A: Mathematical, Physical and Engineering Sciences*, vol. 243, pp. 190–205, The Royal Society, 1957.

- [47] J. Greenwood and J. P. Williamson, "Contact of nominally flat surfaces," in *Proceedings of the Royal Society of London A: Mathematical, Physical and Engineering Sciences*, vol. 295, pp. 300–319, The Royal Society, 1966.
- [48] J. Greenwood and J. Tripp, "The contact of two nominally flat rough surfaces," *Proceedings of the institution of mechanical engineers*, vol. 185, no. 1, pp. 625–633, 1970.
- [49] J. Greenwood, "A unified theory of surface roughness," in *Proceedings of the Royal Society of London A: Mathematical, Physical and Engineering Sciences*, vol. 393, pp. 133–157, The Royal Society, 1984.
- [50] P. R. Nayak, "Random process model of rough surfaces," *Journal of Lubrication Technology*, vol. 93, no. 3, pp. 398–407, 1971.
- [51] R. S. Sayles and T. R. Thomas, "Surface topography as a nonstationary random process," *Nature*, vol. 271, no. 5644, pp. 431–434, 1978.
- [52] T. Thomas, "Defining the microtopography of surfaces in thermal contact," *Wear*, vol. 79, no. 1, pp. 73–82, 1982.
- [53] A. Majumdar and C. Tien, "Fractal characterization and simulation of rough surfaces," *Wear*, vol. 136, no. 2, pp. 313–327, 1990.
- [54] W. Yan and K. Komvopoulos, "Contact analysis of elastic-plastic fractal surfaces," *Journal of applied physics*, vol. 84, no. 7, pp. 3617–3624, 1998.
- [55] R. L. Jackson and J. L. Streator, "A multi-scale model for contact between rough surfaces," *Wear*, vol. 261, no. 11, pp. 1337–1347, 2006.
- [56] K. Johnson, J. Greenwood, and S. Poon, "A simple theory of asperity contact in elasto-hydro-dynamic lubrication," *Wear*, vol. 19, no. 1, pp. 91–108, 1972.
- [57] B. R. Moser, "Biodiesel production, properties, and feedstocks," *In Vitro Cellular & Developmental Biology-Plant*, vol. 45, no. 3, pp. 229–266, 2009.
- [58] D. P. Geller and J. W. Goodrum, "Effects of specific fatty acid methyl esters on diesel fuel lubricity," *Fuel*, vol. 83, no. 17, pp. 2351–2356, 2004.

- [59] J. W. Goodrum and D. P. Geller, "Influence of fatty acid methyl esters from hydroxylated vegetable oils on diesel fuel lubricity," *Bioresource Technology*, vol. 96, no. 7, pp. 851–855, 2005.
- [60] A. Nicolau, C. V. Lutckmeier, D. Samios, M. Gutterres, and C. M. Piatnick, "The relation between lubricity and electrical properties of low sulfur diesel and diesel/biodiesel blends," *Fuel*, vol. 117, pp. 26–32, 2014.
- [61] M. Hazrat, M. Rasul, and M. M. K. Khan, "Lubricity improvement of the ultra-low sulfur diesel fuel with the biodiesel," *Energy Procedia*, vol. 75, pp. 111–117, 2015.
- [62] G. Knothe and K. R. Steidley, "Lubricity of components of biodiesel and petrodiesel. the origin of biodiesel lubricity," *Energy & fuels*, vol. 19, no. 3, pp. 1192–1200, 2005.
- [63] M. M. Maru, R. M. Trommer, K. F. Cavalcanti, E. S. Figueiredo, R. F. Silva, and C. A. Achete, "The stribeck curve as a suitable characterization method of the lubricity of biodiesel and diesel blends," *Energy*, vol. 69, pp. 673–681, 2014.
- [64] Z. M. J. D. D. Jalali-Vahid, H. Rahnejat and D. Dowson, "Transient analysis of isothermal elastohydrodynamic circular point contact," *ImechE, Loughborough university institutional repository*, 2001.
- [65] D. Vijayaraghavan and T. Keith Jr, "Development and evaluation of a cavitation algorithm," *Tribology Transactions*, vol. 32, no. 2, pp. 225–233, 1989.
- [66] H. G. Elrod, "A cavitation algorithm," *ASME J. Lubr. Technol.*, vol. 103, p. 350, 1981.
- [67] M. Fesanghary and M. Khonsari, "A modification of the switch function in the elrod cavitation algorithm," *Journal of Tribology*, vol. 133, no. 2, p. 024501, 2011.
- [68] N. Patir and H. Cheng, "An average flow model for determining effects of three-dimensional roughness on partial hydrodynamic lubrication," *Journal of Lubrication Technology*, vol. 100, no. 1, pp. 12–17, 1978.

- [69] F. Sahlin, A. Almqvist, R. Larsson, and S. Glavatskih, “Rough surface flow factors in full film lubrication based on a homogenization technique,” *Tribology International*, vol. 40, no. 7, pp. 1025–1034, 2007.
- [70] R. Rahmani, I. Mirzaee, A. Shirvani, and H. Shirvani, “An analytical approach for analysis and optimisation of slider bearings with infinite width parallel textures,” *Tribology International*, vol. 43, no. 8, pp. 1551–1565, 2010.
- [71] N. Morris, R. Rahmani, H. Rahnejat, P. King, and B. Fitzsimons, “The influence of piston ring geometry and topography on friction,” *Proceedings of the Institution of Mechanical Engineers, Part J: Journal of Engineering Tribology*, vol. 227, no. 2, pp. 141–153, 2013.
- [72] G. Bayada, S. Martin, and C. Vazquez, “Two-scale homogenization of a hydrodynamic elrod–adams model,” *Asymptotic Analysis*, vol. 44, no. 1, 2, pp. 75–110, 2005.
- [73] H. Elrod and M. Adams, “A computer program for cavitation and starvation problems,” *Cavitation and related phenomena in lubrication*, vol. 103, pp. 37–41, 1974.
- [74] A. Burgdorfer, “The influence of the molecular mean free path on the performance of hydrodynamic gas lubricated bearings,” *ASME Journal of basic Engineering*, vol. 81, pp. 94–100, 1959.
- [75] S. Fukui and R. Kaneko, “Analysis of ultra-thin gas film lubrication based on linearized boltzmann equation: first report-derivation of a generalized lubrication equation including thermal creep flow,” *Journal of Tribology*, vol. 110, no. 2, pp. 253–261, 1988.
- [76] C. C. Hwang, R. F. Fung, R. F. Yang, C. I. Weng, and W. L. Li, “A new modified reynolds equation for ultrathin film gas lubrication,” *IEEE Transactions on Magnetics*, vol. 32, no. 2, pp. 344–347, 1996.
- [77] T. Veijola, H. Kuisma, and J. Lahdenperä, “The influence of gas-surface interaction on gas-film damping in a silicon accelerometer,” *Sensors and Actuators A: Physical*, vol. 66, no. 1, pp. 83–92, 1998.

- [78] N. D. Stevanović and V. D. Djordjević, “The exact analytical solution for the gas lubricated bearing in the slip and continuum flow regime,” *Publications de l’Institut Mathématique*, vol. 91, no. 105, pp. 83–93, 2012.
- [79] P. Bahukudumbi and A. Beskok, “A phenomenological lubrication model for the entire knudsen regime,” *Journal of Micromechanics and Microengineering*, vol. 13, no. 6, p. 873, 2003.
- [80] R. W. Armentrout, M. He, T. Haykin, and A. E. Reed, “Analysis of turbulence and convective inertia in a water-lubricated tilting-pad journal bearing using conventional and cfd approaches,” *Tribology Transactions*, pp. 1–19, 2016.
- [81] M. G. C. De Neves, M. A. N. Da Cunha, N. M. Y. Filho, P. L. Rodrigues, E. A. Batista, T. A. Prado, and M. H. Naka, “Design and fabrication of a linear reciprocating tribometer using sensors with strain-gages,” *22nd International Congress of Mechanical Engineering (COBEM 2013)*, 2013.
- [82] W. Piekoszewski, M. Szczerek, and W. Tuszynski, “The action of lubricants under extreme pressure conditions in a modified four-ball tester,” *Wear*, vol. 249, no. 3, pp. 188–193, 2001.
- [83] B. Briscoe and T. Stolarski, “Wear of polymers in the pin-on-disk configuration,” *In Proceedings of the International Symposium on Polymer Wear and Its Control (Lee, L. H.), St Louis, Missouri, (American Chemical Society, New York), 8-13 April 1984.*
- [84] R. J. Covert, R. Ott, and D. N. Ku, “Friction characteristics of a potential articular cartilage biomaterial,” *Wear*, vol. 255, no. 7, pp. 1064–1068, 2003.
- [85] K. Bonny, P. De Baets, J. Vleugels, S. Huang, O. Van der Biest, and B. Lauwers, “Impact of cr 3 c 2/vc addition on the dry sliding friction and wear response of wc-co cemented carbides,” *Wear*, vol. 267, no. 9, pp. 1642–1652, 2009.
- [86] S. T. Lesniewski, “The effect of ball hardness on four ball wear test result,” *Wear* 264 662-670, 2008.

- [87] H. Masjuki and M. Maleque, "Investigation of the anti-wear characteristics of palm oil methyl ester using a four-ball tribometer test," *Wear*, vol. 206, no. 1, pp. 179–186, 1997.
- [88] P. L. Morgado, J. E. Otero, J. S.-P. Lejarraga, J. M. Sanz, A. D. Lantada, J. Munoz-Guijosa, H. L. Yustos, P. L. Wiña, and J. M. García, "Models for predicting friction coefficient and parameters with influence in elastohydrodynamic lubrication," *Proceedings of the Institution of Mechanical Engineers, Part J: Journal of Engineering Tribology*, vol. 223, no. 7, pp. 949–958, 2009.
- [89] V. Pejaković, A. Igartua, and M. Kalin, "Frictional behaviour of imidazolium sulfate ionic liquid additives under mixed slide to roll conditions: part 2 influence of concentration and chemical composition of ionic liquid additive," *Lubrication Science*, vol. 27, no. 8, pp. 489–503, 2015.
- [90] C. Hooke, "A review of the paper -a numerical solution to the elastohydrodynamic problem by D. Dowson and GR Higginson," *Proceedings of the Institution of Mechanical Engineers, Part C: Journal of Mechanical Engineering Science*, vol. 223, no. 1, pp. 49–63, 2009.
- [91] E. Höglund, "Influence of lubricant properties on elastohydrodynamic lubrication," *Wear*, vol. 232, no. 2, pp. 176–184, 1999.
- [92] C. J. A. Roelands, *Correlation aspects of viscosity- temperature-pressure relationship of lubricating oils*. PhD thesis, Delft University of Technology, 1996.
- [93] M. Teodorescu, D. Taraza, N. A. Henein, and W. Bryzik, "Simplified elastohydrodynamic friction model of the cam-tappet contact," *SAE Technical Paper*, 2003.
- [94] H. Spikes, "Sixty years of ehl," *Lubrication Science*, vol. 18, no. 4, pp. 265–291, 2006.
- [95] W. Habchi, S. Bair, and P. Vergne, "On friction regimes in quantitative elastohydrodynamics," *Tribology International*, vol. 58, pp. 107–117, 2013.
- [96] R. Larsson, "Transient non-newtonian elastohydrodynamic lubrication analysis of an involute spur gear," *Wear*, vol. 207, no. 1, pp. 67–73, 1997.

- [97] J. McBride, “The loaded surface profile: a new technique for the investigation of contact surfaces,” *Institute of Electronics, Information and Communication Engineers*, 2006.
- [98] C. Wu, E. Klaus, and J. Duda, “Development of a method for the prediction of pressure-viscosity coefficients of lubricating oils based on free-volume theory,” *ASME J. Tribol*, vol. 111, no. 1, pp. 121–128, 1989.
- [99] S. C. Tung and M. L. McMillan, “Automotive tribology overview of current advances and challenges for the future,” *Tribology International*, vol. 37, no. 7, pp. 517–536, 2004.
- [100] E. Höglund, “Influence of lubricant properties on elastohydrodynamic lubrication,” *Wear*, vol. 232, no. 2, pp. 176–184, 1999.
- [101] A. Kovalchenko, O. Ajayi, A. Erdemir, G. Fenske, and I. Etsion, “The effect of laser surface texturing on transitions in lubrication regimes during unidirectional sliding contact,” *Tribology International*, vol. 38, no. 3, pp. 219–225, 2005.
- [102] “Park XE7 Atomic Force Microscope,” <http://www.parksystems.com/index.php/products/sample-afm/park-xe7/overview>, 2018.
- [103] C. Buenviaje, S.-R. Ge, M. Rafailovich, and R. Overney, “Atomic force microscopy calibration methods for lateral force, elasticity, and viscosity,” *MRS Online Proceedings Library Archive*, vol. 522, 1998.
- [104] “Park Probe Store Contact Mode,” <http://www.parksystems.com/index.php/service/probe-store/348-contact-mode>, 2018.
- [105] C. Evans and K. Johnson, “The rheological properties of elastohydrodynamic lubricants,” *Proceedings of the Institution of Mechanical Engineers, Part C: Journal of Mechanical Engineering Science*, vol. 200, no. 5, pp. 303–312, 1986.
- [106] L. Meher, D. V. Sagar, and S. Naik, “Technical aspects of biodiesel production by transesterification-a review,” *Renewable and sustainable energy reviews*, vol. 10, no. 3, pp. 248–268, 2006.

- [107] H. Fukuda, A. Kondo, and H. Noda, “Biodiesel fuel production by transesterification of oils,” *Journal of bioscience and bioengineering*, vol. 92, no. 5, pp. 405–416, 2001.
- [108] C. A. Allen, K. Watts, R. Ackman, and M. Pegg, “Predicting the viscosity of biodiesel fuels from their fatty acid ester composition,” *Fuel*, vol. 78, no. 11, pp. 1319–1326, 1999.
- [109] M. J. Ramos, C. M. Fernández, A. Casas, L. Rodríguez, and Á. Pérez, “Influence of fatty acid composition of raw materials on biodiesel properties,” *Bioresource technology*, vol. 100, no. 1, pp. 261–268, 2009.
- [110] K. Wadumesthrige, M. Ara, S. O. Salley, and K. S. Ng, “Investigation of lubricity characteristics of biodiesel in petroleum and synthetic fuel,” *Energy & Fuels*, vol. 23, no. 4, pp. 2229–2234, 2009.
- [111] T. Chum-in, K. Sudaprasert, S. Phankosol, S. Lilitchan, K. Aryusuk, and K. Krisnangkura, “Gibbs energy additivity approaches to qspr in modeling of high pressure dynamic viscosity of fame and biodiesel,” *Journal of Molecular Liquids*, vol. 223, pp. 1006–1012, 2016.
- [112] S. Phankosol, K. Sudaprasert, S. Lilitchan, K. Aryusuk, and K. Krisnangkura, “Estimation of density of biodiesel,” *Energy & Fuels*, vol. 28, no. 7, pp. 4633–4641, 2014.
- [113] E. M. Plan, “Pursuing green growth for sustainability and resilience,” [www.capitalmarketsmalaysia.com/wp-content/uploads/2016/09/Chapter6-MalaysiaPlan.pdf](http://www.capitalmarketsmalaysia.com/wp-content/uploads/2016/09/Chapter6-MalaysiaPlan.pdf), pp. 6/1– 6/30, 2016.
- [114] M. J. Thornton, T. L. Alleman, J. Luecke, and R. L. McCormick, “Impacts of biodiesel fuel blends oil dilution on light-duty diesel engine operation,” *SAE International Journal of Fuels and Lubricants*, vol. 2, no. 2009-01-1790, pp. 781–788, 2009.
- [115] M. Morcos, G. Parsons, F. Lauterwasser, M. Boons, and W. Hartgers, “Detection methods for accurate measurements of the FAME biodiesel content in used crankcase engine oil,” *SAE Technical Paper*, 2009.



- [116] M. Andreae, H. Fang, and K. Bhandary, "Biodiesel and fuel dilution of engine oil," *SAE Technical Paper*, 2007.
- [117] R. Kotrba, "Understanding the post-injection problem," *Biodiesel Magazine*, vol. 5, no. 5, 2008.
- [118] H. Fang, S. Whitacre, E. Yamaguchi, and M. Boons, "Biodiesel impact on wear protection of engine oils," *SAE Technical Paper*, 2007.
- [119] H. Fang, T. Alleman, and R. McCormick, "Quantification of biodiesel content in fuels and lubricants by ftir and nmr spectroscopy," *SAE Technical Paper*, 2006.
- [120] W. W. F. Chong, *Adhesive and molecular friction in tribological conjunctions*. PhD thesis, Cranfield University, 2012.

# Appendix A

## Derivation of two-dimensional Reynolds solution; point contact problem

Finite difference method is used, where the equation is separate into two main parameters known as Poiseuille flow and Couette flow. Then, it is being simplified using the Newton-raphson method as discussed in line contact problem.

$$\frac{\partial}{\partial x} \left[ \frac{\rho h^3}{12\eta} \frac{\partial p}{\partial x} \right] + \frac{\partial}{\partial y} \left[ \frac{\rho h^3}{12\eta} \frac{\partial p}{\partial y} \right] = 12 \left\{ \frac{\partial}{\partial x} \left[ \frac{\rho h(u_A + u_B)}{2} \right] + \frac{\partial}{\partial y} \left[ \frac{\rho h(v_A + v_B)}{2} \right] + \frac{\partial \rho h}{\partial t} \right\} \quad (\text{A.1})$$

where A and B are subscripts denoting the top and bottom bounding bodies respectively.

$$u = \frac{(u_A + u_B)}{2}, v = \frac{(v_A + v_B)}{2}$$

$$U = \frac{u}{u_{av}}, V = \frac{v}{v_{av}}$$

where  $U$  is  $U$  is the speed of entraining motion of the lubricant into the conjunction and  $V$  is the speed of any side-leakage of lubricant out of the contact area

## A.1 Dimensionless parameter for 2D point contact:

Using Jalali *et al.* [64] and Chong [120] approaches, equation A.2 must first be non-dimensionalized before being calculated using finite-difference method. The non-dimensional parameters are shown in Table A.1. Assuming that  $\bar{\rho} \neq f(t)$ . Reynolds equation becomes :

$$\frac{\partial}{\partial x} \left[ \frac{\rho h^3}{\eta} \frac{\partial p}{\partial x} \right] + \frac{\partial}{\partial y} \left[ \frac{\rho h^3}{\eta} \frac{\partial p}{\partial y} \right] = 12 \left[ u_{av} \frac{\partial(\rho h U)}{\partial x} + u_{av} \frac{\partial(\rho h V)}{\partial y} + \frac{\partial(\rho h)}{\partial t} \right] \quad (\text{A.2})$$

Table A.1: Non-dimensional parameters

Parameters	Dimensionless	Relation
x(m)	X	X=x/b
y(m)	Y	Y=y/a
$\rho(\text{kg/m}^3)$	$\bar{\rho}$	$\bar{\rho} = \rho / \rho_0$
$\eta(\text{N.s/m}^2)$	$\bar{\eta}$	$\bar{\eta} = \eta / \rho$
t(s)	$\bar{t}$	$\bar{t} = u_{av} t / R_x$
h(m)	H	H=hR <sub>x</sub> /b <sup>2</sup>
W(s)	W*	W/E* R <sub>x</sub> L
p(Pa)	P	P=p/p <sub>h</sub>
$u_a v(\text{m/s})$	U*	For 1-Dimensional U*= $u_{av} \eta_0 / E^* R_x$ For 2-Dimensional U*= $u / u_{av}$
$v_a v(\text{m/s})$	V*	V*= $v / v_{av}$
$\beta(\text{N/m}^2)$	$\bar{\beta}$	$\bar{\beta} = \beta R_x / \eta_0 u_{av}$

$$\frac{\partial}{\partial X} \left( \frac{\bar{\rho} H^3}{\bar{\eta}} \frac{\partial P}{\partial X} \right)_{i,j} + k^2 \frac{\partial}{\partial Y} \left( \frac{\bar{\rho} H^3}{\bar{\eta}} \frac{\partial P}{\partial Y} \right)_{i,j} = \psi \left( \left[ \frac{\partial(\bar{\rho} H U)}{\partial X} \right]_{i,j} + \frac{\partial(\bar{\rho} H V)}{\partial Y} \right)_{i,j} + \frac{R_x \bar{\rho}}{b} S^* \quad (\text{A.3})$$

$$\underbrace{\frac{\partial}{\partial X} \left( \frac{\bar{\rho}H^3}{\bar{\eta}} \frac{\partial P}{\partial X} \right)}_A + i k^2 \underbrace{\frac{\partial}{\partial Y} \left( \frac{\bar{\rho}H^3}{\bar{\eta}} \frac{\partial P}{\partial Y} \right)}_B = \psi \left( \left[ \underbrace{\frac{\partial(\bar{\rho}HU)}{\partial X}}_C + \underbrace{\frac{\partial(\bar{\rho}HV)}{\partial Y}}_D + \frac{R_x \bar{\rho}}{b} S^* \right] \right)$$

where :

$$\psi = 12 \frac{u_{av} \eta_0 R_x^2}{P_h b^3}, S^* = \frac{\partial h / \partial t}{u_{av}}, k = \frac{b}{a} \quad (\text{A.4})$$

Equation A.3 is expanded base on left hand side and right hand side of the equation. Term A and B, represent the Poiseuille flow in X and Y direction. Term C and D correspond to Couette flow also in X and Y direction.

$$\begin{aligned} \frac{\partial}{\partial X} \left( \frac{\bar{\rho}H^3}{\bar{\eta}} \frac{\partial P}{\partial X} \right)_{i,j} &= \frac{1}{\Delta X} \left[ \left( \frac{\bar{\rho}H^3}{\bar{\eta}} \frac{\partial P}{\partial X} \right)_{i+\frac{1}{2}} - \left( \frac{\bar{\rho}H^3}{\bar{\eta}} \frac{\partial P}{\partial X} \right)_{i-\frac{1}{2}} \right] \\ &= \frac{1}{2\Delta X^2} \left[ \left( \frac{\bar{\rho}H^3}{\bar{\eta}} \right)_{i+1,j} + \left( \frac{\bar{\rho}H^3}{\bar{\eta}} \right)_{i,j} \right] (P_{i+1,j} - P_{i,j}) \\ &\quad - \frac{1}{2\Delta X^2} \left[ \left( \frac{\bar{\rho}H^3}{\bar{\eta}} \right)_{i,j} - \left( \frac{\bar{\rho}H^3}{\bar{\eta}} \right)_{i-1,j} \right] (P_{i,j} - P_{i-1,j}) \\ A &= \frac{1}{2\Delta X^2} \left[ \left( \frac{\bar{\rho}H^3}{\bar{\eta}} \right)_{i,j} - \left( \frac{\bar{\rho}H^3}{\bar{\eta}} \right)_{i-1,j} \right] P_{i-1,j} \\ &\quad - \frac{1}{2\Delta X^2} \left[ \left( \frac{\bar{\rho}H^3}{\bar{\eta}} \right)_{i,j} + 2 \left( \frac{\bar{\rho}H^3}{\bar{\eta}} \right)_{i,j} + \left( \frac{\bar{\rho}H^3}{\bar{\eta}} \right)_{i,j} \right] P_{i,j} \\ &\quad + \frac{1}{2\Delta X^2} \left[ \left( \frac{\bar{\rho}H^3}{\bar{\eta}} \right)_{i+1,j} - \left( \frac{\bar{\rho}H^3}{\bar{\eta}} \right)_{i,j} \right] P_{i+1,j} \end{aligned} \quad (\text{A.5})$$

$$\begin{aligned}
\frac{\partial}{\partial Y} \left( \frac{\bar{\rho} H^3}{\bar{\eta}} \frac{\partial P}{\partial Y} \right)_{i,j} &= \frac{1}{\Delta Y} \left[ \left( \frac{\bar{\rho} H^3}{\bar{\eta}} \frac{\partial P}{\partial Y} \right)_{i,j+\frac{1}{2}} - \left( \frac{\bar{\rho} H^3}{\bar{\eta}} \frac{\partial P}{\partial Y} \right)_{i,j-\frac{1}{2}} \right] \\
&= \frac{1}{2\Delta Y^2} \left[ \left( \frac{\bar{\rho} H^3}{\bar{\eta}} \right)_{i,j+1} + \left( \frac{\bar{\rho} H^3}{\bar{\eta}} \right)_{i,j} \right] (P_{i,j+1} - P_{i,j}) \\
&\quad - \frac{1}{2\Delta Y^2} \left[ \left( \frac{\bar{\rho} H^3}{\bar{\eta}} \right)_{i,j} - \left( \frac{\bar{\rho} H^3}{\bar{\eta}} \right)_{i,j-1} \right] (P_{i,j} - P_{i,j-1}) \\
B &= \frac{1}{2\Delta Y^2} \left[ \left( \frac{\bar{\rho} H^3}{\bar{\eta}} \right)_{i,j} - \left( \frac{\bar{\rho} H^3}{\bar{\eta}} \right)_{i,j-1} \right] P_{i,j-1} \\
&\quad - \frac{1}{2\Delta Y^2} \left[ \left( \frac{\bar{\rho} H^3}{\bar{\eta}} \right)_{i,j+1} + 2 \left( \frac{\bar{\rho} H^3}{\bar{\eta}} \right)_{i,j} + \left( \frac{\bar{\rho} H^3}{\bar{\eta}} \right)_{i,j-1} \right] P_{i,j} \\
&\quad + \frac{1}{2\Delta X^2} \left[ \left( \frac{\bar{\rho} H^3}{\bar{\eta}} \right)_{i,j+1} + \left( \frac{\bar{\rho} H^3}{\bar{\eta}} \right)_{i,j} \right] P_{i,j+1} \tag{A.6}
\end{aligned}$$

$$C = \left( \frac{\partial(\bar{\rho}HU)}{\partial X} \right)_{i,j} = (1 - \beta_x) \frac{(\bar{\rho}HU)_{i+1,j} - (\bar{\rho}HU)_{i,j}}{\Delta X} + \beta_x \frac{(\bar{\rho}HU)_{i,j} - (\bar{\rho}HU)_{i-1,j}}{\Delta X}$$

$$D = \left( \frac{\partial(\bar{\rho}HV)}{\partial Y} \right)_{i,j} = (1 - \beta_y) \frac{(\bar{\rho}HV)_{i,j+1} - (\bar{\rho}HV)_{i,j}}{\Delta Y} + \beta_y \frac{(\bar{\rho}HV)_{i,j} - (\bar{\rho}HV)_{i,j-1}}{\Delta Y}$$

$$A_{i,j} + k^2 B_{i,j} = \psi \left[ C_{i,j} + k D_{i,j} + \frac{R_x}{b} \bar{\rho} S^* \right]$$

Therefore, the simplified version of non-dimensional can be expressed as;

$$F_{i,j} = A_{i,j} + k^2 B_{i,j} - \psi \left[ C_{i,j} + k D_{i,j} + \frac{R_x}{b} \bar{\rho} S^* \right] \tag{A.7}$$

By substitution of the previous A, B, C and D into equation A.3, the new finite difference for 2D Reynolds can be re-write as below;

$$\begin{aligned}
F_{i,j} = & \frac{1}{2\Delta X^2} \left\{ \left[ \left( \frac{\bar{\rho}H^3}{\bar{\eta}} \right)_{i,j} - \left( \frac{\bar{\rho}H^3}{\bar{\eta}} \right)_{i-1,j} \right] P_{i-1,j} \right. \\
& - \left[ \left( \frac{\bar{\rho}H^3}{\bar{\eta}} \right)_{i,j} + 2 \left( \frac{\bar{\rho}H^3}{\bar{\eta}} \right)_{i,j} + \left( \frac{\bar{\rho}H^3}{\bar{\eta}} \right)_{i,j} \right] P_{i,j} \\
& \left. + \left[ \left( \frac{\bar{\rho}H^3}{\bar{\eta}} \right)_{i+1,j} + \left( \frac{\bar{\rho}H^3}{\bar{\eta}} \right)_{i,j} \right] P_{i+1,j} \right\} \\
& + \frac{k^2}{2\Delta Y^2} \left\{ \left[ \left( \frac{\bar{\rho}H^3}{\bar{\eta}} \right)_{i,j} - \left( \frac{\bar{\rho}H^3}{\bar{\eta}} \right)_{i,j-1} \right] P_{i,j-1} + \left[ \left( \frac{\bar{\rho}H^3}{\bar{\eta}} \right)_{i,j} - \left( \frac{\bar{\rho}H^3}{\bar{\eta}} \right)_{i,j+1} \right] P_{i,j+1} \right. \\
& \left. - \left[ \left( \frac{\bar{\rho}H^3}{\bar{\eta}} \right)_{i,j+1} + 2 \left( \frac{\bar{\rho}H^3}{\bar{\eta}} \right)_{i,j} + \left( \frac{\bar{\rho}H^3}{\bar{\eta}} \right)_{i,j-1} \right] P_{i,j} \right\} \\
& - (1 - \beta_x) \frac{(\bar{\rho}HU)_{i+1,j} - (\bar{\rho}HU)_{i,j}}{\Delta X} + \beta_x \frac{(\bar{\rho}HU)_{i,j} - (\bar{\rho}HU)_{i-1,j}}{\Delta X} \\
& - (1 - \beta_y) \frac{(\bar{\rho}HV^*)_{i+1,j} - (\bar{\rho}HV^*)_{i,j}}{\Delta Y} + \beta_y \frac{(\bar{\rho}HV^*)_{i,j} - (\bar{\rho}HV^*)_{i-1,j}}{\Delta Y} \\
& - \psi \frac{R_x}{b} (\bar{\rho}S^*)_{i,j}
\end{aligned} \tag{A.8}$$

Assume that  $P_{i,j}$  are a set of approximate solutions to the real solution  $\bar{P}_i$ , the equation can be expressed as :

$$\begin{cases} \bar{F}_{i,j} = f(\bar{P}_{i-1,j}, \bar{P}_{i+1,j}, \bar{P}_{i,j}, \bar{P}_{i,j+1}, \bar{P}_{i,j-1}) = 0 \\ F_{i,j} = f(P_{i-1,j}, P_{i+1,j}, P_{i,j}, P_{i,j+1}, P_{i,j-1}) \neq 0 \end{cases}$$

By applying Taylor's series expansion can be expressed as well :

$$\begin{aligned}
\bar{F}_{i,j} = & F_{i,j} + \frac{\partial F_{i,j}}{\partial P_{i+1,j}} \Delta P_{i+1,j} + \frac{\partial F_{i,j}}{\partial P_{i-1,j}} \Delta P_{i-1,j} + \frac{\partial F_{i,j}}{\partial P_{i,j}} \Delta P_{i,j} \\
& + \frac{\partial F_{i,j}}{\partial P_{i,j+1}} \Delta P_{i,j+1} + \frac{\partial F_{i,j}}{\partial P_{i,j-1}} \Delta P_{i,j-1} + Err = 0
\end{aligned} \tag{A.9}$$

where  $\Delta P_{i,j} = \bar{P}_{i,j} - P_{i,j}$ .

Assuming that the truncating error is small enough to be neglected, equation A.9 can be re-written as:

$$\begin{aligned}
-F_{i,j} &= \bar{J}_{ij,i-1j}\Delta P_{i-1,j} + \bar{J}_{ij,i+1j}\Delta P_{i+1,j} + \bar{J}_{ij,ij-1}\Delta P_{i,j-1} \\
&\quad + \bar{J}_{ij,ij+1}\Delta P_{i,j+1} + \bar{J}_{ij,ij}\Delta P_{i,j} + Err
\end{aligned} \tag{A.10}$$

where  $\bar{J}_{i,k} = \frac{\partial F_i}{\partial P_k}$ .

To further expand the equation, the Gauss-Seidel iteration method is used where :

$$\Delta P_{k,l}^n = \frac{-F_{k,l} - J_{kl,k-1l}\Delta P_{k-1l}^n - J_{kl,k+1l}\Delta P_{k+1l}^{n-1} - J_{kl,kl-1}\Delta P_{kl-1}^n - J_{kl,kl+1}\Delta P_{kl+1}^{n-1}}{J_{kl,kl}} \tag{A.11}$$

The Jacobian matrix could be simplified in the equation as;

$$\Delta P_{k,l}^n = \frac{-J[5] - J[1]\Delta P_{k-1l}^n - J[0]\Delta P_{k+1l}^{n-1} - J[3]\Delta P_{kl-1}^n - J[2]\Delta P_{kl+1}^{n-1}}{J[4]} \tag{A.12}$$

where the updating of the pressure is based on :

$$P_{i,j}^n = P_{i,j}^{n-1} + \Omega \Delta P_{i,j}^n \tag{A.13}$$

## A.2 Jacobian matrix

The same method to solve Jacobian matrix for 2D problem that has been mention earlier in appendix A can be expand as below;

$$\bar{J}_{ij,i+1j}$$

$$\begin{aligned}
\bar{J}_{ij,i+1j} &= \frac{\partial F_{i,j}}{\partial P_{i+1,j}} \\
&= \frac{\partial}{\partial P_{i+1,j}} \left\{ \left[ \frac{1}{2\Delta X^2} \left\{ \left[ \left( \frac{\bar{\rho}H^3}{\bar{\eta}} \right)_{i,j} - \left( \frac{\bar{\rho}H^3}{\bar{\eta}} \right)_{i-1,j} \right] P_{i-1,j} \right. \right. \right. \\
&\quad - \left[ \left( \frac{\bar{\rho}H^3}{\bar{\eta}} \right)_{i+1,j} + 2 \left( \frac{\bar{\rho}H^3}{\bar{\eta}} \right)_{i,j} + \left( \frac{\bar{\rho}H^3}{\bar{\eta}} \right)_{i,j} \right] P_{i,j} \\
&\quad \left. \left. \left. + \left[ \left( \frac{\bar{\rho}H^3}{\bar{\eta}} \right)_{i+1,j} + \left( \frac{\bar{\rho}H^3}{\bar{\eta}} \right)_{i,j} \right] P_{i+1,j} \right\} \right. \\
&\quad + \frac{k^2}{2\Delta Y^2} \left\{ \left[ \left( \frac{\bar{\rho}H^3}{\bar{\eta}} \right)_{i,j} - \left( \frac{\bar{\rho}H^3}{\bar{\eta}} \right)_{i,j-1} \right] P_{i,j-1} \right. \\
&\quad - \frac{1}{2\Delta Y^2} \left[ \left( \frac{\bar{\rho}H^3}{\bar{\eta}} \right)_{i,j+1} + 2 \left( \frac{\bar{\rho}H^3}{\bar{\eta}} \right)_{i,j} + \left( \frac{\bar{\rho}H^3}{\bar{\eta}} \right)_{i,j-1} \right] P_{i,j} \\
&\quad \left. \left. \left. + \left[ \left( \frac{\bar{\rho}H^3}{\bar{\eta}} \right)_{i+1,j} + \left( \frac{\bar{\rho}H^3}{\bar{\eta}} \right)_{i,j} \right] P_{i+1,j} \right\} \right. \\
&\quad - \psi \frac{1}{\Delta X} (1 - \beta_x) \left\{ (\bar{\rho}HU)_{i+1,j} - (\bar{\rho}HU)_{i,j} + \beta_x (\bar{\rho}HU)_{i,j} - (\bar{\rho}HU)_{i-1,j} \right\} \\
&\quad - k\psi \frac{1}{\Delta Y} \left\{ (1 - \beta_y) \left[ (\bar{\rho}HV^*)_{i+1,j} - (\bar{\rho}HV^*)_{i,j} \right] + \beta_y \left[ (\bar{\rho}HV^*)_{i,j} - (\bar{\rho}HV^*)_{i-1,j} \right] \right\} \\
&\quad \left. \left. \left. - \psi \frac{R_x}{b} (\bar{\rho}S^*)_{i,j} \right] \right\} \right.
\end{aligned} \tag{A.14}$$



$$\begin{aligned}
\bar{J}_{i,j} = & \left\{ \frac{1}{2\Delta X^2} [M_{i+1,j}^{i,j} + M_{i+1,j}^{i-1,j}] P_{i-1,j} - [M_{i+1,j}^{i+1,j} + 2M_{i+1,j}^{i,j} + M_{i+1,j}^{i-1,j}] P_{i,j} \right. \\
& + [M_{i+1,j}^{i+1,j} + M_{i+1,j}^{i,j}] P_{i+1,j} + \left. \left[ \left( \frac{\bar{\rho} H^3}{\bar{\eta}} \right)_{i+1,j} + \left( \frac{\bar{\rho} H^3}{\bar{\eta}} \right)_{i,j} \right] \right\} \\
& + \frac{k^2}{2\Delta Y^2} \left\{ [M_{i+1,j}^{i,j} + M_{i+1,j}^{i,j-1}] P_{i,j-1} - [M_{i+1,j}^{i,j+1} + 2M_{i+1,j}^{i,j} + M_{i+1,j}^{i,j-1}] P_{i,j} \right. \\
& + [M_{i+1,j}^{i,j+1} + M_{i+1,j}^{i,j}] P_{i,j+1} \left. \right\} \\
& - \psi \frac{1}{\Delta X} \left\{ (1 - \beta_x) [{}_x N_{i+1,j}^{i+1,j} - {}_x N_{i+1,j}^{i,j}] + \beta_x [{}_x N_{i+1,j}^{i,j} - {}_x N_{i+1,j}^{i-1,j}] \right\} \\
& - k\psi \frac{1}{\Delta Y} \left\{ (1 - \beta_y) [{}_y N_{i,j+1}^{i,j+1} - {}_y N_{i,j+1}^{i,j}] + \beta_y [{}_y N_{i,j+1}^{i,j} - {}_y N_{i,j+1}^{i,j-1}] \right\} - 0
\end{aligned} \tag{A.15}$$

Where;

$$M_{k,l}^{i,j} = \frac{\partial \left( \frac{\bar{\rho} H^3}{\bar{\eta}} \right)_{i,j}}{\partial P_{k,l}} \quad , {}_x N_{k,l}^{i,j} = \frac{\partial (\bar{\rho} H)_{i,j}}{\partial P_{k,l}} \tag{A.16}$$

$\bar{J}_{ij,i-1j}$

$$\begin{aligned}
\bar{J}_{ij,i-1j} &= \frac{\partial F_{i,j}}{\partial P_{i-1,j}} \\
&= \left\{ \frac{1}{2\Delta X^2} [M_{i+1,j}^{i,j} + M_{i+1,j}^{i-1,j}] P_{i-1,j} - [M_{i+1,j}^{i+1,j} + 2M_{i+1,j}^{i,j} + M_{i-1,j}^{i-1,j}] P_{i,j} \right. \\
&\quad \left. + [M_{i-1,j}^{i+1,j} + M_{i-1,j}^{i,j}] P_{i+1,j} + \left[ \left( \frac{\bar{\rho} H^3}{\bar{\eta}} \right)_{i,j} + \left( \frac{\bar{\rho} H^3}{\bar{\eta}} \right)_{i-1,j} \right] \right\} \\
&\quad + \frac{k^2}{2\Delta Y^2} \left\{ [M_{i-1,j}^{i,j} + M_{i-1,j}^{i,j-1}] P_{i,j-1} - [M_{i-1,j}^{i,j+1} + 2M_{i-1,j}^{i,j} + M_{i-1,j}^{i,j-1}] P_{i,j} \right. \\
&\quad \left. + [M_{i-1,j}^{i,j+1} + M_{i-1,j}^{i,j}] P_{i,j+1} \right\} \\
&\quad - \psi \frac{1}{\Delta X} \left\{ (1 - \beta_x) [x N_{i-1,j}^{i+1,j} - x N_{i-1,j}^{i,j}] + \beta_x [x N_{i-1,j}^{i,j} - x N_{i-1,j}^{i-1,j}] \right\} - 0
\end{aligned} \tag{A.17}$$

$\bar{J}_{ij,ij+1}$

$$\begin{aligned}
\bar{J}_{ij,ij+1} &= \frac{\partial F_{i,j}}{\partial P_{i,j+1}} \\
&= \left\{ \frac{1}{2\Delta X^2} [M_{i,j+1}^{i,j} + M_{i,j+1}^{i-1,j}] P_{i-1,j} - [M_{i,j+1}^{i+1,j} + 2M_{i,j+1}^{i,j} + M_{i,j+1}^{i-1,j}] P_{i,j} \right. \\
&\quad \left. + [M_{i,j+1}^{i+1,j} + M_{i,j+1}^{i,j}] P_{i+1,j} \right\} \\
&\quad + \frac{k^2}{2\Delta Y^2} \left\{ [M_{i,j+1}^{i,j} + M_{i,j+1}^{i,j-1}] P_{i,j-1} - [M_{i,j+1}^{i,j+1} + 2M_{i,j+1}^{i,j} + M_{i,j+1}^{i,j-1}] P_{i,j} \right. \\
&\quad \left. + [M_{i,j+1}^{i,j+1} + M_{i,j+1}^{i,j}] P_{i,j+1} + \left[ \left( \frac{\bar{\rho} H^3}{\bar{\eta}} \right)_{i,j+1} + \left( \frac{\bar{\rho} H^3}{\bar{\eta}} \right)_{i,j} \right] \right\} \\
&\quad - \psi \frac{1}{\Delta X} \left\{ (1 - \beta_x) [x N_{i,j+1}^{i+1,j} - x N_{i,j+1}^{i,j}] + \beta_x [x N_{i,j+1}^{i,j} - x N_{i,j+1}^{i-1,j}] \right\} - 0
\end{aligned} \tag{A.18}$$

$\bar{J}_{ij,ij-1}$

$$\begin{aligned}
\bar{J}_{ij,ij-1} &= \frac{\partial F_{i,j}}{\partial P_{i,j-1}} \\
&= \left\{ \frac{1}{2\Delta X^2} [M_{i,j-1}^{i,j} + M_{i,j-1}^{i-1,j}] P_{i-1,j} - [M_{i,j-1}^{i+1,j} + 2M_{i,j-1}^{i,j} + M_{i,j-1}^{i-1,j}] P_{i,j} \right. \\
&\quad \left. + [M_{i,j-1}^{i+1,j} + M_{i,j-1}^{i,j}] P_{i+1,j} \right\} \\
&\quad + \frac{k^2}{2\Delta Y^2} \left\{ [M_{i,j-1}^{i,j} + M_{i,j-1}^{i,j-1}] P_{i,j-1} - [M_{i,j-1}^{i,j+1} + 2M_{i,j-1}^{i,j} + M_{i,j-1}^{i,j-1}] P_{i,j} \right. \\
&\quad \left. + [M_{i,j-1}^{i,j+1} + M_{i,j-1}^{i,j}] P_{i,j+1} + \left[ \left( \frac{\bar{\rho} H^3}{\bar{\eta}} \right)_{i,j-1} + \left( \frac{\bar{\rho} H^3}{\bar{\eta}} \right)_{i,j} \right] \right\} \\
&\quad - \psi \frac{1}{\Delta X} \left\{ (1 - \beta_x) [x N_{i,j-1}^{i+1,j} - x N_{i,j-1}^{i,j}] + \beta_x [x N_{i,j-1}^{i,j} - x N_{i,j-1}^{i-1,j}] \right\} - 0
\end{aligned} \tag{A.19}$$

$\bar{J}_{ij,ij}$

$$\begin{aligned}
\bar{J}_{ij,ij} &= \frac{\partial F_{i,j}}{\partial P_{i,j}} \\
&= \left\{ \frac{1}{2\Delta X^2} [M_{i-,j}^{i,j} + M_{i+1,j}^{i-1,j}] P_{i-1,j} - [M_{i+1,j}^{i+1,j} + 2M_{i,j}^{i,j} + M_{i,j}^{i-1,j}] P_{i,j} \right. \\
&\quad \left. + [M_{i,j}^{i+1,j} + M_{i,j}^{i,j}] P_{i+1,j} + \left[ \left( \frac{\bar{\rho}H^3}{\bar{\eta}} \right)_{i+1,j} + \left( \frac{\bar{\rho}H^3}{\bar{\eta}} \right)_{i,j} + \left( \frac{\bar{\rho}H^3}{\bar{\eta}} \right)_{i-1,j} \right] \right\} \\
&\quad + \frac{k^2}{2\Delta Y^2} \left\{ [M_{i,j}^{i,j} + M_{i,j}^{i,j-1}] P_{i,j-1} - [M_{i-1,j}^{i,j+1} + 2M_{i,j}^{i,j} + M_{i,j}^{i,j}] P_{i,j} \right. \\
&\quad \left. + [M_{i,j}^{i,j+1} + M_{i,j}^{i,j}] P_{i,j+1} - \left[ \left( \frac{\bar{\rho}H^3}{\bar{\eta}} \right)_{i,j+1} + \left( \frac{\bar{\rho}H^3}{\bar{\eta}} \right)_{i,j} + \left( \frac{\bar{\rho}H^3}{\bar{\eta}} \right)_{i,j-1} \right] \right\} \\
&\quad - \psi \frac{1}{\Delta X} \left\{ (1 - \beta_x) [x N_{i,j}^{i+1,j} - x N_{i,j}^{i,j}] + \beta_x [x N_{i-1,j}^{i,j} - x N_{i-1,j}^{i,j}] \right\} - 0
\end{aligned} \tag{A.20}$$

with M and N are defined as below;

$$\begin{aligned}
M_{k,l}^{i,j} &= \frac{\partial \left( \frac{\bar{\rho}H^3}{\bar{\eta}} \right)_{i,j}}{\partial P_{k,l}} \\
&= \left( \frac{H^3}{\bar{\eta}} \right)_{i,j} \frac{\partial \bar{\rho}_{i,j}}{\partial P_{k,l}} + \left( \bar{\rho}H^3 \right)_{i,j} \frac{\bar{\eta}_{i,j}^{-1}}{\partial P_{k,l}} + \left( \frac{\bar{\rho}}{\bar{\eta}} \right)_{i,j} \frac{\partial H_{i,j}^3}{\partial P_{k,l}} \\
&= \left( \frac{H^3}{\bar{\eta}} \right)_{i,j} \frac{\partial \bar{\rho}_{i,j}}{\partial P_{k,l}} - \left( \frac{\bar{\rho}H^3}{\bar{\eta}^2} \right)_{i,j} \frac{\partial \bar{\eta}_{i,j}}{\partial P_{k,l}} + 3 \left( \frac{\bar{\rho}H^2}{\bar{\eta}} \right)_{i,j} \frac{\partial H_{i,j}}{\partial P_{k,l}} \\
M_{k,l}^{i,j} &= \left( \frac{H^3}{\bar{\eta}} \right)_{i,j} Ro_{k,l}^{i,j} - \left( \frac{\bar{\rho}H^3}{\bar{\eta}^2} \right)_{i,j} Et_{k,l}^{i,j} + 3 \left( \frac{\bar{\rho}H^2}{\bar{\eta}} \right)_{i,j} D_{m,n}
\end{aligned} \tag{A.21}$$

$$Ro_{k,l}^{i,j} = \frac{\partial \bar{\rho}_{i,j}}{\partial P_{k,l}}; Et_{k,l}^{i,j} = \frac{\partial \bar{\eta}_{i,j}}{\partial P_{k,l}}; D_{m,n} = \frac{\partial H^2}{\partial P_{k,l}} \tag{A.22}$$

$${}_x N_{k,l}^{i,j} = \frac{\partial (\bar{\rho}HU)_{i,j}}{\partial P_{k,l}} = (HU)_{i,j} \frac{\partial \bar{\rho}_{i,j}}{\partial P_{k,l}} + (\bar{\rho}U)_{i,j} \frac{\partial \bar{\rho}_{i,j}}{\partial P_{k,l}} + (\bar{\rho}H)_{i,j} \frac{\partial U_{i,j}}{\partial P_{k,l}} \tag{A.23}$$

$${}_x N_{k,l}^{i,j} = (HU)_{i,j} Ro_{k,l}^{i,j} + (\bar{\rho})_{i,j} D_{m,n} \quad (\text{A.24})$$

Non-dimensional terms that used to define viscosity  $Et$  and density  $Ro$  are defined as stated below;

$$\begin{aligned} Ro_{k,l}^{i,j} &= \frac{\partial \bar{\rho}_{i,j}}{\partial P_{k,l}} = \frac{\partial}{\partial P_{k,l}} \left[ 1 + \frac{0.6 \cdot 10^{-9} \cdot P_h \cdot P_{i,j}}{1 + 1.7 \cdot 10^{-9} \cdot P_h \cdot P_{i,j}} \right] \\ &= 0.6 \cdot 10^{-9} P_h \frac{\partial}{\partial P_{k,l}} \left[ \frac{P_{i,j}}{1 + 1.7 \cdot 10^{-9} \cdot P_h \cdot P_{i,j}} \right] \\ &= 0.6 \cdot 10^{-9} P_h \left[ \frac{\frac{\partial P_{i,j}}{\partial P_l} (1 + 1.7 \cdot 10^{-9} \cdot P_h \cdot P_{i,j}) - P_{i,j} \frac{\partial (1 + 1.7 \cdot 10^{-9} \cdot P_h \cdot P_{i,j})}{\partial P_l}}{(1 + 1.7 \cdot 10^{-9} \cdot P_h \cdot P_{i,j})^2} \right] \\ &= \frac{0.6 \cdot 10^{-9} \cdot P_h}{(1 + 1.7 \cdot 10^{-9} \cdot P_h \cdot P_{i,j})^2} \frac{\partial P_{i,j}}{\partial P_{k,l}} \end{aligned} \quad (\text{A.25})$$

If  $k \neq l$  and/or  $l \neq j$

$$\frac{\partial \bar{P}_{i,j}}{\partial P_{k,l}} = 0 \quad \text{---} \quad > \quad \frac{\partial \bar{\rho}_{i,j}}{\partial P_{k,l}} = 0$$

If  $k = i$  and  $l = j$

$$\frac{\partial \bar{\rho}_{i,j}}{\partial P_{k,l}} = \frac{0.6 \cdot 10^{-9} \cdot P_h}{(1 + 1.7 \cdot 10^{-9} \cdot P_h \cdot P_{i,j})^2}$$

$$\begin{aligned}
Et_{k,l}^{i,j} &= \frac{\partial \bar{\eta}_{i,j}}{\partial P_{k,l}} = \frac{\partial \left[ e^{[\ln \eta_0 + 9.67] \left[ -1 + \left( 1 + \frac{P_h \cdot P_{i,j}}{P_0} \right)^z \right]} \right]}{\partial P_{k,l}} \\
&= \frac{\partial \left[ \ln \eta_0 + 9.67 \right] \left[ -1 + \left( 1 + \frac{P_h \cdot P_{i,j}}{P_0} \right)^z \right]}{\partial P_{k,l}} \bar{\eta}_{i,j} \\
&= [\ln \eta_0 + 9.67] \bar{\eta}_{i,j} \frac{\partial \left[ \left( 1 + \frac{P_h \cdot P_{i,j}}{P_0} \right)^z \right]}{\partial P_{k,l}} \\
&= [\ln \eta_0 + 9.67] \bar{\eta}_{i,j} z \left( 1 + \frac{P_h \cdot P_{i,j}}{P_0} \right)^{z-1} \frac{\partial \left[ \left( 1 + \frac{P_h \cdot P_{i,j}}{P_0} \right)^z \right]}{\partial P_{k,l}} \\
&= [\ln \eta_0 + 9.67] \frac{\bar{\eta}_{i,j} z P_h}{P_0} \left( 1 + \frac{P_h \cdot P_{i,j}}{P_0} \right)^{z-1} \frac{\partial P_{i,j}}{\partial P_{k,l}} \\
\frac{\partial \bar{\eta}_{i,j}}{\partial P_{k,l}} &= [\ln \eta_0 + 9.67] \frac{\bar{\eta}_{i,j} z P_h}{P_0} \left( 1 + \frac{P_h \cdot P_{i,j}}{P_0} \right)^{z-1} \frac{\partial P_{i,j}}{\partial P_{k,l}}
\end{aligned} \tag{A.26}$$

If  $k \neq l$  and/or  $l \neq j$

$$\frac{\partial \bar{P}_{i,j}}{\partial P_{k,l}} = 0 \quad \text{---} \quad > \quad \frac{\partial \bar{\eta}_{i,j}}{\partial P_{k,l}} = 0$$

If  $k = i$  and  $l = j$

$$\frac{\partial \bar{P}_{i,j}}{\partial P_{k,l}} = 1 \quad \text{---} \quad > \quad \frac{\partial \bar{\eta}_{i,j}}{\partial P_{k,l}} = \left( [\ln \eta_0 + 9.67] \frac{\bar{\eta}_{i,j} z P_h}{P_0} \left( 1 + \frac{P_h \cdot P_{i,j}}{P_0} \right)^{z-1} \right)$$

where

$$\left( P_0 = \frac{1}{5.1e^{-9}} \right)$$

### A.3 Mathematical derivation for surface deflection

In order to calculate the surface deflection along the lubricated point contact, the following formula is used;

$$\delta_{k,l} = \frac{2P_h}{\pi E'} \sum_{j=1}^{n_x} \sum_{i=1}^{n_y} P_{i,j} D_{m,n} \quad (\text{A.27})$$

where  $m$  and  $n$  incorporate within them the effect of a pressure node  $(i,j)$  on a deflection node  $(k,l)$  and are expressed as :

$$m = |k - i| (m = |k - i + 1|)$$

$$n = |l - j| (n = |l - j + 1|)$$

The deflection influence coefficient matrix , D is given as follow [];

$$D_{m,n} = (\bar{y} - \bar{a}) \ln \left[ \frac{(\bar{x} - \bar{b}) + \sqrt{(\bar{y} - \bar{a})^2 + (\bar{x} - \bar{b})^2}}{(\bar{x} + \bar{b}) + \sqrt{(\bar{y} - \bar{a})^2 + (\bar{x} + \bar{b})^2}} \right]$$

$$+ (\bar{y} + \bar{a}) \ln \left[ \frac{(\bar{x} + \bar{b}) + \sqrt{(\bar{y} + \bar{a})^2 + (\bar{x} + \bar{b})^2}}{(\bar{x} - \bar{b}) + \sqrt{(\bar{y} + \bar{a})^2 + (\bar{x} - \bar{b})^2}} \right]$$

$$+ (\bar{x} + \bar{b}) \ln \left[ \frac{(\bar{y} + \bar{a}) + \sqrt{(\bar{y} + \bar{a})^2 + (\bar{x} + \bar{b})^2}}{(\bar{y} - \bar{a}) + \sqrt{(\bar{y} - \bar{a})^2 + (\bar{x} + \bar{b})^2}} \right]$$

$$+ (\bar{x} - \bar{b}) \ln \left[ \frac{(\bar{y} - \bar{a}) + \sqrt{(\bar{y} - \bar{a})^2 + (\bar{x} - \bar{b})^2}}{(\bar{y} + \bar{a}) + \sqrt{(\bar{y} + \bar{a})^2 + (\bar{x} - \bar{b})^2}} \right] = [m] \quad (\text{A.28})$$

where:

$$\bar{b} = \frac{\Delta x}{2}, \bar{a} = \frac{\Delta y}{2} \text{ and } \bar{x} = x_{k,l} - x_{i,j} = m\Delta X = [m], \bar{y} = y_{k,l} - y_{i,j} = n\Delta y = [m] \quad (\text{A.29})$$




$$\begin{aligned}
D_{m,n} = & ymln \left[ \frac{xm + \sqrt{ym^2 + xm^2}}{xp + \sqrt{ym^2 + xp^2}} \right] + ypln \left[ \frac{xp + \sqrt{yp^2 + xp^2}}{xm + \sqrt{yp^2 + xm^2}} \right] \\
& + xpln \left[ \frac{yp + \sqrt{yp^2 + xp^2}}{xm + \sqrt{ym^2 + xp^2}} \right] + xmln \left[ \frac{ym + \sqrt{ym^2 + xm^2}}{yp + \sqrt{yp^2 + xm^2}} \right]
\end{aligned} \tag{A.30}$$

# Appendix B

## SAE grade lubricant

### SAE5W40



## Shell Helix *Ultra* 5W-40

*Maximises performance right up to the next oil change*

Shell Helix Ultra has been formulated with Shell's ultimate active cleansing technology. It works harder to protect than conventional motor oils by continuously helping to prevent dirt and sludge build-up, for better responsiveness and improved performance, thus helping your engine to operate at its full potential right up to the next oil change.

Technical Data Sheet

**DESIGNED TO MEET CHALLENGES**

#### Performance, Features & Benefits

- Shell's ultimate active cleansing technology**  
Up to five times more effective at removing sludge from dirty engines than a mineral oil.
- Long-term oxidation stability**  
Up to 30% more protection than other fully synthetic leading brands tested.
- Low viscosity, rapid oil flow and low friction**  
Greater fuel efficiency and easier cold starting.
- High shear stability**  
Maintains viscosity and stays in grade throughout the oil change interval.
- Specially selected synthetic base oils**  
Reduce oil volatility and therefore oil consumption and the need for top-up.
- Minimises vibration and engine noise**  
Smoother, quieter drive.

#### Main Applications

- Suitable for fuel-injected petrol engines fitted with 'blow-by' gas recirculation and catalytic converters operating in extreme driving conditions.

#### Specifications, Approvals & Recommendations

- API: SN/CF
- ACEA: A3/B3, A3/B4
- VW: 502.00/505.00
- MB Approval: 229.5
- BMW: LL-01
- Porsche: A40
- ferrari
- Fiat: 9.55535.Z2 (Meets the requirements of)
- Renault: RN 0700/0710
- PSA: B71 2296

For a full listing of equipment approvals and recommendations, please consult your local Shell Technical Helpdesk, or the OEM Approvals website.

#### Typical physical characteristics

Properties	Method	Shell Helix Ultra 5W-40
Viscosity Grade		5W-40
Kinematic Viscosity @40°C	cSt	ASTM D445 74.4
Kinematic Viscosity @100°C	cSt	ASTM D445 13.1
density @15°C	kg/l	ASTM 4052 0.840
Pour Point	°C	ASTM D97 -39
Hths Viscosity @150°C	m PaS	ASTM D4741 3.68
Flash Point (Pmcc)	°C	ASTM D93 215

These characteristics are typical of current production. Whilst future production will conform to Shell's specification, variations in these characteristics may occur.

# SAE10W40



Technical Data Sheet

## Shell Helix *HX7* 10W-40

*Cleans and Protects for Extra Responsiveness*

Shell Helix HX7 has been formulated with special active cleansing technology. It works harder to protect than conventional motor oils by continuously helping to prevent dirt and sludge build-up for better responsiveness right up to the next scheduled oil change.

### DESIGNED TO MEET CHALLENGES

#### Performance, Features & Benefits

- **Special Active Cleansing Technology**  
Up to twice as effective at removing sludge from dirty engines as a normal mineral oil.
- **Enhanced Oxidation Stability**  
Up to 19% more protection than other leading synthetic technology products tested.
- **Low Viscosity, Rapid oil flow and low friction**  
Greater fuel efficiency.
- **High Shear Stability**  
Maintains viscosity and stays in grade throughout the oil change interval.
- **Specially Selected Synthetic Base Oils**  
Reduce oil volatility and therefore oil consumption and the need for top-up.
- **Minimises vibration and engine noise**  
Smoother, quieter drive.

#### Main Applications

Suitable for fuel-injection gasoline engines fitted with 'blow-by' gas recirculation and catalytic converters. Also suitable for turbo-charged and intercooled, direct-injection diesel engines fitted with 'blow-by' gas recirculation without particulate filters.

#### Specifications, Approvals & Recommendations

- API: SN/CF
- ACEA: A3/B3, A3/B4
- Jaso: SG+
- MB Approval: 229.3
- VW: 502.00/505.00
- GM: LL-B-025
- Renault: RN 0700, RN 0710
- PSA: B71 2296
- Fiat: 9.55535-G2 (meets requirements)

For a full listing of equipment approvals and recommendations, please consult your local Shell technical helpdesk, or the OEM Approvals Website.

#### Typical physical characteristics

Properties			Method	Shell Helix HX7
Viscosity Grade				10W-40
Kinematic Viscosity	@40°C	cSt	ASTM D445	92.1
Kinematic Viscosity	@100°C	cSt	ASTM D445	14.4
Density	@15°C	kg/l	ASTM D4052	0.880
Flash Point (Pmcc)			°C	220
Pour Point			°C	-39

These characteristics are typical of current production. Whilst future production will conform to Shell's specification, variations in these characteristics may occur.

# SAE15W40



Technical Data Sheet

## Shell Helix *HX5* 15W-40

*Premium multi-grade motor oil - Helps to remove sludge from dirty engines*

Shell Helix HX5 is designed to help provide consistent engine performance. It works hard to help protect against engine sludge and reduce wear. It is suitable for a wide variety of vehicles for everyday driving conditions.

Proud Drivers Choose Shell Helix

### Performance, Features & Benefits

- **Active cleansing technology**  
Actively locks away harmful performance-robbing deposits.
- **Active clean-up**  
Helps to remove sludge left behind by inferior oils <sup>2</sup>
- **Effective wear protection** <sup>1</sup>  
Helps to protect against wear and neutralise corrosive combustion acids.
- **Resistance to oil degradation** <sup>2</sup>  
Helps to maintain protection throughout the oil-drain interval.
- **Multi-fuel capability**  
Can be used for gasoline, diesel and gas engines, and is also suitable for biodiesel and gasoline/ethanol blends.

<sup>1</sup> Based on Sequence IVA engine test carried out at an independent laboratory

<sup>2</sup> Based on a severe sludge clean-up test

### Main Applications

- Shell Helix HX5's premium multigrade formulation helps to provide protection in everyday daily driving conditions. Shell Helix HX5 can be used for gasoline, diesel and gas engines, and it is also suitable for biodiesel and gasoline/ethanol blends.

### Specifications, Approvals & Recommendations

- API SN/CF
- ACEA A3/B3
- To find the right Shell Helix product for your vehicles and equipment, please consult Shell LubeMatch at: <http://lubematch.shell.com>
- Advice on applications not covered here may be obtained from your Shell or Shell Lubricants distributor representatives or technical help desks.

### Typical Physical Characteristics

Properties			Method	Shell Helix HX5
SAE Viscosity Grade				15W-40
Kinematic Viscosity	@40°C	cSt	ASTM D445	106.00
Kinematic Viscosity	@100°C	cSt	ASTM D445	14.27
Viscosity Index			ASTM D2270	137
MRV	@-25°C	cP	ASTM D4684	17000
Density	@15°C	kg/m <sup>3</sup>	ASTM D4052	865.8
Flash Point			ASTM D92	241
Pour Point			ASTM D97	-45

These characteristics are typical of current production. Whilst future production will conform to Shell's specification, variations in these characteristics may occur.

# Appendix C

## List of Publications

### Published Journal Papers

1. **S.H. Hamdan** W.W.F. Chong, J.-H. Ng, C.T. Chong, H. Zhang Ng. Nano-tribological characterisation of palm based trimethylolpropane ester for application as boundary lubricant. *Tribology International*. Paper under review.
2. M.H. Din, **S.H. Hamdan**. W.W.F. Chong. Frictional Analysis on Engine Lubricant Dilution by Coconut oil and Soybean oil Derived Biodiesel. *Jurnal Tribologi*. Accepted.
3. Y.C. Ng, **S.H. Hamdan**. W.W.F. Chong. Development Of A Mathematical Tool To Predict Engine In-Cylinder Friction. *Jurnal Tribologi*. Accepted.
4. **S.H. Hamdan**, W.W.F. Chong, J.-H. Ng , C.T. Chong and S. Rajoo. A study of the tribological impact of biodiesel dilution on engine lubricant properties. *Process Safety and Environmental Protection*. doi.org/10.1016/j.psep.2017.05.007 **2017** .
5. **S.H. Hamdan**, W.W.F. Chong, J.-H. Ng, M.J. Ghazali, and R.J.K. Wood. Influence of Fatty Acid Methyl Ester Composition on Tribological Properties of Vegetable Oils and Duck Fat Derived Biodiesel. *Tribology International* dx.doi.org/10.1016/j.triboint.2016.12.008, **2016**.

### Refereed conference proceedings

1. **S.H. Hamdan**,W.W.F.Chong. Simulation of Lubrication Stribeck curve for SAE grade engine lubricants *Proceedings of the 6th Asia International Conference on Tribology (ASIATRIB-2018)*, Sarawak, Malaysia **September 16 - 21, 2018**.
2. **S.H. Hamdan**,W.W.F.Chong, Jo-Han Ng. Nano-tribological characterisation of palm oil-based trimethylolpropane (TMP) ester for application as boundary lubricant. *Challenges in Environmental Science & Engineering (CESE-2017)*, Kunming, China, **November 10 - 16, 2017**.
3. **S.H. Hamdan**,W.W.F.Chong. Assessment on biodiesel behavior in EHL and ML lubrication regime. *World Tribology Congress (WTC-2017)*,Beijing, China, **September 17 - 22, 2017**.

4. W.W.F.Chong. **S.H. Hamdan**, Assessment on biodiesel behavior in EHL and ML lubrication regime. *World Tribology Congress (WTC-2017,Beijing, China, September 17 - 22, 2017.*
5. **S.H. Hamdan**, W.W.F. Chong, J.-H. Ng, M.J. Ghazali, and R.J.K. Wood. Lubrication Stribeck curve characterisation of vegetable oil derived biodiesel . *Leeds-Lyon Symposium on Tribology, September 6 - 9 2016* , Leeds Trinity University,UK, Organised by Leeds-School of Mechanical Engineering.

## **Poster presentation**

1. **S.H. Hamdan**, W.W.F. Chong, and J.-H. Ng,Friction assessment of SAE grade 10W40 lubricant: A combined numerical and experimental study, *5th FEE PG Conference of Engineering Sciences, 2nd November 2016*, Grand Harbour Hotel, Southampton, UK.

## **Journal paper under preparation**

1. **S.H. Hamdan**, W.W.F. Chong, and S. Yusup. Nano-tribological characterisation between the interaction of methyl oleate and zinc dialkyldithiophospate (ZDDP).